Dissertation
submitted to the
Combined Faculty of Mathematics, Engineering and Natural Sciences
of Heidelberg University, Germany
for the degree of
Doctor of Natural Sciences

Put forward by
Theodoros Soultanis
born in: Thessaloniki, Greece
Oral examination: 06.12.2022

Spectral properties of gravitational waves from neutron star merger remnants

Referees: Priv. Doz. Dr. Andreas Bauswein
Apl. Prof. Dr. Christian Fendt

Zusammenfassung

Wir stellen ein neues analytisches Modell vor, das die Gravitationswellenemission in der Phase nach der Verschmelzung von Doppelneutronensternen beschreibt. Das Modell wird durch eine Reihe von physikalischen Parametern bestimmt, die mit verschiedenen Oszillationsmoden, Kombinationstönen oder nicht-linearen dynamischen Merkmalen zusammenhängen. Ausserdem wird die zeitliche Entwicklung der dominanten Mode nach der Verschmelzung mit einbezogen. Das Modell beschreibt die numerischen Daten von Simulationen mit unterschiedlicher Gesamtmasse mit sehr hoher Genauigkeit. Alle Parameter des Modells korrelieren mit der Gesamtmasse des Doppelsterns. Für hohe Massen des Systems identifizieren wir neue spektrale Merkmale, die von der nicht-linearen Kopplung zwischen der quasi-radialen Oszillation und einer Deformation des Verschmelzungsüberrests herrühren. Deren Einbeziehung erhöht die Genauigkeit des Modells signifikant. Wir stellen fest, dass die subdominanten Frequenzkomponenten entscheidend für die Konstruktion von zuverlässigen Gravitationswellenmodellen sind. Aufgrund der hohen Genauigkeit ist unser Modell besonders für die Suche mit verbesserten Versionen der aktuellen Detektoren (aLIGO+, aVirgo+) oder zukünftigen Instrumenten geeignet. Wir finden eine quasi-universelle Beziehung zur Beschreibung der Nähe eines Doppelsterns zum Einsetzen des Gravitationskollapses zum Schwarzen Loch. Anschließend entwickeln wir eine Methode zur Bestimmung der Grenzmasse für die direkte Bildung Schwarzer Löcher und der maximalen Masse von nicht rotierenden Neutronensternen. Dieses Verfahren stützt sich auf eine einzige präzise Messung der Gravitationswellen vor und nach der Verschmelzung.

Abstract

We present a new analytic model describing gravitational wave emission in the post-merger phase of binary neutron star mergers. The model is determined by a number of physical parameters that are related to various oscillation modes, combination tones or non-linear features. The time evolution of the main post-merger frequency is incorporated. The model achieves high fitting factors for a sequence of equal-mass simulations of varying mass. All parameters of the model correlate with the total binary mass. For high binary masses, we identify new spectral features originating from the non-linear coupling between the quasi-radial oscillation and an antipodal tidal deformation of the remnant, the inclusion of which enhances the corresponding fitting factors. We find that subdominant frequency components are crucial for the construction of faithful gravitational wave templates. Because of the high fitting factors our model is particularly suitable for searches with upgraded detectors of the current generation (aLIGO+, aVirgo+) or future detectors. We find a quasi-universal relation for the proximity of a binary configuration to black-hole formation. We then develop a method for determining the threshold mass for prompt black-hole formation and the maximum mass of non-rotating neutron stars. This procedure relies on one precise measurement of the inspiral and post-merger phase.

To my parents, Ioanna and Dimitris,
my siblings, Evangelia and Miltos,
and my partner,
Andriana

Contents

List of Figures

List of Tables

List of Abbreviations

ADM	Arnowitt–Deser–Misner
BH	black-hole
CFC	conformal flatness condition
EoS	equation of state
FF	fitting factor
GW	gravitational wave
ID	initial data
NS	neutron star
PCA	principal component analysis
QC	quasi-circular
SPH	smooth particle hydrodynamics
RK	Runge-Kutta
WENO	weighted essentially non-oscillatory

List of Physical Constants

c	speed of light
G	gravitational constant
$M_\odot$	solar mass

1. Introduction

1.1. Motivation

Neutron star (NS) mergers are rare astrophysical events and strong gravitational wave (GW) emitters. The first GW detection from a source identified as a NS merger, GW170817 [6], was reported in 2017. The GWs produced during the pre-merger and post-merger phase contain information about the interior of NSs at different high-density regimes, respectively. The total binary mass of the system can be extracted from the GW signal, and also rough estimates of the distance and localization of source can be obtained.

Neutron star mergers are also associated to electromagnetic (EM) transients such as short gamma-ray burst (sGRB) [7, 8] and kilonova (see [9, 10]). Both transients were detected along with GW170817 [11–20]. Short gamma-ray bursts are bursts of gamma-rays with a typical duration of less than ≈ 2 s [7, 8]. They exhibit a characteristic highly focused relativistic jet which is powered by the accretion of matter to the remnant.

The kilonova is a quasi-isotropic EM transient occurring in NS mergers, that originates from the radioactive decay of heavy, neutron-rich elements produced through the rapid neutron-capture process (r-process) [21] in the ejecta of these events. The r-process is a series of nuclear reactions where seed nuclei (like iron) rapidly capture neutrons in a neutron-rich environment with a timescale shorter than that of beta-decay. The production of half of the heavy elements in the universe is explained by the r-process nucleosynthesis occurring in neutron-rich environments such as those of NS mergers. These newly formed elements decay, heat the ejecta, and when those expand enough, thermal radiation produces an EM transient, the kilonova. The characteristics of the observed kilonova depend on the total mass, velocity, and composition of the ejected material (see [22]), and so, carry information about the properties of high-density matter and the r-process. The detection of GW170817 and its EM counterparts, along with a scrutinized analysis that followed, showed that NS mergers are likely the major r-process element production sites in the universe.

Neutron star mergers provide a rich extraterrestrial laboratory for probing physics at high densities. The underlying physics in the interior of NSs is described by the so-called equation of state (EoS) of NSs which is, so far, only incompletely known. Nevertheless, different theoretical models have been proposed. The properties of NSs, the GWs and the EM counterparts in NS mergers depend on the EoS, and so, theoretical models can be tested with observations. Multi-messenger observations, where information from GWs and EM counterparts is combined, can

provide observational constraints on the EoS and reduce the uncertainties in the extracted properties of the GW source.

There are two distinct phases of GW radiation in NS mergers, the *inspiral phase* and the *post-merger phase*. In the inspiral phase, the NSs are in a quasi-circular orbit, where their distribution of mass forms a quadrupole which results to emission of gravitational waves. As energy is extracted from the system via GW emission, the orbit shrinks, and the NSs eventually merge. In the late stage of the inspiral, at a separation distance between the NS centers of approximately 35-45 km, tidal effects become important and accelerate the merger. Tidal effects are connected to the EoS of NSs (see Sec. 1.2) via the tidal deformability Λ and thus the inspiral can provide significant information about the underlying EoS [23, 24].

In the post-merger phase, if the total binary mass ($M_{\rm tot}$) is lower than a threshold mass ($M_{\rm thres}$) for prompt collapse [5, 25, 26], the remnant is a meta-stable rapidly differentially rotating NS. Even if its mass exceeds the maximum mass of a non-rotating NS, it is supported against gravitational collapse due to rapid differential rotation and thermal pressure. The remnant is hot and highly deformed, non-axisymmetric, and oscillates in different fluid (quasi) oscillation modes which emit GWs in frequencies (around 2-4 kHz) that correlate with the EoS (see [27–31]). The post-merger phase provides many channels for gaining information about the NS EoS.

The dominant frequency component in the post-merger GW spectrum is associated to the quadrupolar oscillation mode ($f_{\rm peak}$) [27, 31–47]. Generally, $f_{\rm peak}$ reaches high values for soft EoSs and low values for stiff EoSs. For varying EoSs, the frequency $f_{\rm peak}$ correlates with the radii of non-rotating NSs. The authors in [48] performed a large number of binary simulations with fixed $M_{\rm tot}$ and found tight correlations between $f_{\rm peak}$ and the radius $R_{1.6}$ of a non-rotating NS with gravitational mass of 1.6 $M_\odot$. These relations were further explored for a slightly wider mass range in [38, 39] (and not a fixed $M_{\rm tot}$), with also slightly larger average scatter between the data and the fits. More recently, [49] introduced two-parametric empirical relations connecting chirp mass ($M_{\rm chirp}$), $f_{\rm peak}$, and different NS radii, for a wide range of total binary masses. Such relations are important because with those, a measurement of $f_{\rm peak}$ can be converted to a measurement of the NS radius. The radius is uniquely linked to the EoS through the stellar structure equations and does thus provide valuable information about the properties of high-density matter.

Further information on the incompletely known EoS is encoded in the threshold mass $M_{\rm thres}$ for black-hole (BH) formation. Generally, if $M_{\rm tot} \geq M_{\rm thres}$ then a BH is formed, while if $M_{\rm tot} < M_{\rm thres}$ a meta-stable remnant is formed. The threshold mass $M_{\rm thres}$ and its dependence on the EoS was first investigated in [25, 26] and later in [50]. In these works, the authors explored correlations between $M_{\rm thres}$, different NS radii, and the maximum mass $M_{\rm max}$ of a non-rotating NS. Following the detection of GW170817, the authors in [51] (and later [50]) used an empirical relation for $M_{\rm thres}$, $M_{\rm thres}(M_{\rm max}, R_{1.6})$ [26], to impose lower limit constraints on the NS radius using the fact that the remnant of GW170817 most likely did not result in a prompt collapse, as suggested by the properties of the EM emission [10, 22]. Additional studies on $M_{\rm thres}$ have been carried out recently e.g. [5, 52–54]. Finally,

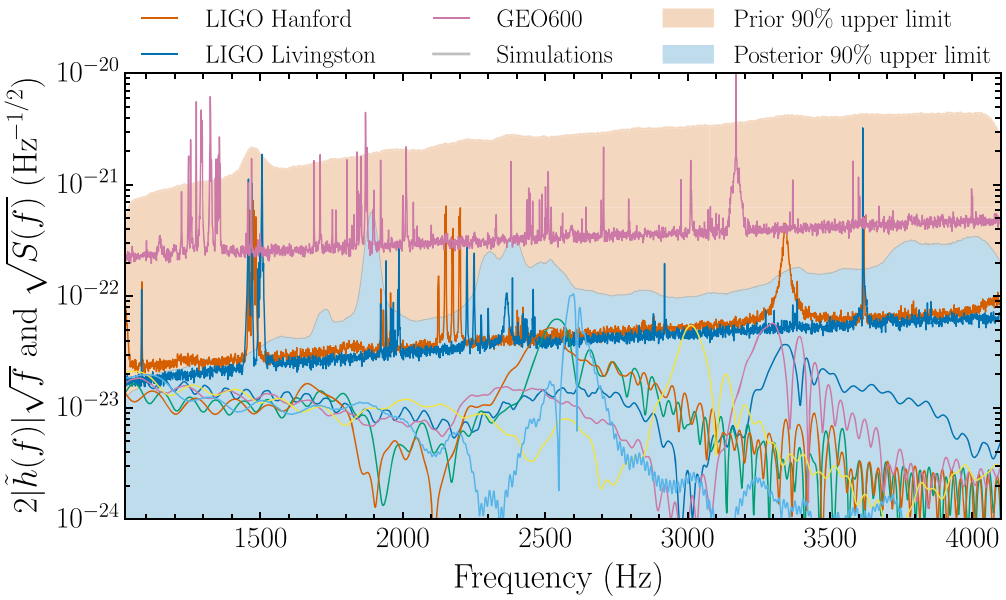

Figure 1.1: Noise spectral densities for different detectors and GW spectra from numerical relativity simulations for the analysis of GW170817 carried out in [1]. Figure adapted from [1]. Title: *Properties of the Binary Neutron Star Merger GW170817*.

we note that the post-merger GW emission can be employed to determine the end product of a NS merger event.

As is apparent, the detection of GWs from the post-merger phase would provide plenty of new research opportunities and physics to explore. Unfortunately, the early versions of the second-generation detectors, aLIGO and aVirgo, were unable to detect the post-merger phase of GW170817 (see Fig. 1.1). Since then, different upgrades to these detectors have been introduced and their sensitivity is significantly improved (see [55]). We note that their target sensitivity is not yet reached, and so, more improvements will follow in the future. An additional detector, KAGRA, started operating in 2020 (see [55]). Furthermore, plans for third-generation detectors, such as Einstein Telescope [56] and Cosmic Explorer [57], or dedicated high-frequency detectors [58–62] are currently being developed. Under these circumstances, for a source with properties similar to GW170817 and comparable luminosity distance, a measurement of the post-merger phase will be feasible in the near future. This highlights the necessity to better understand the post-merger GW emission and develop strategies for their detection.

In addition to detectors with sufficient sensitivity, GW detections also rely on robust and efficient data analysis techniques for the identification of a source and the parameter estimation for its properties. One approach is to employ matched-filtering methods which require post-merger GW template banks. In those methods, a model describing the GW emission, namely a GW template, is correlated with the unknown signal obtained from the detector in order identify the presence of the model in the unknown signal. This process is computationally expensive and requires fast and accurate waveform models for the GW emission in NS mergers that cover a wide range of the parameter space.

In this thesis we model NS mergers, and extract the emitted GWs, using 3-dimensional simulations in numerical relativity. In those, Einstein's equations are solved numerically using complex parallelized codes that require substantial computational resources. Although numerical simulations of binary NS mergers provide a tool for studying the GWs in the post-merger phase, the total time required for a simulation along with the large computational cost, renders these simulations inapplicable for matched-filtering searches. Nevertheless, GWs from the post-merger phase computed within numerical relativity aid the development of GW templates. In recent years, several GW template time-domain or frequency-domain models have been introduced e.g. [38, 41, 42, 63–72] (see also Sec. 1.4).

To construct faithful GW template models for the description of the post-merger emission an in-depth understanding of the spectral features of the GW spectrum is essential. The dependencies of the various frequency components in the GW signal on the characteristic properties of the system, such as the total binary mass and the mass ratio, have to be explored. In addition, the impact of the EoS on the GW spectrum has to also be assessed. To this end, it is imperative to understand the physical mechanisms, couplings and combination tones between frequency components, that generate those spectral features. To develop general purpose GW templates for a large parameter space of total mass, mass ratio, and EoS models, empirical relations for the properties of the GW spectrum, such as the frequencies of the different components, are required. For this reason, a precise explanation for the origin of the various spectral features is necessary for the development of physically inspired and accurate correlations between specific quantities, and combinations of those, associated to NSs with reduced scattering errors. Finally, we note that the inferred quantities and therefore the EoS constraints, from the GW detection using such templates also rely on empirical relations (as also described before). For these reasons, a study like the one carried out in this thesis, where the spectral properties of the GW emission in the post-merger phase for a large set of varying EoS, masses, and ratios, and also simulation tools is important.

1.2. Neutron stars

Before we describe a detailed background for the different projects and goals of this thesis, we give a brief overview about NSs. We discuss their formation, typical values for mass, radius, central density, and their internal structure described by the EoS.

Formation process

A NS is formed when the core of a massive star with an initial mass roughly larger than 8 $M_\odot$ undergoes gravitational collapse and supernova explosion ([73–75] for more details). If the initial mass is smaller than a critical value, a hot proto-neutron star (with a temperature of several 10 MeV) is formed following the supernova explosion. The hot proto-neutron star cools down due to neutrino

emission in ≈ 10 s resulting in a cold[1] NS, which is supported against gravity by the repulsive forces of nuclear matter.

Typical values

Neutron stars have gravitational masses ranging from roughly 1.1 $M_\odot$ to $2.0 - 3.0$ $M_\odot$, while their radius is expected to be around $10 - 14$ km (see [23, 74]). The lower limit in the NS mass is imposed by the formation mechanism (see [76, 77] and references therein), while the maximum mass has to be at least equal to the largest observed pulsar mass [78]. An upper limit on the maximum mass can be estimated based on causality, that is, the speed of sound cannot be larger than the speed of light [79]. The maximum rest-mass density at the core of the NS is believed to be roughly around $\approx 1.0\text{-}2.5 \cdot 10^{15}$ g/cm^3. We remark that the exact values of the maximum mass, the radius, and the maximum rest-mass density depend on the so far incompletely known equation of state (see below).

Internal structure

The internal structure of a NS consists of five regions, namely the inner core, the outer core, the crust, the envelope and the atmosphere [74, 76]. The envelope and the atmosphere carry only a negligible fraction of the total mass. The crust consists of neutron-rich nuclei, and at densities larger than the neutron drip density of $4 \cdot 10^{11}$ g/cm^3 neutrons become unbound from the nuclei (the neutron chemical potential becomes zero). At even higher densities, roughly from a fourth (1/4) to a half (1/2) of the nuclear saturation density $\rho_s = 2.7 \cdot 10^{14} \cdot$ g/cm^3 the strongly deformed nuclei form the so-called nuclear pasta phase [80]. This phase ends at approximately 1/2 ρ_s where a phase transition to homogeneous nuclear matter occurs at the boundary to the outer core. It is yet unknown whether there is a clear boundary between outer and inner core but various theoretical models have been proposed for the description of the composition of the inner core. It may be that homogeneous nuclear matter continues to the inner core, or that exotic states like hyperons, condensed kaons, pions, or deconfined quark matter (pure or mixed with hadrons) exist. Finally, we note that calculations within perturbative quantum chromodynamics (pQCD) are accurate for densities around $40\rho_s$ [81, 82], however, this regime is significantly higher than what is expected to be at the center of NSs (10 ρ_s).

Equation of state

The relation between pressure P, rest-mass density ρ, internal specific energy ϵ (or temperature T equivalently), and electron fraction Y_e (the ratio of the number of protons or electrons to the total number of baryons), $P = P(\rho, \epsilon, Y_e)$ defines the so-called EoS of a NS. The properties of NSs such as the mass, the radius, and its maximum mass depend on the underlying EoS. In cold NSs, the pressure and the internal specific energy are only functions of the rest-mass density, while

[1] The term cold refers to the fact that the nucleon Fermi energy is significantly higher than the nucleon thermal energy.

the electron fraction Y_e is determined by the beta-equilibrium condition. The NS EoS is yet only incompletely known and a unique model for the inner core does not exist (see [83,84] for a review on various EoS models and [74] for a discussion on the different parametrizations of the EoS).

1.3. Post-merger GW spectrum

The GW signal in the post-merger phase consists of different frequency components associated with various oscillation modes and quasilinear combination tones excited during the merger. Figure 1.2 shows a typical GW spectrum of the post-merger phase. The dominant feature is connected to the quadrupolar oscillation mode f_{peak} (see [27,31–47]). The frequency f_{peak} depends on the EoS. In addition, there are several secondary features in the post-merger GW signal. Two of those, the frequencies f_{2-0} and f_{2+0}, originate from a non-linear coupling between the frequency f_{peak} and the quasi-radial oscillation mode f_0 (see [27,42]). The frequencies $f_{2\pm0}$ are combination tones and are expected to produce frequency peaks at approximately $f_{2\pm0} \approx f_{\text{peak}} \pm f_0$. Another component, f_{spiral}, is connected to the orbital motion of the two antipodal tidal bulges formed during the merger phase (see [28]). These bulges have a lower angular velocity than the inner remnant and thus the frequency f_{spiral} is typically lower than f_{peak}. This frequency component is a dynamical feature and typically lasts only a few milliseconds. In this work, we discover a new coupling mechanism between f_{spiral} and the quasi-radial mode f_0 (see Sec. 4.1.3).

1.4. Post-merger GW templates

To detect the post-merger GW phase, robust and efficient data analysis techniques are needed. Currently, there are two main approaches. In the first one, morphology-independent methods are employed [85,86]. The second one is based on matched-filtering techniques, which require accurate GW post-merger template banks. In this work, we focus on the latter method.

The authors in [42] introduced a time-domain analytic model, which utilizes a combination of three exponentially decaying sinusoids. The model incorporated the dominant post-merger peak f_{peak} and the two most significant secondary frequency components, f_{spiral} and f_{2-0}, that also correlate with the binary's properties. Informed by numerical relativity simulations, the authors in [41,63–65] introduced frequency-domain models, and time-domain models were introduced in [38,66–70]. A frequency-domain model (which can be inverted to the time domain) for the amplitude and phase of the spectra, using a principal component analysis (PCA), was developed in [41]. A frequency domain hierarchical model, which generates amplitude spectra, was introduced in [64]. The authors in [65] introduced a frequency-domain amplitude model, which utilizes Lorentzian functions, in combination with relations connecting binary properties to the post-merger characteristic features. A time-domain analytical model based on the morphology of the post-merger waveforms (using numerical relativity informed

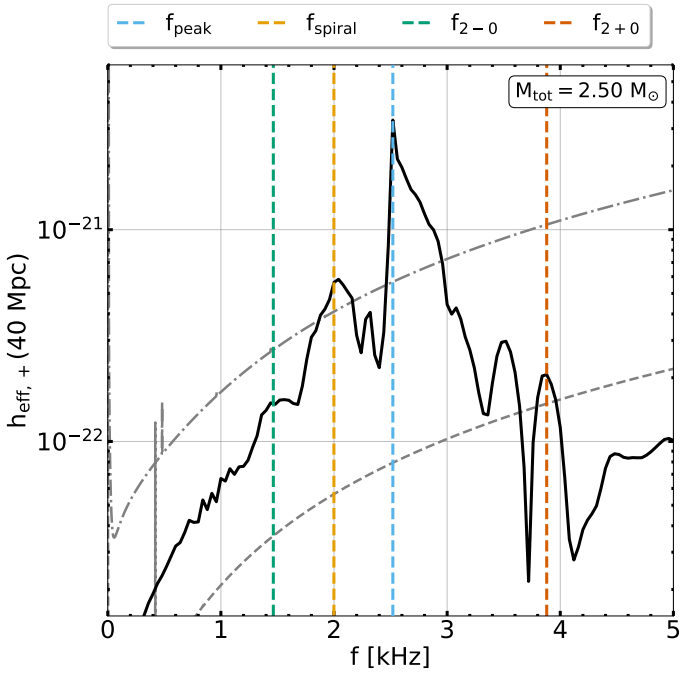

Figure 1.2: GW spectrum for the post-merger phase. Colored dashed vertical lines indicate the frequency peaks $f_{\rm peak}, f_{\rm spiral}, f_{2-0}, f_{2+0}$. The dash dotted curves denote the design sensitivity Advanced LIGO [2] and of the Einstein Telescope [3], respectively. Figure adapted from [4].

relations), which can be combined with an inspiral waveform, was constructed in [70]. Lastly, [68] introduced a time-domain analytic model that uses exponentially damped sinusoids (as in [42]) and includes three frequency components. For all frequency components in the model, a constant linear frequency-drift term was introduced.

To develop faithful post-merger GW templates, it is important to understand the underlying physical mechanisms, which dictate the different features of the GW spectrum. The GW spectrum is complex and although some of its properties are well studied and understood others are not.

In this thesis, the spectral properties of the post-merger phase along a sequence of equal-mass binary NS merger simulations with increasing total mass are compared. We observe a smooth transition of spectral features along this sequence as anticipated in [28]. We examine the time evolution of the dominant frequency component $f_{\rm peak}$ in the GW spectra (see also [68]) and using spectrograms we propose a time-dependent 2-segment piecewise analytic function, which models such a frequency drift.

Furthermore, we identify a new coupling mechanism between the tidal antipodal bulges ($f_{\rm spiral}$, see [28]) and the quasi-radial mode (f_0). This coupling leads to two frequency peaks in the GW spectra of high-mass models. We find that this new feature is important for the construction of accurate GW templates for systems with binary masses near the threshold mass to prompt collapse.

We construct a time-domain analytic model (based on [42]) for the post-merger

GW emission, which incorporates the four frequency components ($f_{\rm peak}$, $f_{\rm spiral}$, $f_{2\pm0}$) and allows a time-dependent description of the $f_{\rm peak}$ component. We develop a hierarchical procedure to determine the analytic model's parameters. The performance of our analytic model is evaluated using the noise-weighted fitting factor (FF) which is a measure that quantifies the match between the model and the waveform (see Eq. (5.6), (5.7) for the definition). The latter remains higher than ~ 0.96 along the entire sequence of binary models considered. These high FFs are comparable to, and in some cases even higher than, those of the best-performing fits presented in [64, 65, 68, 70].

Our new analytic model consists of physical parameters only, which is why the model is also helpful to understand the general dynamics and dependencies of the merger and its GW signal. We find that all the parameters correlate with the total binary mass of the system. The model can be used for the detection and parameter estimation of the post-merger phase in upcoming searches with upgraded second-generation detectors, such as aLIGO+ and aVirgo+ (see [55]), with future, third-generation (Einstein Telescope [56] and Cosmic Explorer [57]) or with dedicated high-frequency detectors [58–62]. Since the model is based on physical parameters, it elucidates the mechanisms shaping the spectra and how those depend on the binary mass.

1.5. Quasi-radial oscillation modes

Accurate post-merger GW templates are necessary for the successful detection of GWs from the post-merger phase and a precise measurement of $f_{\rm peak}$ would already put constraints on the EoS. In this work, we also address the question of whether secondary frequency components in the GW spectrum contain additional information about the EoS. To this end, we investigate the properties of the quasi-radial oscillation modes in NS merger remnants. These couple to the $f_{\rm peak}$ mode and are responsible for several secondary frequency components in the GW post-merger spectrum.

Radial modes in non-rotating stars are the simplest modes (see [87]). They provide information about the stability of the configuration in study and are typically used in validation tests in general relativistic numerical simulations. In those, the frequency of the radial oscillation mode extracted from the simulation is compared to the corresponding frequency computed from perturbation theory. Since the radial modes are spherical, they do not emit GWs, however, the situation is different for NS merger remnants (see [27, 28]). In remnants, the quasi-radial oscillation mode f_0 can couple to the quadrupolar frequency $f_{\rm peak}$ (see [27], Chapter 4) or to the $f_{\rm spiral}$ frequency (see Chapter 4) and thus produce secondary frequency components in the GW spectrum, $f_{2\pm0}$ and $f_{\rm spiral\pm0}$, respectively. As the total binary mass increases the NSs become more compact, the impact velocities are larger, and thus the quasi-radial oscillation mode is strongly excited. The latter is investigated in Chapter 4 (and also in [27, 28]), where we show that, for a specific EoS, the amplitude of the f_0 oscillation is an increasing function of $M_{\rm tot}$.

As previously mentioned and also discussed in Chapter 5, secondary compo-

nents in the post-merger GW spectrum are crucial for the construction of accurate post-merger GW templates. In this work, we show that additional information about the EoS can be extracted from the secondary components connected to the quasi-radial oscillation mode f_0. We consider a scenario of an accurate measurement of the total mass $M_{\rm tot}$, the dominant frequency component $f_{\rm peak}$, and the quasi-radial frequency f_0. The frequency f_0 can be derived from f_{2-0} or f_{2+0} in combination with $f_{\rm peak}$ or by measuring $f_{\rm spiral}$ and $f_{\rm spiral-0}$ or $f_{\rm spiral+0}$. We propose a method for determining the threshold mass $M_{\rm thres}$ for prompt BH formation, with an average error of 0.040 $M_\odot$, using the knowledge of $M_{\rm tot}, f_{\rm peak}, f_0$. Then, we employ empirical relations such as those introduced in [5], which connect $M_{\rm thres}$, $M_{\rm max}$, and $R_{1.6}$, to predict the maximum mass $M_{\rm max}$ of a non-rotating NS. This method exhibits an average error of 0.068 $M_\odot$.

1.6. Goals and outline

In this section we summarize the goals of this work and provide an outline of this thesis. This work addresses several questions, the first one being whether the spectral features in the GW emission from NS merger remnants systematically depend on the bulk properties of the system such as the total binary mass. Another question is whether the GW post-merger emission can be described with relatively simple analytic models, and if the parameters involved depend on the properties of the system. To this end, we simulate a sequence of NS mergers with increasing mass using the fully general relativistic Einstein Toolkit code. Furthermore, we address the question of whether secondary components in the GW spectrum can be used in order to obtain information about the so far incompletely known EoS. For this, we construct one of the largest library of NS merger simulations created so far, with varying total binary mass, mass ratio, and EoS model using the SPH code. With this library, we study the quasi-radial oscillation modes in NS merger remnants which are responsible for coupling mechanisms which produce secondary features in the GW spectrum. More specifically, the following questions are addressed throughout this work:

- Do the GW spectral properties of NS merger remnants systematically depend on the total binary mass ?
- Does the quadrupolar mode $f_{\rm peak}$ exhibit a time-dependent frequency evolution and how can it be described?
- Which of the secondary frequency components of the GW post-merger spectrum are most pronounced at different binary mass regimes?
- Do configurations with a total binary mass close to the threshold mass for prompt collapse exhibit additional frequency components in their GW spectrum?
- Is it possible to describe the GW post-merger emission with an analytic model which consists of exponentially decaying sinusoids and how well would it perform for a wide range of total binary masses?

- What is the appropriate complexity level of the analytic model (defined by the number of components) in order to obtain sufficiently high fitting factors?
- Are the parameters of the analytic model smooth functions of some characteristic property of the system, and if so, can a purely analytic model be constructed?
- Can we use the secondary frequency components in the GW post-merger spectrum to further constrain the EoS ?

The thesis is structured as follows: In Chapter 2 we present the different formulations for constructing initial data, and performing 3-dimensional simulations of NS mergers in numerical relativity. We also describe the additional implementations introduced to the codes throughout this work. In Chapter 3 we describe the data sets of binary NS merger simulations that were constructed and used throughout this work. In Chapter 4 we discuss the spectral properties of the GW post-merger signal for a sequence of binaries of increasing total binary mass in general relativity. In Chapter 5 we present a new analytic model for the gravitational wave emission in the post-merger phase in NS merger remnants. We evaluate its performance and construct analytic relations for the model's parameters. In Chapter 6 we discuss specific configurations with total mass close to the threshold for prompt collapse and introduce two modifications to the analytic model. In Chapter 7 we discuss the quasi-radial oscillation modes in NS merger remnants and using those, we introduce a scheme for the prediction of threshold mass for prompt collapse and maximum mass of a NS. In Chapter 8 we summarize the findings of this thesis, discuss the conclusions and ideas about future work directions. In Appendix A we assess the impact of residual eccentricity in the initial data, the resolution, and the assumption of pi-symmetry on our results. In Appendix B we include more detailed information on the results discussed in Chapter 4 and Chapter 5. In Appendix C we present empirical relations for the frequencies $f_{\rm spiral}, f_{\rm spiral-0}, f_0$ using the symmetric binary data set described in Chapter 3.

1.7. Conventions

Unless otherwise noted, we employ a dimensionless system of units for which $c = G = M_\odot = 1$. Throughout this work, the Latin indices range from 1 to 3, while the Greek indices range from 0 to 3. As in Einstein's summation rule, repeated indices correspond to summation. The symbol Δ represents the Laplace operator defined in the flat spatial metric. The flat space metric signature is $(-,+,+,+)$. The binray mass ratio is defined as $q = m_1/m_2$, where m_1, m_2 are the masses of the companion stars with $m_1 > m_2$. For the analysis of the GW spectra, the effective GW spectrum defined as $h_{\rm eff,+}(f) = f \cdot \widetilde{h}_+(f)$, where $\tilde{h}_+(f)$ is the Fourier transform of the strain $h_+(t)$, is used.

2. Numerical methods

In this chapter, we describe the theory regarding the simulation tools used in this work. First, we briefly introduce the basic theory of numerical relativity, that is the Arnowitt–Deser–Misner (ADM) spacetime decomposition. We discuss the construction of initial conditions for binary NS merger simulations in general relativity using the `LORENE` code [88, 89]. We describe the two (numerical relativity) simulation tools employed in this work: a) the Einstein Toolkit [90] which is a fully general relativistic grid-based code b) a smooth particle hydrodynamics (SPH) code [91, 92] where gravity is solved under the conformal flatness condition (CFC) [93, 94]. Finally, we discuss two additional implementations we incorporated, namely the inclusion of tracer particles in general relativity and a scheme for the reduction of residual eccentricities in the initial conditions of binary NS mergers.

2.1. The ADM formalism

The spacetime is described by the ADM formalism [95]. The spacetime is foliated in spacelike, non intersecting, hypersurfaces Σ_t which are parametrized with respect to a global time function t. Under these considerations, a general spacetime metric $g_{\mu\nu}$ can be expressed in the form

$$g_{\mu\nu} = \gamma_{\mu\nu} - n_\mu n_\nu, \tag{2.1}$$

where $\gamma_{\mu\nu}$ is the so-called *induced spatial metric* on each hypersurface Σ_t, and n^μ is a unit timelike vector normal to the hypersurface Σ_t. γ^ν_μ is used to project spacetime vectors and tensors to the spatial hypersurface Σ_t. The general line element is given by

$$ds^2 = (-\alpha^2 + \beta_i\beta^i)dt^2 + 2\beta_i dt dx^i + \gamma_{ij}dx^i dx^j. \tag{2.2}$$

where the metric potentials α and β^i are the lapse function and shift vector, respectively.

2.2. Initial data: Lorene

We construct initial data (ID) of circular quasiequilibrium solutions using the `LORENE` library [88,89]. These are used for all the simulations, in this work, carried out with the Einstein Toolkit (see Sec. 2.3). `LORENE` incorporates a spectral solver

which provides an accurate mapping of the ID to the computational grid of the evolution code.

For the construction of quasiequilibrium states the following assumptions are made: a) The spacetime is solved under the CFC approximation [93, 94] and thus the gravitational radiation is neglected, b) The individual stars' velocity profiles are either irrotational or rigid, c) the system is in equilibrium in the co-rotating frame. These assumptions imply the existence of a *helical* Killing vector (see [89]) that in the ADM formalism reads

$$\xi^{\mu} = (\partial_t)^{\mu} + \Omega\ (\partial_{\phi})^{\mu}, \tag{2.3}$$

where Ω is a constant referring to the orbital angular velocity of the binary, t and ϕ are the coordinate time and azimuthal coordinate, respectively.

The spacetime is obtained by solving the five elliptic differential equations derived from Einstein's equations under the CFC approximation, and the maximal slicing condition (see [89] for more details, and Sec. 2.6).

2.3. The Einstein Toolkit

The Einstein Toolkit is an open-source code [90] for 3-dimensional hydrodynamical simulations in general relativity. The evolution of hydrodynamics is carried out in a grid-based approach employing the Valencia formulation [96, 97]. In the Einstein Toolkit, this formulation is implemented in the `GRHydro` module [98, 99]. The spacetime is evolved in a fully general relativistic manner using either the BSSN [100–102] or the Z4c [103, 104] formulation. These evolution schemes have been used extensively in the literature (see [105] and references therein). In Sec. 2.3.2 we further discuss these formulations. The Z4c formulation is implemented in the `CTGamma` [106, 107] module, which is not part of the Einstein Toolkit code. Nevertheless, due to the modular nature of the code we imported it to our version of the code.

2.3.1. The Valencia formalism

We present the formulation for relativistic hydrodynamics typically employed by grid-based codes such as the Einstein Toolkit. The evolution of hydrodynamics is carried out according to the Valencia formulation [96, 97]. Because we do not include magnetic fields in our simulations, we only discuss the original Valencia formulation (see [96, 97]).

The fluid is described by the energy-momentum tensor of a *perfect fluid* which is defined as

$$T^{\mu\nu} = \rho h u^{\mu} u^{\nu} + P g^{\mu\nu}, \tag{2.4}$$

where ρ is the rest-mass density, P is the pressure, h is the relativistic enthalpy defined as $h = 1 + P/\rho + \epsilon$, ϵ is the specific internal energy and u^{μ} is the four-velocity of the fluid. The pressure is a function of ρ and ϵ, that is, $P = P(\rho, \epsilon)$,

however it can also depend on the electron fraction Y_e (see Sec. 1.2). To evolve the hydrodynamics we utilize the following local conservation laws

$$\begin{aligned} \nabla_\mu j^\mu &= 0, & (2.5)\\ \nabla_\mu T^{\mu\nu} &= 0, & (2.6) \end{aligned}$$

where ∇_μ corresponds to the covariant derivative with respect to the spacetime metric $g_{\mu\nu}$. The first equation, Eq. (2.5) is a continuity equation and refers to the conservation of the current of rest-mass defined as $j^\mu = \rho\ u^\mu$. The second equation, Eq. (2.6), denotes the conservation of the energy-momentum tensor $T^{\mu\nu}$. Eq. (2.5)-(2.6) form a set of five equations which are used to determine the evolution of hydrodynamical variables (ρ, u_i, ϵ) or variations of those.

In this framework, the Eulerian observers whose four-velocity is equal to n^μ, measure the fluid velocity as

$$\begin{aligned} v^i &= \frac{1}{\alpha}\left(\frac{u^i}{u^0} + \beta^i\right) \\ &= \frac{u^i}{W} + \frac{\beta^i}{\alpha}, & (2.7) \end{aligned}$$

where W is the Lorentz factor between the Eulerian observer and the fluid velocity u^μ with $W \equiv -n_\alpha u^\alpha = \alpha\ u^0$. Subsequently, we define a new set of variables, the *conserved variables*: the conserved density D, the conserved momentum S_j, and the conserved energy density τ

$$\begin{aligned} D &= \sqrt{\gamma}\rho W, & (2.8)\\ S_j &= \sqrt{\gamma}\rho h W^2 \upsilon_j, & (2.9)\\ \tau &= \sqrt{\gamma}(\rho h W^2 - p) - D. & (2.10) \end{aligned}$$

These are functions of $\rho, \upsilon_i, \epsilon$ which are typically called *primitive variables*. With the conservative variables, the system Eq. (2.5),(2.6) can be expressed in a hyperbolic flux-conservative form:

$$\frac{\partial \mathbf{U}}{\partial t} + \frac{\partial \mathbf{F}^i}{\partial x^i} = \mathbf{S}, \quad (2.11)$$

where the vectors $\mathbf{U}$, $\mathbf{F}^i$, and $\mathbf{S}$ are defined as

$$\mathbf{U} = \begin{bmatrix} D \\ S_j \\ \tau \end{bmatrix}, \quad (2.12)$$

$$\mathbf{F}^i = \alpha \cdot \begin{bmatrix} D\left(v^i - \frac{\beta^i}{\alpha}\right) \\ S_j\left(v^i - \frac{\beta^i}{\alpha}\right) + \sqrt{\gamma}P\delta^i_j \\ \tau\left(v^i - \frac{\beta^i}{\alpha}\right) + \sqrt{\gamma}Pv^i \end{bmatrix}, \quad (2.13)$$

$$\mathbf{S} = \alpha\sqrt{\gamma} \cdot \begin{bmatrix} 0 \\ T^{\mu\nu}\left(\frac{\partial g_{\nu j}}{\partial x^{\mu}} - \Gamma^{\lambda}_{\mu\nu} g_{\lambda j}\right) \\ \alpha\left(T^{\mu 0}\frac{\partial \ln \alpha}{\partial x^{\mu}} - T^{\mu\nu}\Gamma^{0}_{\mu\nu}\right) \end{bmatrix}. \tag{2.14}$$

In this form, Eq. (2.11) can be solved using finite-volume techniques, which perform well in the presence of discontinuities and shocks. As such, to evolve the conservative variables, the fluxes $\mathbf{F}^i$ at the cell faces have to be determined. This is achieved by solving the local Riemann problem at the cell interfaces. For this, the values of the fluid states (conservative variables) have to be computed on the left-hand side and right-hand side of the cell interface. This step is called *reconstruction* and is achieved by interpolation using knowledge of the fluid variables at the cell centers. In this work, we employ a weighted essentially non-oscillatory (WENO) [108,109] reconstruction scheme which can reach up to fifth order accuracy under a smooth flow of the fluid (see [99]). For the solution of the local Riemann problem, we use the HLLE Riemann solver [110]. Finally, from the updated conservative variables the primitive variables have to be recovered. The system of equations Eq. (2.8)-(2.10) is numerically solved for ρ, v_i, ϵ using the schemes introduced in [111].

2.3.2. Metric solvers

We discuss the two general relativistic formulations for the evolution of spacetime which are employed in this work, BSSN [100–102] and Z4c [103,104]. Both formulations employ conformal transformations where the spatial metric γ_{ij} is expressed as a product of a positive scaling factor (such as $e^{4\phi}$) and a background metric $\tilde{\gamma}_{ij}$. This concept is expanded to other objects (tensors) in order to express the Einstein's equations into a numerically stable hyperbolic form. In this work, we mainly employ the Z4c formulation.

BSSN

We present the evolution equations of the spacetime according to the BSSN formulation. We note that since we use the McLachlan implementation [112,113], the equations presented below are the same as in the works of [114,115] but with some modifications to the notation. By introducing appropriate conformal transformations, the evolved variables of the BSSN scheme read

$$\phi \equiv \log\left[\frac{1}{12}\det\gamma_{ij}\right], \tag{2.15}$$

$$\tilde{\gamma}_{ij} \equiv e^{-4\phi}\,\gamma_{ij}, \tag{2.16}$$

$$K \equiv \gamma^{ij}K_{ij} \tag{2.17}$$

$$\tilde{A}_{ij} \equiv e^{-4\phi}\left[K_{ij} - \frac{1}{3}\gamma_{ij}K\right], \tag{2.18}$$

$$\tilde{\Gamma}^{i} \equiv \tilde{\gamma}^{jk}\tilde{\Gamma}^{i}_{jk}, \tag{2.19}$$

where $e^{-4\phi}$ is the conformal factor and there $\tilde{\gamma}_{ij}$ refers to the background metric, K_{ij} is the extrinsic curvature which is provided by the ID, K is its trace (and thus $\tilde{A}_{ij}$ refers to the conformal traceless extrinsic curvature), and $\tilde{\Gamma}^i_{jk}$ refers to the Christoffel symbols for the metric $\tilde{\gamma}_{ij}$. The total number of these variables is 17 (1+6+1+6+3). The corresponding evolution equations read

$$\begin{aligned}
\partial_0 K &= -e^{-4\phi}\left[\tilde{D}^i\tilde{D}_i\alpha + 2\partial_i\phi\cdot\tilde{D}^i\alpha\right] + \alpha\left(\tilde{A}^{ij}\tilde{A}_{ij} + \frac{1}{3}K^2\right) \\
&\quad -\alpha S, && (2.20)\\
\partial_0\phi &= -\frac{\alpha}{6}K + \frac{1}{6}\partial_k\beta^k, && (2.21)\\
\partial_0\tilde{\gamma}_{ij} &= -2\alpha\tilde{A}_{ij} + 2\tilde{\gamma}_{k(i}\partial_{j)}\beta^k - \frac{2}{3}\tilde{\gamma}_{ij}\partial_k\beta^k, && (2.22)\\
\partial_0\tilde{A}_{ij} &= e^{-4\phi}\left[\alpha\tilde{R}_{ij} + \alpha R^\phi_{ij} - \tilde{D}_i\tilde{D}_j\alpha + 4\partial_{(i}\phi\cdot\tilde{D}_{j)}\alpha\right]^{TF} \\
&\quad + \alpha K\tilde{A}_{ij} - 2\alpha\tilde{A}_{ik}\tilde{A}^k_j + 2\tilde{A}_{k(i}\partial_{j)}\beta^k - \frac{2}{3}\tilde{A}_{ij}\partial_k\beta^k \\
&\quad -\alpha e^{-4\phi}\hat{S}_{ij}, && (2.23)\\
\partial_0\tilde{\Gamma}^i &= \tilde{\gamma}^{kl}\partial_k\partial_l\beta^i + \frac{1}{3}\tilde{\gamma}^{ij}\partial_j\partial_k\beta^k + \partial_k\tilde{\gamma}^{kj}\cdot\partial_j\beta^i - \frac{2}{3}\partial_k\tilde{\gamma}^{ki}\cdot\partial_j\beta^j \\
&\quad - 2\tilde{A}^{ij}\partial_j\alpha + 2\alpha\Big[(m-1)\partial_k\tilde{A}^{ki} - \frac{2m}{3}\tilde{D}^i K \\
&\quad +m(\tilde{\Gamma}^i_{kl}\tilde{A}^{kl} + 6\tilde{A}^{ij}\partial_j\phi)\Big] - S^i, && (2.24)
\end{aligned}$$

where $\partial_0 \equiv \partial_t - \beta^j\partial_j$, $m = 1$, the quantities with the ˜ symbol are connected to the background metric $\tilde{\gamma}_{ij}$, $\tilde{D}_i$ corresponds to the covariant derivative with respect to $\tilde{\gamma}_{ij}$, the operator $[..]^{\rm TF}$ refers to the traceless part of the expression in brackets, the quantities $\tilde{R}_{ij}$ and R^ϕ_{ij} are related to the Ricci tensor (see Eq. (17) and Eq. (18) of [114]), and the source terms $S, S_i, \hat{S}_{ij}$ depend on the energy-momentum tensor (and the Ricci tensor) and are defined in Eq. (16)-(18) of [115].

In addition, the system is supplemented by the evolution equations of the metric potentials, the lapse function α and the shift vector β^i. These, in their most general form, read

$$\begin{aligned}
\partial_0\alpha &= -\alpha^2 f(\alpha,\phi,x^\mu)(K - K_0(x^\mu)), && (2.25)\\
\partial_0\beta^i &= \alpha^2 G(\alpha,\phi,x^\mu)B^i, && (2.26)\\
\partial_0 B^i &= e^{-4\phi}H(\alpha,\phi,x^\mu)\partial_0\tilde{\Gamma}^i - \eta^i(B^i,\alpha,x^\mu), && (2.27)
\end{aligned}$$

where B^i is related to the time derivative of the shift vector β^i, and f, G, H, η are arbitrary functions. For the evolution of the lapse function we use the 1+log slicing where:

$$\begin{aligned}
f(\alpha,\phi,x^\mu) &\equiv 2/\alpha, && (2.28)\\
K_0(x^\mu) &\equiv 0. && (2.29)
\end{aligned}$$

The evolution of the shift vector is carried out under the Γ-driver method where:

$$G(\alpha, \phi, x^\mu) \equiv (3/4)\,\alpha^{-2}, \tag{2.30}$$
$$H(\alpha, \phi, x^\mu) \equiv e^{4\phi}, \tag{2.31}$$
$$\eta(B^i, \alpha, x^\mu) \equiv (1/2)\,B^i q(r), \tag{2.32}$$

with $q(r) = 1$ for a radial coordinate distance $r \leq R$ and $q(r) = R/r$ for $r > R$ with R being a large value of the order of 370 km. Thus seven (1+3+3) additional variables are evolved.

Furthermore, as shown in [75, 116], specific identities, commonly called constraints, must be satisfied in this system. They read

$$H \equiv R - \tilde{A}^{ij}\tilde{A}^{ij} + \frac{2}{3}K^2 - 16\pi\rho_{\mathrm{ADM}} = 0, \tag{2.33}$$
$$M^i \equiv \tilde{D}_j\tilde{A}^{ij} - \frac{2}{3}\tilde{D}^i K + 6\tilde{A}^{ij}\tilde{D}_j\phi = 0, \tag{2.34}$$

where R is the Ricci scalar, $\rho_{\mathrm{ADM}} = n_\alpha n_\beta T^{\alpha\beta}$. Eq. (2.33) is referred as the Hamiltonian constraint, and the Eq. (2.34) is the Momentum constraint [1]. These equations are satisfied with good precision during the construction of the ID (since these are the equations which are solved). However, in a numerical simulation, the constraint equations are only monitored and so, are used to estimate the errors in the simulation. The major difference between the BSSN and Z4c formulations is the treatment of the violation of the constraints, since the latter scheme incorporates a method to damp this violation. Finally, we note that depending on the exact evolution formulation (BSSN or Z4c), additional constraints for auxiliary quantities may exist. These are also monitored during the evolution, however, we do not present them in this work.

Z4c

We present the evolution equations for the spacetime according to the Z4c formulation, where we follow the implementation described in [103, 104]. The Z4c scheme originates from the more general Z4 formulation, which ensures that the violation of the constraint equations is damped. In this framework, Einstein's equations are replaced by

$$\begin{aligned} R_{\alpha\beta} + \nabla_\alpha Z_\beta + \nabla_\beta Z_\alpha &= 8\pi(T_{\alpha\beta} - \frac{1}{2}g_{\alpha\beta}T) \\ +\kappa_1[t_\alpha Z_\beta + t_\beta Z_\alpha &- (1+\kappa_2)g_{\alpha\beta}t_\gamma Z^\gamma], \end{aligned} \tag{2.35}$$

where Z_α is the four vector of the constraints H and M^i, t^α is a time-like vector field, and κ_1, κ_2 are constraint damping coefficients. When the constraints Z_α vanish, Eq. (2.35) reduce to Einstein's equations, and thus the solutions of Eq. (2.35) are also valid solutions of Einstein's equations. The Z4c scheme is derived from the Z4 formulation by neglecting specific terms of the Z4 evolution equations and

[1] The momentum constraint is expressed in terms of the conformal traceless extrinsic curvature, but generally is a function of the extrinsic curvature K_{ij}.

introducing appropriate conformal transformations which lead to a system that shares many similarities with the BSSN equations. The evolved variables read

$$\begin{aligned}
\chi &\equiv \gamma^{-\frac{1}{3}}, && (2.36)\\
\tilde{\gamma}_{ij} &\equiv \chi\, \gamma_{ij}, && (2.37)\\
\hat{K} &\equiv K - 2\Theta, && (2.38)\\
\tilde{A}_{ij} &\equiv \chi\, (K_{ij} - \frac{1}{3}\gamma_{ij} K), && (2.39)\\
\tilde{\Gamma}^i &\equiv 2\tilde{\gamma}^{ij} Z_j + \tilde{\gamma}^{ij}\tilde{\gamma}^{kl}\tilde{\gamma}_{jk,l}, && (2.40)\\
\Theta &= -n_\alpha Z^\alpha, && (2.41)
\end{aligned}$$

where $K = \gamma^{ij} K_{ij}$ is the trace of K_{ij}, and Z_j is the spatial projection of Z_α. The total number of these evolved variables is eighteen (1+6+1+6+3+1). The corresponding evolution equations read

$$\begin{aligned}
\partial_t \chi &= \frac{2}{3}\chi\Big[\alpha(\hat{K} + 2\Theta) - D_i\beta^i\Big], && (2.42)\\
\partial_t \tilde{\gamma}_{ij} &= -2\alpha\tilde{A}_{ij} + 2\tilde{\gamma}_{k(i}\partial_{j)}\beta^k - \frac{2}{3}\tilde{\gamma}_{ij}\partial_k\beta^k + \beta^k\partial_k\tilde{\gamma}_{ij}, && (2.43)\\
\partial_t \hat{K} &= -D_i D^i\alpha + \alpha[\tilde{A}_{ij}\tilde{A}^{ij} + \frac{1}{3}(\hat{K} + 2\Theta)^2\\
&\quad +\kappa_1(1-\kappa_2)\Theta] + 4\pi\alpha[S + \rho_{\rm ADM}] + \beta^i\partial_i\hat{K}, && (2.44)\\
\partial_t \tilde{A}_{ij} &= \chi\Big[-D_iD_j\alpha + \alpha\tilde{R}_{ij} + \alpha R^\chi_{ij} - 8\pi\alpha S_{ij}\Big]^{\rm tf} + \alpha\Big[(\hat{K} + 2\Theta)\tilde{A}_{ij}\\
&\quad -2\tilde{A}_{ik}\tilde{A}^k{}_j\Big] + 2\tilde{A}_{k(i}\partial_{j)}\beta^k - \frac{2}{3}\tilde{A}_{ij}\partial_k\beta^k + \beta^k\partial_k\tilde{A}_{ij}, && (2.45)\\
\partial_t \tilde{\Gamma}^i &= \tilde{\gamma}^{jk}\partial_j\partial_k\beta^i + \frac{1}{3}\tilde{\gamma}^{ij}\partial_j\partial_k\beta^k - 2\tilde{A}^{ij}\partial_j\alpha\\
&\quad +2\alpha\big[\tilde{\Gamma}^i{}_{jk}\tilde{A}^{jk} - \frac{3}{2}\tilde{A}^{ij}\partial_j\ln\chi - \frac{1}{3}\tilde{\gamma}^{ij}\partial_j(2\hat{K} + \Theta)\\
&\quad -\kappa_1(\tilde{\Gamma}^i - \tilde{\Gamma}_{\rm d}{}^i) - 8\pi\tilde{\gamma}^{ij}S_j\big] + \frac{2}{3}\tilde{\Gamma}_{\rm d}{}^i\partial_j\beta^j - \tilde{\Gamma}_{\rm d}{}^j\partial_j\beta^i\\
&\quad +\beta^j\partial_j\tilde{\Gamma}^i, && (2.46)\\
\partial_t\Theta &= \frac{1}{2}\alpha\big[R - \tilde{A}_{ij}\tilde{A}^{ij} + \frac{2}{3}(\hat{K} + 2\Theta)^2 - 16\pi\rho_{\rm ADM}\\
&\quad -2\kappa_1(2+\kappa_2)\Theta\big] + \beta^i\partial_i\Theta, && (2.47)
\end{aligned}$$

where $\rho_{\rm ADM} = n_\alpha n_\beta T^{\alpha\beta}$, $S_i = -\gamma_{i\alpha} n_\beta T^{\alpha\beta}$, $S_{ij} = \gamma_{i\alpha}\gamma_{j\beta}T^{\alpha\beta}$, and $\tilde{\Gamma}_{\rm d}{}^i = \tilde{\gamma}^{jk}\tilde{\Gamma}^i{}_{jk}$. As before, the quantities with the $\tilde{}$ symbol are connected to the background metric $\tilde{\gamma}_{ij}$, the operator $[..]^{\rm TF}$ refers to the traceless part of the expression in the brackets, $\tilde{R}_{ij}$ and R^χ_{ij} are connected to the Ricci tensor and are defined in Eq. (20)-(21) of [103]). Evidently, this system of equations shares some similarities with the BSSN system Eq.(2.20)-Eq.(2.24) with one additional evolution equation for Θ.

As before, for the evolution of the lapse function α we employ the 1+log slicing where we replace K and K_0 with $\hat{K}$ and $\hat{K}_0$ in (2.25), respectively. The evolution

of the shift vector is carried out using the Γ-driver (see Eq. (2.26)-(2.27)). Finally, the Hamiltonian and Momentum constraints in Z4c formulation are given by

$$H = R - \tilde{A}^{ij}\tilde{A}_{ij} + \frac{2}{3}(\hat{K} + 2\Theta)^2 - 16\pi\rho_{\rm ADM}, \tag{2.48}$$

$$M^i = \partial_j \tilde{A}^{ij} + \tilde{\Gamma}^i{}_{jk}\tilde{A}^{jk} - \frac{2}{3}\tilde{\gamma}^{ij}\partial_j(\hat{K} + 2\Theta) - \frac{3}{2}\tilde{A}^{ij}\partial_j(\log\chi). \tag{2.49}$$

$$\tag{2.50}$$

Numerical implementations

The implementation of the BSSN formulation is the McLachlan code [112, 113], which is included in the Einstein Toolkit code, and is the default evolution formulation. For the Z4c formulation, we couple the `CTGamma` module to the Einstein Toolkit. The module is based on the same code infrastructure, namely the Cactus code and thus, the coupling to the Einstein Toolkit is relatively straightforward. The time integration of the equations of the BSSN and Z4c formulations is accomplished with the method of lines scheme [117]. In this, the spatial partial derivatives are approximated with finite differences, while the time derivatives ∂_t are kept intact. In this form, the system becomes a system of ordinary differential equations. We evolve it in time using a fourth order Runge-Kutta (RK4) time integration. The spatial partial derivatives are approximated using fourth order finite differences.

2.4. Implementation of tracers

In this section we describe our implementation of tracer particles (also called tracers) in the Einstein Toolkit code. Tracers are particles which simply follow the flow, that is the (coordinate) velocity field, of the fluid. They do not interact with matter and do not influence the dynamics of the system. By interpolating, one can obtain the value of any scalar or vector field at the position of the tracers.

For a tracer particle a with coordinates x^i, we use interpolation to determine its coordinate velocity at time t. Then the coordinate velocity can be used as an equation of motion of the tracer particle a by integrating

$$\frac{dx^i}{dt} = \bar{v}^i, \tag{2.51}$$

where $\bar{v}^i$ is the coordinate velocity at the position x^i. The coordinate velocity $\bar{v}^i$ is connected to the four velocity u^i of the fluid as

$$\bar{v}^i = \frac{dx^i}{dt} = \frac{dx^i}{d\tau}\frac{d\tau}{dt} = \frac{u^i}{u^0} \qquad \text{for i=1,2,3.} \tag{2.52}$$

Because the Einstein Toolkit employs the Valencia formulation (see Sec. 2.3.1), the fluid velocity field measured by the Eulerian observer, denoted by $v^i_{\rm ET}$ in this

section for simplicity, is given by

$$v^i_{\rm ET} = \frac{1}{\alpha}\left(\frac{u^i}{u^0}+\beta^i\right). \tag{2.53}$$

By inserting (2.52) into (2.53) we derive the expression for the coordinate velocity $\bar{v}^i$ as a function of $v^i_{\rm ET}$, the lapse function α, and shift vector $\beta^{\rm i}$:

$$\bar{v}^i = \alpha\, v^i_{\rm ET} - \beta^i. \tag{2.54}$$

Thus the coordinate velocity $\bar{v}^i$ at any position in space is calculated by interpolating the quantities $v^i_{\rm ET}, \alpha, \beta^i$ which are stored during the simulation. We numerically integrate Eq. (2.51) in time t for every tracer particle using a Runge-Kutta of second order (RK2) and finally update their respective coordinate x^i.

2.5. Reduction of eccentricity

In this section we discuss a scheme to reduce the residual eccentricity in the ID. More specifically, we implement a modified version of the prescription introduced in [118], and adapt it to the equations used in the `LORENE` code. This implementation improves the quality of our simulations since it leads to more realistic ID. This is because gravitational radiation is expected to circularize the orbits in the final stages of the inspiral [119]. Although the implementation itself is not lengthy, a good understanding of the code and the formulation employed by `LORENE` is necessary.

To reduce the residual eccentricity in the ID, the velocity field of the quasi-equilibrium solution is changed by imposing an additional appropriate approaching velocity component. As previously mentioned, for the quasi-circular (QC) solutions we assume the existence of a helical symmetry Killing vector (see Eq. (2.3)). For the correction we introduce the conformal Killing vector

$$\xi^\mu = (\partial t)^\mu + \Omega\,(\partial\phi)^\mu - \upsilon_\pm(\partial x)^\mu, \tag{2.55}$$

where we assume that the stars are on the x coordinate axis, the quantities υ_+ and υ_- apply to the stars for $x>0$ and $x<0$, respectively, and $\upsilon_+ - \upsilon_- = 2\upsilon$ with υ being a constant.

As explained in [118] the spacetime field equations are unaffected by the replacement of (2.3) with (2.55). However, since the approaching velocity is not compatible with the spacetime symmetry (in the co-moving frame), the hydrostatic equilibrium cannot be obtained. To this end, we only modify the (converged) quasi-circular solution with (2.55) using a relatively small υ. The change in ξ^μ enters the hydrodynamics equations via the considered observer with four velocity parallel to ξ^μ (for more information see Eq(21)-(26) of [118]).

We determine the appropriate approaching velocity correction υ with an iterative procedure using several successive simulations. We note that we use a slightly modified version of the scheme described in [118]. The first iteration corresponds to the simulation using the quasi-circular ID, and therefore $\upsilon = 0$ and $\Omega = \Omega_{\rm QC}$ is

the orbital frequency of the QC solution provided by LORENE. We model the time evolution of the separation distance $d(t)$ with the function

$$s(t) \;=\; A_0 + A_1\ t + A_2\ t^2 + B\ \sin(\omega t + \phi_0). \tag{2.56}$$

where $A_0, A_1, A_2, B, \omega, \phi_0$ are free parameters. The polynomial terms $(A_0 + A_1\ t + A_2\ t^2)$ mimic the shrinking of the orbit due to the GW radiation, whereas the modulation term $(B\ \sin(\omega t + \phi_0))$ is connected to the residual eccentricity of the system. For perfectly circular orbits the parameter B vanishes $(B \to 0)$. To minimize the modulation term $B\ \sin(\omega t + \phi_0)$ and circularize the orbits, the appropriate corrections to the orbital angular velocity Ω $(\delta\Omega)$ and approaching velocity v have to be determined.

We calculate the time evolution of the separation distance $d(t)$, assuming that the latter is equal to the coordinate distance between the centers of the two stars. We also assume that the centers of the stars coincide with the cells with the maximum rest-mass density, respectively. We only use their coordinates in the orbital plane $(x_\mathrm{i}, y_\mathrm{i})$ for i=1,2. With these considerations the separation distance $d(t)$ is given by

$$d(t) \;=\; \sqrt{(x_1 - x_2)^2 + (y_1 - y_2)^2}. \tag{2.57}$$

We note that $d(t)$ is slightly noisy most likely because of the assumption that the positions of the centers of the stars coincide with the cells with the maximum rest-mass density. As a result, these positions are discretized and, at close times, create a noise around the actual center. For this reason, we perform an averaging between every five data points in the time series. We also discard the first 1-3 ms of $d(t)$ because this part of the simulation is dominated by the relaxation of the ID (computed under the CFC approximation) to the general relativistic dynamical variables (see the discussion in [118]). Then we perform an analytic fit on $d(t)$ using the model function Eq. (2.56) and extract the quantities B, ω, ϕ_0. We present the expressions for the corrections in $\delta\Omega$ and v as presented in [118] but with respect to the variables B, ω, ϕ_0 used in this work. They read

$$\delta\Omega \;=\; +\frac{\omega^2 B}{2\Omega d}\sin(\phi_0), \tag{2.58}$$

$$v \;=\; -\frac{B\omega}{2}\cos\phi_0, \tag{2.59}$$

where d is the initial separation distance of the system and Ω is the orbital frequency of the system. The eccentricity can be approximated from the relation $e \approx \frac{B}{d\omega}$. This procedure is repeated (roughly three times) until the eccentricity e decreases significantly and thus the orbit is circularized.

We performed this iterative procedure using both spacetime evolution schemes (BSSN and Z4c). We find that generally the inspiral phase with the Z4c evolution scheme exhibits systematically lower residual eccentricities compared to that of BSSN. This trend is observed even in simulations of the QC ID (without applying any reduction in e). The reduction of eccentricity also performs best with the Z4c scheme leading to significantly lower values of e, when convergence is reached,

compared to when the BSSN evolution scheme is employed. One reason for this behavior may be the treatment of the violation of constraints. As the inspiral evolves, the errors in the BSSN formulation are stationary, while in the Z4c formulation they are propagated away (see [103]). Therefore in the former case, the errors are accumulated in the area where the inspiral takes place, and this may influence the orbit and lead to higher values of e.

2.6. The SPH code

In this section we describe the relativistic SPH code [91, 92]. As previously mentioned, the spacetime is described by the ADM spacetime decomposition where the general metric takes the form of Eq. (2.2). The evolution of hydrodynamics is carried out with the relativistic smooth particle hydrodynamics formalism (see [91])[2].

Spacetime

More specifically, the spacetime is evolved under the so-called CFC (conformal flatness condition) approximation which assumes a spatial metric of the following form

$$\gamma_{ij} = \psi^4 \, \delta_{ij}, \tag{2.60}$$

where ψ is the conformal factor. We choose the maximal slicing condition which states that the trace of the extrinsic curvature K_{ij} and each partial time derivative are zero, $\partial_t K = K = 0$. Under these conditions, Einstein's equations can be converted into a set of five elliptic differential equations [94, 120]:

$$\Delta\psi = -2\pi\psi^5 E - \frac{1}{8}\psi^5 K_{ij}K^{ij}, \tag{2.61}$$

$$\Delta(\alpha\psi) = 2\pi\alpha\psi^5(E+2S) + \frac{7}{8}\alpha\psi^5 K_{ij}K^{ij}, \tag{2.62}$$

$$\Delta\beta^i + \frac{1}{3}\partial^i\partial_j\beta^j = 16\pi\alpha\rho W\hat{u}_i + 2\psi^{10}K^{ij}\partial_j\left(\frac{\alpha}{\psi^6}\right) \equiv S_\beta, \tag{2.63}$$

where the quantities E and S are the matter contributions and $\rho, P, W, \hat{u}_i$ are defined below. In the CFC maximal slicing approximation the extrinsic curvature K_{ij} is given by

$$K_{ij} = \frac{\psi^4}{2\alpha}\left(\delta_{il}\partial_j\beta^l + \delta_{jl}\partial_i\beta^l - \frac{2}{3}\delta_{ij}\partial_k\beta^k\right). \tag{2.64}$$

Furthermore, Eq. (2.63) can be transformed into a set of two Poisson-like equations by introducing a new auxiliary vector field B^i of the form $B^i = \beta^i + \frac{1}{4}\partial^i\chi$

[2] Although some of the variable symbols used in this section are also used in Sec. 2.3, we remark that these variables are separate since the two codes are independent and the formulations are different.

[91]. By inserting $\beta^i(B^i, \partial^i\chi)$ to Eq. (2.63), the system reads

$$\Delta B^i = S_\beta, \tag{2.65}$$
$$\Delta\chi = \partial_i B^i. \tag{2.66}$$

As a result, all the spacetime fields ψ, α, β^i can be evolved by solving the aforementioned set of Poisson-like differential equations Eq. (2.61),(2.62), (2.65),(2.66). To solve these equations we use a multi-grid solver [121] on an overlaid (Cartesian) grid. Because ψ, α, B^i appear in the source terms, an iterative procedure is employed until convergence is achieved, where we choose as an initial guess the solution of the previous step. Since the hydrodynamics are described by the SPH scheme (see below) we obtain the values of the hydrodynamical variables (which also enter the source terms) at the grid positions using the typical SPH mapping, which is described below. The spacetime fields at the positions of the SPH particles are computed using a third order interpolation. For the boundary conditions for the fields in the source terms of Eq. (2.61),(2.62) we employ a multipole expansion up to quadrupole order, while for the shift related quantities B^i, χ in Eq (2.65),(2.66) we impose a fall-off law [92].

Finally, we remark that in the CFC condition the emission of GWs is neglected. For this reason the GW radiation is externally computed using the slow-motion quadrupole formalism, described in [91]. In addition, a back-reaction force prescription is implemented in order to mimic the loss of energy and angular momentum (see [91]).

Hydrodynamics

The matter fields are described by the energy-momentum tensor $T_{\mu\nu}$ of a perfect fluid (see Eq. (2.4)). The quantities $\rho, h, \epsilon, P, u^\mu$ have the same meaning as in Sec. 2.3.1. The matter fields enter the spacetime equations Eq. (2.61)-(2.66) with the terms $E = \rho h W^2 - P$ and $S = \rho h(W^2 - 1) + 3P$, where $W = \alpha u^0 = \sqrt{1 + \gamma_{ij}u^i u^j}$. As in the Valencia formulation (see Sec. 2.3.1) we define the conserved variables: the conserved density ρ^*, conserved momentum $\hat{u}$, and conserved specific internal energy τ :

$$\rho^* = \rho\alpha u^0\psi^6, \tag{2.67}$$
$$\hat{u}_i = hu_i = h\left(\bar{v}_i + \beta_i\right)\psi^4 u^0, \tag{2.68}$$
$$\tau = hW - \frac{P}{\rho W} - \sqrt{1 + \frac{\hat{u}_i\hat{u}_j\delta^{ij}}{\psi^4}}. \tag{2.69}$$

These variables are derived from primitive variables $\rho, \bar{v}^i, \epsilon$, where $\bar{v}^i$ refers to the coordinate velocity field. The latter is connected to the four velocity u^i by the relation $\bar{v}^i = u^i/u^0$. The relativistic SPH hydrodynamics follow a Lagrangian approach, and so, the equations of hydrodynamics are solved on the co-moving

frame. The Lagrangian relativistic hydrodynamics equations read

$$\frac{d}{dt}\rho^* = -\rho^* \partial_i \bar{v}^i, \tag{2.70}$$

$$\frac{d}{dt}\hat{u}_i = -\frac{1}{\rho^*}\alpha\psi^6\partial_i P - \alpha\hat{u}^0\partial_i\alpha + \hat{u}_j\partial_i\beta^j + \frac{2\hat{u}_k\hat{u}_k}{\psi^5\hat{u}^0}\partial_i\psi, \tag{2.71}$$

$$\begin{aligned}\frac{d}{dt}\tau = & -\frac{\psi^6}{\rho^*}\left(\bar{v}^i+\beta^i\right)\left(1-\frac{hW}{\omega}\right)(\partial_i P) \\ & - \psi^6\frac{P}{\rho^*}\partial_i\left(\bar{v}^i+\beta^i\right) \\ & - 6\psi^5\frac{P}{\rho^*}\left(\bar{v}^i+\beta^i\right)(\partial_i\psi) \\ & - \frac{\hat{u}_i}{\psi^4}\left(1-\frac{hW}{\omega}\right)(\partial_i\alpha) \\ & + \frac{1}{\psi^4}\left(\frac{1}{hW}-\frac{1}{\omega}\right)\left[\hat{u}_i\hat{u}_j\partial_j\beta^i - \frac{1}{3}\hat{u}_i\hat{u}_i\partial_j\beta^j\right],\end{aligned} \tag{2.72}$$

where $\frac{d}{dt}$ denotes the total derivative $\frac{d}{dt} = \partial_t + \bar{v}^i\partial_i$, and $\omega = \sqrt{1+\psi^{-4}\delta_{ij}\hat{u}^i\hat{u}^j}$. Finally, to close the system of equations an EoS is required. The EoS provides a pressure relation of the form $P = P(\rho, \epsilon, Y_e)$. Throughout the evolution, Y_e is simply advected by solving the equation $\frac{dY_e}{dt} = 0$. We evolve these equations in time t using a fourth order RK4 scheme within the SPH formulation (see below). From the updated conserved $(\rho^*, \hat{u}_i, \tau)$ variables we numerically recover the primitive variables $(\rho, \bar{v}_i, \epsilon)$.

The discretization of the Eq. (2.70)-(2.72) is performed with the SPH formulation (see [91, 92]). The SPH particles are interpolation points which represent the fluid. Each SPH particle has a sphere of influence, quantified by the smoothing length h (see below). The value of a fluid field at a point in space is determined by summing over all contributions of the neighbouring particles. We remark that there is not a physical interpretation for the individual SPH particle, but they only become meaningful as a collection of particles. Because the conserved density ρ^* obeys the continuity equation Eq.(2.70), in the relativistic SPH framework, it is also given by

$$\rho^*_a = \sum_b m_b W(|\vec{r}_a - \vec{r}_b|, h_b), \tag{2.73}$$

where a denotes the particle a, m_b is the rest-mass of the particle b, and $W(|\vec{r}_a - \vec{r}_b|, h)$ is the spherical kernel function $W(r, h)$. The latter is an essential part of the SPH formulation since it quantifies the influence of particle b to particle a and vice versa. The quantity h_b is the smoothing length and represents the effective radius of influence of particle b. We also note that the (rest) mass of every SPH particle is constant throughout the evolution.

As previously mentioned, the SPH particles are interpolation points that represent the fluid, and as such, the values of an arbitrary field $A(\vec{r})$, at position $\vec{r}$, can be approximated by integrating the contributions of all SPH particles as

$$\langle A(\vec{r})\rangle = \int A(\vec{r'})\ W(|\vec{r} - \vec{r'}|, h) d\vec{r'}. \tag{2.74}$$

In this example A is a scalar field but it can also be a vector field. Assuming a collection of SPH particles, the above equation can be discretized as

$$\langle A(\vec{r})\rangle \approx \sum_a A(\vec{r_a})\,\frac{m_a}{\rho_a^*}\,W(|\vec{r}-\vec{r}_a|,h_a), \tag{2.75}$$

where $A(\vec{r_a})$ is the value of the field at the position of the particle a, h_a is the smoothing length of particle a, and the ratio $\frac{m_a}{\rho_a^*}$ is the effective volume of the particle a. Furthermore, the derivative of any field can be approximated in a similar fashion using the derivative of the analytic kernel functions. For instance, using Eq. (2.75), one can express the pressure gradient $\partial_i P_a$ of a particle a, as

$$\partial_i P_a = -\rho_a^* \sum_b m_b \left(\frac{P_b}{\rho_b^{*2}}+\frac{P_a}{\rho_a^{*2}}\right)\partial_i W(|\vec{r}_a-\vec{r}_b|,h_b). \tag{2.76}$$

As becomes apparent, the kernel function has to be chosen carefully. In our simulations, we use the Wendland kernel function (see [122, 123]). This kernel function leads to less numerical damping in the GWs emitted in the post-merger phase compared to other kernels used in earlier versions of the code (see [27, 28, 42, 124, 125]). This kernel also does not affect the corresponding frequencies in the GW spectrum compared again to other kernels. This may be because the Wendland kernel leads to SPH particle distributions which are more ordered and less noisy compared to other Kernels (see [123]). The Wendland kernel in three dimensions reads

$$W(q,h) = \frac{1365}{64\pi h^3}\max[(1-d),0]^8(32d^3+25d^2+8d+1), \tag{2.77}$$

where $d=|\vec{r}-\vec{r'}|/h$.

Furthermore, in the SPH framework shocks are treated with the inclusion of an artificial viscosity scheme. In this work, we employ the scheme introduced in [126] where every SPH particle is assigned to a time-dependent viscosity coefficient, which becomes large in the presence of shocks (that is when the velocity divergence becomes largely negative). Finally, the artificial viscous term is added to the physical pressure term (see [91] for a detailed description).

Finally, we note that for the NS merger simulations carried out with the SPH code, the ID are generated using the scheme described in [91, 92]. One difference between this scheme and the one used in the `LORENE` code is the prescription employed for determining the fluid velocity field. The two schemes are in good agreement with deviations in angular momentum and orbital angular velocity of the order of $\approx 1\%$ (see [91]). We briefly summarize the method: starting from an initial guess for the orbital angular velocity Ω of the system, the two stars are relaxed towards a velocity distribution of a binary with the prescribed Ω. In this phase, if the two stars begin to fall inwards then Ω is increased, and if their separation tends to increase, Ω is decreased.

3. Simulated models

In this chapter, we discuss the various simulations of binary NS mergers used in this work. We describe the fully general relativistic simulations of a sequence of models with increasing total binary mass $M_{\rm tot}$ using the Einstein Toolkit code. Then we introduce two separate data sets of simulations using the SPH code: a) we simulate mass sequences for several EoSs for symmetric binaries ($q = 1$); b) we consider three EoS models, representative of soft, medium, and stiff EoSs, to construct a grid of simulations for different mass ranges and binary mass ratios.

3.1. Sequence of binaries with the Einstein Toolkit

We perform fully general relativistic simulations of NS mergers using the Einstein Toolkit. We use the MPA1 [127] EoS model which is compatible with the current constraints from GW170817 [128], and the mass measurement of $2.01\pm0.04\ M_\odot$ for pulsar PSR J0348_0432 [78]. We consider a mass sequence of equal mass binaries (with mass ratio $q = 1$) with increasing total binary mass $M_{\rm tot}$. We simulate eight models with $M_{\rm tot} = 2.4,\ 2.5,\ 2.6,\ 2.7,\ 2.8,\ 2.9,\ 3.0$ and $3.1\ M_\odot$. We note that none of the simulated binaries forms a BH during the simulation time of up to 25 ms of post-merger phase, while our most massive model has a total mass which is close to the threshold mass $M_{\rm thres}$ for prompt BH formation [5].

We use the `LORENE` code [88, 89] to obtain circular quasi-equilibrium solutions for the initial data for our simulations (see Sec. 2.2). We choose an initial separation of 40 km between the centers of the NSs, which leads to a few revolutions prior to the merger. As previously mentioned, the quasi-circular ID are subject to residual eccentricity e (see Sec. 2.5), which we assess in Appendix A, and find that the GW features are hardly affected by values of $e < 0.01$. We evolve the ID using the Einstein Toolkit (see Sec. 2.3). As mentioned in Sec. 2.3, we employ the GRHydro module [98, 99] for the evolution of hydrodynamics which adopts the Valencia formulation [96, 97]. The HLLE Riemann solver [110] is used along with a weighted essentially non-oscillatory (WENO) reconstruction scheme [108, 109]. For the spacetime evolution we use the Z4c formulation described in Sec. 2.3.2 and the implementation of the CTGamma module [106, 107].

The computational domain has seven refinement levels and the innermost one corresponds to the finest resolution ($dx = 277$ m), while the grid spacing is doubled at each external level. We choose a box size with $x_{\rm max} = 2126.276$ km (and $x_{\rm min} = -2126.276$ km). In addition, we assess the resolution effects by considering a higher resolution model (see Appendix A) and find only weak influence on the

GW spectral features. The latter model is referred to as the HR simulation. We reduce the computational costs of our simulations by imposing reflection symmetry with respect to the orbital plane and pi symmetry to the axis normal to this plane. We find that the spectral properties are essentially unaffected in simulations without the pi symmetry (see Appendix A).

For the EoS we use a seven-segment piecewise polytrope [129] implementation which is supplemented with an ideal-gas pressure component to approximate the thermal effects. We set $\Gamma_{\rm th} = 1.75$ which is a reasonable choice for modeling post-merger GW emission [124].

The GWs are extracted using the Ψ_4 formalism. In the latter, we decompose the Weyl scalar Ψ_4 in spin-weighted spherical harmonics at a finite coordinate radius R, where we denote with $\Psi_4^{\rm l,m}(t, R)$ the radially averaged component. In our analysis we focus on the dominant model $(l, m) = (2, 2)$ and use an extraction coordinate radius of $R \simeq 443$ km. We tested that a larger extraction coordinate radius of $R \simeq 1033$ km leaves the GW spectra essentially unaffected. To derive the GW strain (from $\Psi_4^{\rm l,m}(t, R)$) a double integration with respect to coordinate time t is required, however, typical integration methods lead to non-linear drifts in the strain. This problem is avoided by performing the integration in the frequency domain using a fixed frequency integration scheme [130].

We define the merging time $t_{\rm merge}$ as the time at which $|h(t)| = \sqrt{h_+^2(t) + h_\times^2(t)}$ reaches the maximum. We perform a time shift ($t \to t - t_{\rm merge}$) so that $t = 0$ corresponds to the merging time. We split the GW signals into two phases accordingly: a) the inspiral phase ($t < 0$) b) the post-merger phase ($t \geq 0$). All figures associated with GW quantities (such as GW spectrograms) use the aforementioned convention meaning that $t = 0$ corresponds to the merging time obtained from $\max |h(t)|$. Figures and measures associated with the lapse function (such as spectrograms of the minimum lapse function $\alpha_{\rm min}$) define the merging time using the maximum of strain obtained from the quadrupole formula $|h^{\rm QF}(t)|$. We note that (prior to our time shifting) the two times of the $\max |h(t)|$ and $\max |h^{\rm QF}(t)|$ should differ by approximately $\Delta t \simeq \frac{1}{c} R \simeq 1.5$ ms, which thus can be removed as appropriate.

3.2. Large grid of SPH simulations

Furthermore, we generate two large libraries of binary NS merger simulations using the SPH code (see Sec. 2.6). We simulate in total 541 (350 + 191) binaries varying the total binary mass $M_{\rm tot}$, mass ratio q, and EoS model. For every simulation, we consider approximately 300000 particles (roughly 150000 particles per star), which is a typical resolution employed in such works (see also [5, 124, 131]). The spacetime is solved on a grid (see Sec. 2.6) with a grid spacing of approximately 1.18 km. We note that a typical simulation using the SPH code requires considerably less computational resources than the Einstein toolkit [1]. However, a

[1] A typical simulation with the SPH code requires approximately 3000 CPU hours which is significantly lower than in the case of a fully general relativistic simulation using the Einstein toolkit for setups like the ones described in Sec. 3.1.

straightforward comparison between these codes is not trivial since the hydrodynamics and spacetime evolution are treated differently. For these simulations, we use the Wendland kernel function (see Sec. 2.6) which, as previously mentioned, leads to less noise and numerical damping of the GW signals and also does not affect the frequencies of the GW spectrum compared to those obtained with other kernels.

In the first library of binaries, we simulate several mass sequences for different EoSs of symmetric binaries ($q = 1$) with increasing total mass $M_{\rm tot}$. We use this data set to investigate the dependence of the quasi-radial oscillation frequency f_0 in NS merger remnants on the EoSs and binary mass. Subsequently, we use this information to put constraints on $M_{\rm thres}$ and $M_{\rm max}$ (see Chapter 7).

In the second library of simulations, we employ three EoSs (stiff, soft, medium) and vary the total binary mass $M_{\rm tot}$ and mass ratio q. These simulations are employed in the development of a hierarchical Bayesian method for deriving constraints on the radius $R_{1.6}$ of a NS with gravitational mass of 1.6 $M_\odot$, through an ensemble analysis of binary NS mergers.

3.2.1. Symmetric binary sequences

We simulate eighteen mass sequences of symmetric binaries ($q = 1$) with varying EoSs. Of the total of eighteen EoS models, ten of them are microphysical EoSs with temperature dependence and eight are barotropic. We note that a barotropic EoS model is constructed at zero temperature assuming the beta-equilibrium condition. In this case, thermal effects are approximated with an ideal gas component with $\Gamma_{\rm th} = 1.75$ (see [124]). The microphysical temperature-dependent EoSs are: DD2 [132], SFHX [133], SFHO [133], TMA [134, 135], TM1 [134, 136], LS220 [137], LS375 [137], NL3 [132, 138], and GS2 [139], BHBLP [140]. The barotropic EoSs are: H4 [141], ALF2 [129,142], MPA1 [127], SLy4 [143], APR4 [144], WFF2 [145], BSK21 [146], BSK20 [146]. For the majority of the barotropic EoSs (except BSK20 and BSK21) we use the prescription introduced in [129] where the EoS tables are parametrized by a seven-segment piecewise polytrope. Figure 3.1 displays the gravitational mass $M_{\rm g}$ and radius R relation for non-rotating NSs for all the EoS models included in this data set. Table 3.1 provides the values of $M_{\rm max}$ and $M_{\rm thres}$ for the respective EoSs (see [5]).

We simulate in total 350 symmetric binaries. For every EoS sequence we consider a broad range of total binary masses, and for the majority of the models we do not simulate configurations very close to the threshold mass $M_{\rm thres}$ for prompt collapse to BH. This is because we are interested in remnants which survive for a few milliseconds ($\approx$ 15 to 20 ms) in the post-merger phase. The initial separation distance between the centers of the stars is approximately 38 km which results to a few revolutions of inspiral before the two stars merge. We note that this separation distance is slightly smaller than the one employed in the simulations performed with the Einstein Toolkit. This is because the generation of the ID and spacetime evolution is carried out under the CFC condition (see Sec. 2.6), and so, the unphysical transient typically observed at the beginning of simulations with fully general relativistic codes due to a relaxation of the ID, is not observed

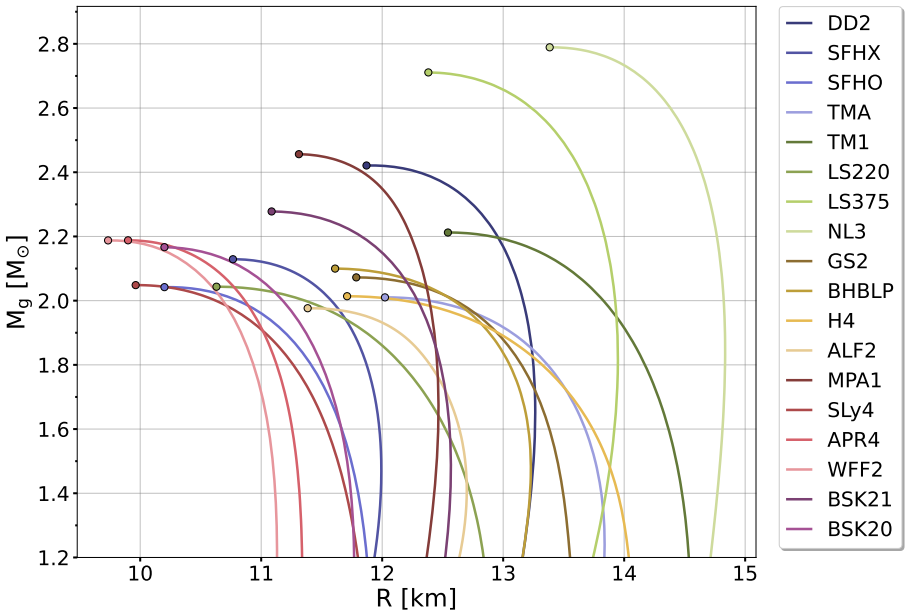

Figure 3.1: Gravitational mass and radius relation for non-rotating NSs for all the EoS models considered. Colored circles indicate the maximum mass configurations.

Temperature-dependent EoSs					
EoS	$M_{\rm max}$ $[M_\odot]$	$M_{\rm thres}$ $[M_\odot]$	EoS	$M_{\rm max}$ $[M_\odot]$	$M_{\rm thres}$ $[M_\odot]$
DD2	2.421	3.325	SFHX	2.129	2.975
SFHO	2.058	2.875	TMA	2.010	3.175
TM1	2.212	3.375	LS220	2.043	2.975
LS375	2.711	3.575	NL3	2.789	3.800
GS2	2.091	3.175	BHBLP	2.100	3.125

Barotropic EoS					
EoS	$M_{\rm max}$ $[M_\odot]$	$M_{\rm thres}$ $[M_\odot]$	EoS	$M_{\rm max}$ $[M_\odot]$	$M_{\rm thres}$ $[M_\odot]$
H4	2.012	3.125	ALF2	1.975	2.975
MPA1	2.456	3.225	SLy4	2.045	2.825
APR4	2.189	2.825	WFF2	2.188	2.825
BSK20	2.167	2.875	BSK21	2.278	3.075

Table 3.1: General information on the EoSs included in this library and the corresponding maximum mass of a non-rotating NS $M_{\rm max}$, and the threshold mass $M_{\rm thres}$ for prompt collapse to BH. Data taken from [5].

in these calculations (see [118]). An illustration of the parameter space in the EoS-$M_{\rm tot}$ plane is shown in Fig. 3.2.

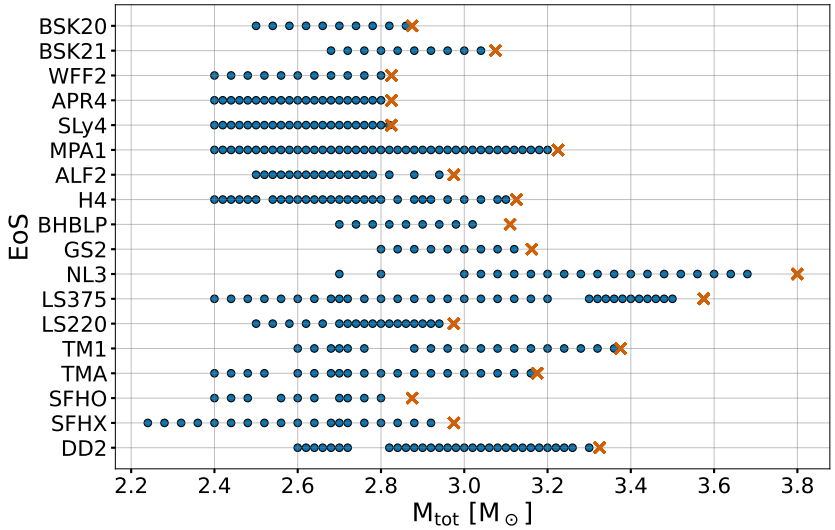

Figure 3.2: Illustration of the parameter space of the simulated binaries. Orange crosses indicate the threshold masses $M_{\rm thres}$ for the respective EoSs. $M_{\rm thres}$ values taken from [5].

3.2.2. Grids of binaries

We simulate 191 additional binary configurations to construct three grids of simulations with varying total binary masses $M_{\rm tot}$ and mass ratio q for three different EoS models. These are the DD2 [132], the SLy4 [143], and the SFHX [133], representative of stiffer, softer, and medium EoSs, respectively. We note that the softer EoSs lead to smaller NS radii and higher post-merger GW frequencies, assuming a fixed total binary mass $M_{\rm tot}$. As previously mentioned, the DD2 and SFHX models have a temperature dependence, while the SLy4 EoS is only available at zero temperature assuming the beta-equilibrium condition. Thermal effects are again described by the ideal gas approximation with $\Gamma_{\rm th} = 1.75$ (see [124] for details and a justification of this choice).

EoS	$M_{\rm thres}(q = 0.7)$ $[M_\odot]$	$M_{\rm thres}(q = 0.85)$ $[M_\odot]$	$M_{\rm thres}(q = 1.0)$ $[M_\odot]$
SFHX	2.925	2.975	2.975
DD2	3.275	3.325	3.325
SLy4	2.775	2.825	2.825

Table 3.2: Threshold masses for prompt collapse for different mass ratios q for the DD2, SFHX, SLy4 EoS models. Data taken from [5].

We vary the total binary mass $M_{\rm tot}$ in a broad range, but we do not consider systems that promptly form a black hole after merging (see Tab. 3.1). In all of the simulated configurations, the remnants survive for at least 15 ms in the post-merger phase. Generally, $M_{\rm thres}$ depends on the EoS model and exhibits an additional (mild) dependence on the mass ratio q (see [5]). Table 3.2 provides the values of $M_{\rm thres}$ for the respective EoSs included in this data set for mass

ratios $q \in \{0.7, 0.85, 1.0\}$ as computed in [5]. We consider six binary mass ratios $q \in \{0.7, 0.8, 0.85, 0.9, 0.95, 1.0\}$. For the SFHX binaries, we use a finer grid in $M_{\rm tot}$. In total, the library contains 41 binaries with DD2, 132 binaries with SFHX, and 41 binaries with SLy4.

Finally, we note that this data set is currently employed by external collaborators for the construction of a hierarchical Bayesian method for deriving constraints on $R_{1.6}$ through an ensemble analysis of barely-informative, marginal detections of the NS merger GW post-merger signal.

4. Spectral properties of GWs

In this chapter, we investigate the GW emission in the post-merger phase from NS mergers. We employ the data set with the fully general relativistic three-dimensional simulations described in Sec. 3.1. We discuss the post-merger spectral features for a sequence of equal-mass binaries ($q = 1$) of increasing total binary mass. We study the time evolution of the main frequency component $f_{\rm peak}$ and introduce an analytic function which models this evolution. We identify a mechanism which explains the origin of so far unexplained spectral features, that is, the non-linear coupling of the quasi-radial oscillation to the antipodal tidal deformation of the remnant. These features become significant for high-mass models.

4.1. Spectral analysis of post-merger GW emission

In this section, we discuss the different spectral features of the post-merger GW signal for the *reference simulation* of the model with total mass $M_{\rm tot} = 2.5\ M_\odot$. We study its GW spectrum and compute its spectrograms in order to extract the time evolution of certain features. Subsequently, we introduce a new coupling mechanism, which explains additional frequency peaks in the GW spectrum of high-mass configurations.

4.1.1. Evolution of $f_{\rm peak}$

The strongest feature in the post-merger GW signal, most commonly denoted by $f_{\rm peak}$ or f_2, is attributed to the fundamental quadrupolar oscillation mode (see [27, 31–47]). The frequency $f_{\rm peak}$ depends dominantly on the EoS and total binary mass, which is not unexpected since the size of the remnant is dictated by the high-density regime of the EoS. However, as the remnant is subject to further evolution, $f_{\rm peak}$ shifts to lower or higher frequencies. This is because the combined effects of angular momentum redistribution and losses from GW emission, change its stellar structure, thus leading to a change in the dominant oscillation frequency.

To understand the frequency evolution of the different components of the GW signal, we compute spectrograms which utilize a wavelet-based scheme [147]. Figure 4.1 shows the spectrogram of the strain $h_+(t)$ for the reference simulation ($M_{\rm tot} = 2.5\ M_\odot$). The time evolution of the dominant component $f_{\rm peak}$ is clear. In the first few milliseconds, a rapid evolution of $f_{\rm peak}$ takes place, and the signal is split in two phases: (a) for $t \lesssim 6$ ms, $f_{\rm peak}$ is decreasing approximately from

about 2.8 kHz to 2.5 kHz; (b) for $t \gtrsim 6$ ms, f_{peak} is approximately constant at $f_{\mathrm{peak}} = 2.5$ kHz.

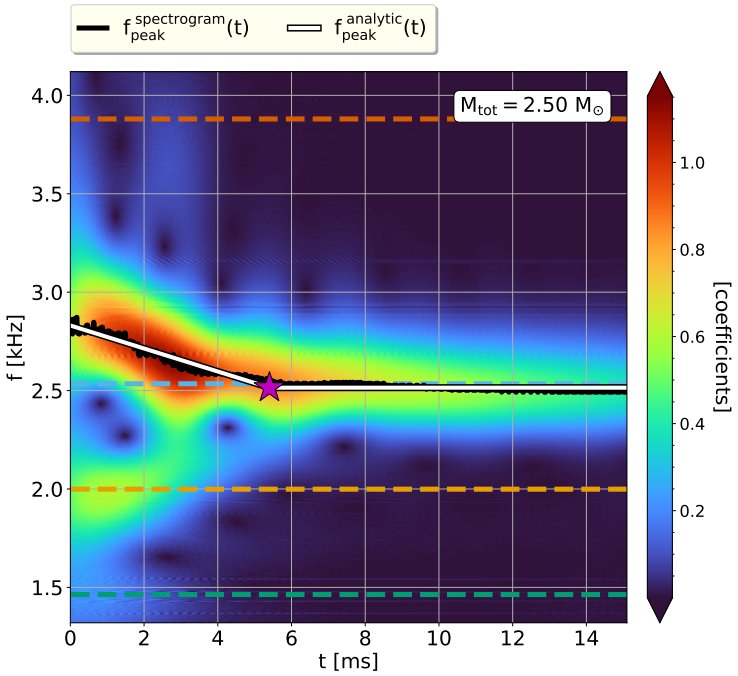

Figure 4.1: Spectrogram of strain $h_+(t)$ for the reference simulation. The black curve illustrates $f_{\mathrm{peak}}(t)$ determined by the maximum wavelet coefficient at given time t. The white curve shows the 2-segment piecewise analytic fit $f_{\mathrm{peak}}^{\mathrm{analytic(t)}}$ of Eq. (4.1). The purple star indicates $t = t_*$, after which the frequency remains constant. The cyan, yellow, green, and orange dashed horizontal lines indicate $f_{\mathrm{peak}}, f_{\mathrm{spiral}}, f_{2-0}, f_{2+0}$, respectively, as extracted from the spectrum shown in Fig. 4.2. Figure taken from [4].

We extract the evolution of $f_{\mathrm{peak}}(t)$ from the spectrogram (black curve) as the frequency of the maximum wavelet coefficient at time t, and thus quantify the frequency drift. We find that the time-dependent $f_{\mathrm{peak}}(t)$ can be modeled by a simple two-segment piecewise *analytic fit* with respect to the time coordinate t. The analytic function consists of: (a) a segment where the initial drift is described by a linear function in the frequency-time plane; (b) a segment which assumes a constant f_{peak} determined by the imposed continuity as

$$f_{\mathrm{peak}}^{\mathrm{analytic}}(t) = \begin{cases} \zeta_{\mathrm{drift}} \cdot t + f_{\mathrm{peak},0} & \text{for } t \leq t_* \\ f_{\mathrm{peak}}(t_*) & \text{for } t > t_* \end{cases} . \tag{4.1}$$

Figure 4.1 displays the analytic fit as two line segments (white) and is in good agreement with the numerically extracted $f_{\mathrm{peak}}(t)$. We note that Fig. 4.1 demonstrates a specific example where the initial drift is negative. In the general parameter space of different EoSs and total binary masses, the initial drift may be positive, negative, or nearly zero. There are also cases where a constant drift up to the delayed collapse to a BH describes more accurately the time evolution,

and these cases are still covered by the above analytic description. There are also cases where the frequency f_{peak} is not constant but continues to increase linearly, and these cases are still covered by the above analytic description.

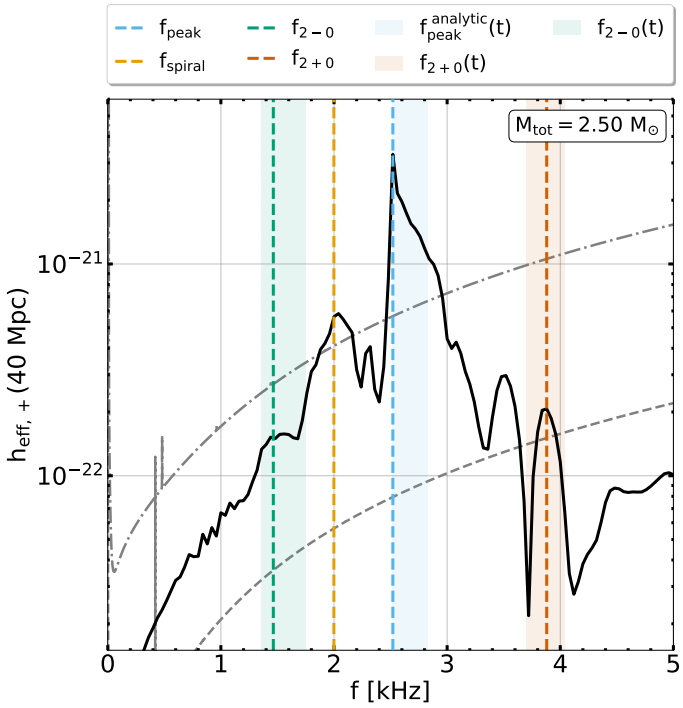

Figure 4.2: Effective GW spectrum $h_{\text{eff},+}(f)$ for the post-merger phase of the reference simulation. Colored dashed vertical lines indicate the frequency peaks $f_{\text{peak}}, f_{\text{spiral}}, f_{2-0}, f_{2+0}$. Shaded areas correspond to the frequency range of $f_{\text{peak}}, f_{2-0}, f_{2+0}$ (see text for details). The dash dotted curves denote the design sensitivity Advanced LIGO [2] and of the Einstein Telescope [3], respectively. Figure taken from [4].

For analyzing the GW spectrum, we employ the effective GW spectrum defined as $h_{\text{eff},+}(f) = f \cdot \tilde{h}_+(f)$, where $\tilde{h}_+(f)$ is the Fourier transform of the strain $h_+(t)$ (in agreement with the definition currently used in the literature). We note that in this work, f_{peak}, i.e. without explicit time argument, corresponds to the frequency associated with the maximum amplitude of $h_{\text{eff},+}(f)$, and $f_{\text{peak}}(t)$ refers to dominant frequency as a dynamical quantity, which is extracted from the spectrogram.

Figure 4.2 displays the effective GW spectrum $h_{\text{eff},+}(f)$ for the reference simulation, where we assume a distance of 40 Mpc and overplot the sensitivity curves of Advanced LIGO and the Einstein Telescope for reference. The dominant frequency peak corresponds to f_{peak}. As can be seen, the frequency peak f_{peak} may not be necessarily symmetric, however, it can have a broad, one-sided distribution toward higher frequencies. One explanation for this feature is an evolving time-dependent $f_{\text{peak}}(t)$, which covers the corresponding frequency range. We use the analytic piecewise function $f_{\text{peak}}^{\text{analytic}}(t)$ to obtain the frequency range of the evolution (cyan-shaded area) and find a good agreement with the one-sided peak

of the dominant mode as seen in Fig. 4.2.

Finally, from the spectrograms we also compute the mean value of $f_{\mathrm{peak}}(t)$ averaged over the duration of the drift, namely, the interval from 0 to t_*. We find that the mean value $\langle f_{\mathrm{peak}}^{t\in[0,t*]}(t)\rangle$ provides a measure for $f_{\mathrm{peak}}(t)$ at early times, but it does not necessarily coincide with the maximum in the GW spectrum.

4.1.2. Secondary GW peaks $f_{2\pm0}$ and f_{spiral}

As depicted in the spectrogram (see Fig. 4.1) and the GW spectrum (see Fig. 4.2), the GW signal in the post-merger phase not only contains the dominant oscillation mode but also many secondary features. More precisely, a non-linear coupling between the quadrupolar mode and the quasi-radial oscillation mode f_0 explains two of those subdominant spectral features. This coupling is expected to produce side peaks (combination tones) of the dominant peak at frequencies $f_{2\pm0} \approx f_{\mathrm{peak}} \pm f_0$. We identify these secondary peaks in the GW spectrum in Fig. 4.2 at approximately $f_{\mathrm{peak}} \pm f_0$. The quasi-radial frequency f_0 is estimated from the Fourier transform of the evolution of the minimum lapse function α_{min}, since f_0 (being a quasi-radial oscillation) does not contribute prominently to the GW spectrum.

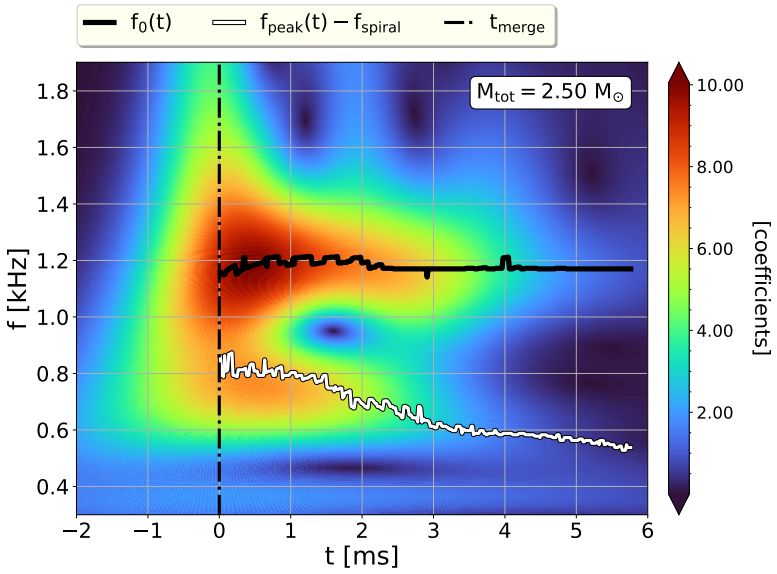

Figure 4.3: Spectrogram of minimum lapse function $\alpha_{\mathrm{min}}(t)$ for the reference simulation. The black curve shows $f_0(t)$, as determined by the maximum wavelet coefficient at time t. The white line shows $f_{\mathrm{peak}}(t) - f_{\mathrm{spiral}}$. The vertical dash-dotted line indicates the merging time t_{merge}. Figure taken from [4].

In this analysis, we define and extract the $f_{2\pm0}$ as the local maxima in the effective GW spectrum $h_{\mathrm{eff},+}(f)$ using the full signal including the inspiral phase. We note that the relation $f_{2\pm0} = f_{\mathrm{peak}} \pm f_0$ is only approximate. This inequality is due to the fact that the frequencies $f_{2\pm0}$ are determined during the early and very dynamical evolution of the remnant. In the early post-merger phase, the radial oscillation is strongly excited and the main frequency peaks, in particular $f_{\mathrm{peak}}(t)$, can evolve rapidly.

For this reason, we investigate the time evolution of the quasi-radial mode $f_0(t)$. From the spectrogram of the time evolution of the minimum lapse function $\alpha_{\rm min}(t)$ (see Fig. 4.3) we extract the time-dependent $f_0(t)$. We employ a second order polynomial fit to detrend the data to improve the quality of the spectrogram. We note that $f_0(t)$ can also be extracted from the time evolution of the maximum rest-mass density $\rho_{\rm max}(t)$. The frequency change of $f_0(t)$ for the reference simulation is small and comparable to the noise associated to the spectrogram scheme. We note that for high-mass models the frequency drift of $f_0(t)$ is slightly more pronounced (see Appendix B). As expected, the roughly constant $f_0(t)$ is in good agreement with the dominant peak in the power spectrum of $\alpha_{\rm min}$ (see Fig. 4.11).

Finally, we use the time evolution of both $f_{\rm peak}(t)$ and $f_0(t)$ to obtain the time-dependent $f_{2\pm0}(t) = f_{\rm peak}(t) \pm f_0(t)$. We derive the frequency ranges in which $f_{2\pm0}(t)$ varies, as indicated by the green and orange bands in Fig. 4.2, and find that they coincide well with the secondary peaks.

As already mentioned, we find that the exact values of $f_{2\pm0}$ deviate by some percent from $f_{\rm peak} \pm f_0$ i.e. the frequencies extracted from the full signal, which is a consequence of the initial evolution of the main peak frequency $f_{\rm peak}(t)$. We find that employing the average $\langle f_{\rm peak}^{t\in[0,t*]}(t)\rangle$, which is more representative for the initial phase, an excellent agreement between $f_{2\pm0}$ and $\langle f_{\rm peak}^{t\in[0,t*]}(t)\rangle \pm f_0$ is obtained. The latter is understandable since f_0 decays relatively fast in comparison to $f_{\rm peak}$, and thus one may expect that the coupling between both modes is determined by $f_{\rm peak}(t)$ at the early stage.

Moreover, we identify another secondary peak, $f_{\rm spiral}$, originating from the orbital motion of tidal antipodal bulges formed during the merging phase (see [28]). Figure 4.4 displays the rest-mass density in the orbital plane at different times in the early post-merger phase where the formation of the antipodal tidal bulges can be seen. Their angular frequency is lower than the inner remnant, and therefore the $f_{\rm spiral}$ has systematically lower frequency than $f_{\rm peak}$. We note that the $f_{\rm spiral}$ component is present only for a few cycles. Our results show that the antipodal bulges also appear in fully general relativistic simulations. In our analysis, we treat $f_{\rm spiral}$ as a constant in time quantity and we define it as the maximum of the corresponding peak at the GW spectrum. In reality, $f_{\rm spiral}$ may be subject to a slight frequency evolution since the central remnant evolves in time and therefore affects the motion of the bulges which generate $f_{\rm spiral}$. As shown in Fig. 4.1, at approximately $t = 3$ ms and $f = 2.20$ kHz, the frequency of $f_{\rm spiral}$ increases. We note that this frequency drift can also be seen in spectrograms with wavelet parameters which enhance the frequency resolution. However, the amplitude of the $f_{\rm spiral}$ feature drops rapidly and thus the impact of such frequency evolution is expected to be small. The most dominant secondary frequency peak in our reference simulation is $f_{\rm spiral}$, and therefore we expect the presence of an additional low-frequency modulation at $f_{\rm peak}(t) - f_{\rm spiral}$. The latter affects the remnant's compactness and therefore the evolution of $\alpha_{\rm min}(t)$ (see [28]). Indeed, this modulation can be seen in the spectrogram of $\alpha_{\rm min}(t)$ in our reference simulation in Fig. 4.3, where the extracted $f_{\rm peak}(t) - f_{\rm spiral}$ is overplotted (white).

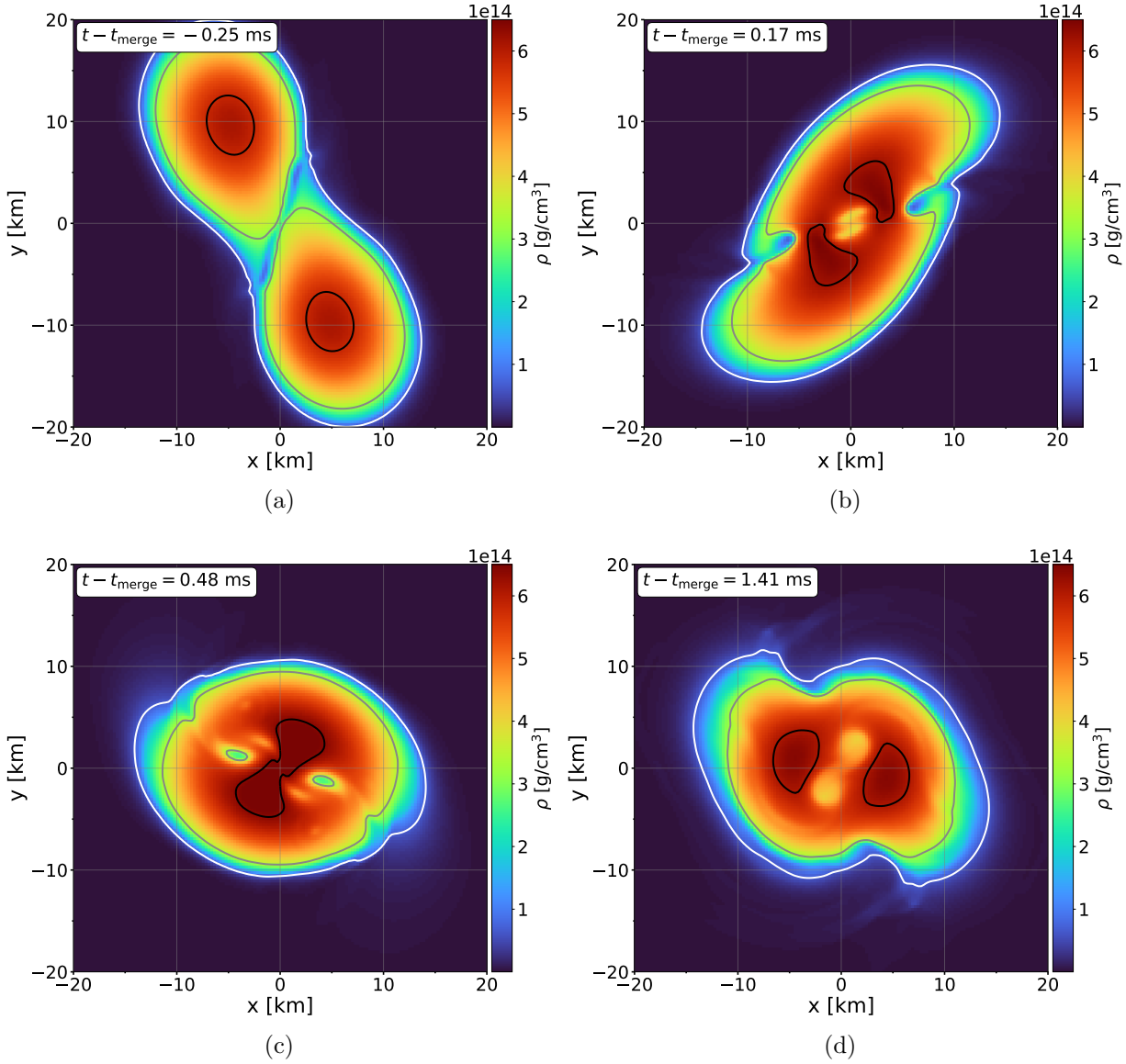

Figure 4.4: Rest-mass density profiles in the orbital plane at different times in the early post-merger phase. Contour lines with white, gray, and black colors indicate the regions with rest-mass density equal to $0.1\rho_{\rm max}(t)$, $0.5\rho_{\rm max}(t)$, and $0.95\rho_{\rm max}(t)$, respectively.

4.1.3. $f_{\rm spiral-0}$ coupling

We discuss our findings regarding a new mechanism, which explains additional spectral features in the GW spectrum. More specifically, we discuss a coupling between $f_{\rm spiral}$ and the quasi-radial oscillation mode f_0. We find that the aforementioned feature is more pronounced in high-mass configurations, and thus we discuss the simulation with a total binary mass $M_{\rm tot} = 3.0\ M_\odot$ (see Fig. 4.5). Because its total binary mass $M_{\rm tot}$ is close to $M_{\rm thres}$, the quasi-radial mode is strongly excited [28]. In this configuration $f_{\rm spiral}$ is clearly pronounced (see Fig. 4.5). Our conjecture is that the strong radial oscillation affects the orbital motion of the

bulges, and this leads to a coupling between f_0 and $f_{\rm spiral}$. Indeed, we find frequency peaks at approximately $f_{\rm spiral\pm0} = f_{\rm spiral} \pm f_0$.

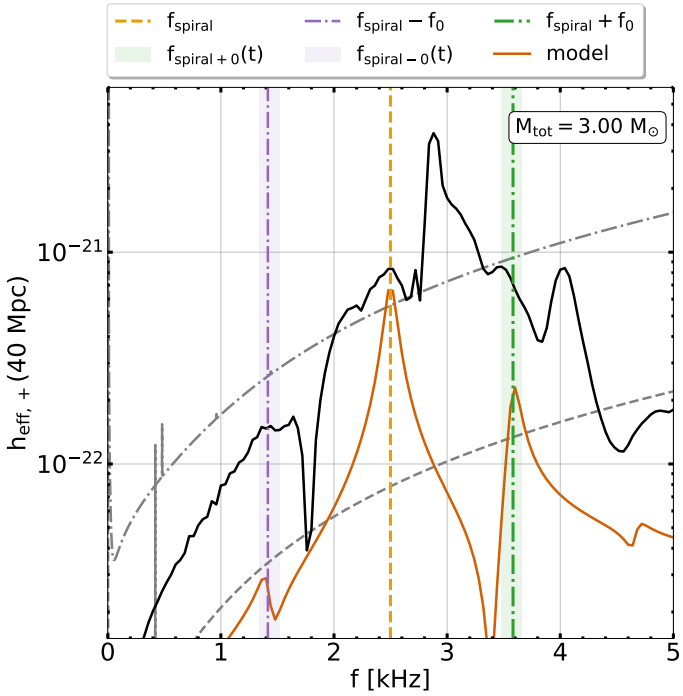

Figure 4.5: Effective GW spectrum $h_{\rm eff,+}(f)$ for the $M_{\rm tot} = 3.0 M_\odot$ model at post-merger phase. Colored vertical lines indicate $f_{\rm spiral}$, $f_{\rm spiral-0}$, $f_{\rm spiral+0}$. Shaded areas correspond to their frequency range visualized by the same colors respectively. Orange curve shows the effective GW spectrum of a simple toy model discussed in Sec. 4.1.3. Figure taken from [4].

Figure 4.5 displays the GW spectrum of the post-merger phase for this simulation. Similarly to the previous case, the quasi-radial oscillation frequency f_0 is extracted from the maximum in the Fourier transform $\tilde{\alpha}_{\rm min}(f)$ of the minimum lapse function (see Fig. 4.11). We estimate $f_{\rm spiral\pm0}$ using the $f_{\rm spiral}$ from the GW spectrum, and as shown in Fig. 4.5, we find that the estimates $f_{\rm spiral\pm0}$ match very well with additional frequency peaks in the power spectrum. The low-frequency $f_{\rm spiral} - f_0$ is in good agreement with the corresponding frequency peak and in contrast, the high-frequency $f_{\rm spiral} + f_0$ exhibits a deviation by approximately 200 Hz. In order to assess our conjecture, we use the time-dependent $f_0(t)$, extracted from the spectrogram of $\alpha_{\rm min}(t)$ (see Fig. 4.3), and estimate the frequency ranges of $f_{\rm spiral\pm0}$. We find these ranges to be in good agreement with additional peaks in the GW spectrum, and in particular, the frequency peak in the vicinity of $f_{\rm spiral} + f_0$ indeed lies in the corresponding frequency range. We note that a 200 Hz deviation may be understandable because, in reality, the $f_{\rm spiral}$ component is not exactly constant. We emphasize that our finding is not restricted to this particular EoS model but is a general feature in NS merger simulations. We carried out additional simulations using the SPH code employing different EoS models with varying total binary masses, and observe it in the corresponding GW spectra (see below).

To further corroborate our finding, we consider a simple toy model: We use two point particles with individual masses $m_1 = m_2 = 0.2\ M_\odot$ on a circular orbit with orbital frequency $f_{\rm orb} = \frac{1}{2} f_{\rm spiral}$ at a radius $R = 9$ km. In addition, a radial oscillation with frequency f_0 is superimposed on the circular orbit with amplitude $A = 1$ km. We believe these values are representative numbers, guided by a rough analysis of the simulation data. Since the bulges disappear after a few milliseconds, we mimic this behavior using an exponential decay of the point-particle masses with a timescale $\tau_m = 5.0$ ms. Finally, we obtain the corresponding GW radiation using the quadrupole formula and derive the Fourier transform, which is overplotted in Fig. 4.5. This simple model produces a dominant peak at $f_{\rm spiral}$ (as is expected) and two secondary peaks coinciding with $f_{\rm spiral} \pm f_0$. The same pattern of relative amplitudes of $f_{\rm spiral} \pm f_0$ in the simulation and the toy model is apparent; $f_{\rm spiral} + f_0$ is significantly enhanced.

The coupling to the quasi-radial mode f_0 may also result in frequency peaks at approximately $f_{\rm peak}(t) \pm 2 \cdot f_0$ and $f_{\rm spiral} \pm 2 \cdot f_0$, but these are expected to be weak components. A exception may be the high total mass models, where the f_0 mode is strongly excited and thus they may become significant. We note that our simple toy model generates a peak (in its spectrum) at roughly $f = 4.7$ kHz which coincides with $f_{\rm spiral} + 2 \cdot f_0$. In addition, a weak bump in the GW spectrum can be seen in the vicinity of $f_{\rm spiral} + 2 \cdot f_0$. In Chapter 6 we identify more features in the GW spectrum which can be associated to such couplings.

In the following subsubsection, we briefly discuss results using another simulation tool, the SPH code, for different physical binary systems. With this, we provide additional evidence on the spiral $\pm$ 0 coupling and its presence in GW spectra for additional EoS models.

SPH simulations with different EoSs

To show the generality of our results we identify the aforementioned spectral features ($f_{\rm spiral\pm0}$) in six additional simulations using the SPH code (see Sec. 2.6). We use a subset of the data set described in Sec. 3.2.1. We consider three EoS models, namely, SFHX [133], DD2 [132], and LS375 [137] and analyse the GW spectra for two configurations for every EoS model with total binary masses denoted by $M_{\rm tot,1}$ and $M_{\rm tot,2}$, respectively. The total binary masses are chosen to be relatively high (not far from the respective $M_{\rm thres}$ value for each EoS). This choice ensures that the quasi-radial modes are strongly excited and so the coupling spiral $\pm$ 0 may be pronounced too. Table 4.1 provides information about the total binary masses $M_{\rm tot,1}$, $M_{\rm tot,2}$ for all the configurations considered along with the corresponding value of $M_{\rm thres}$ for equal-mass configurations. We note that $M_{\rm thres}$ exhibits a mild dependence on the mass ratio q (see [5] for an elaborate discussion).

Figures 4.6-4.8 display the effective GW spectra in the post-merger phase for the simulated models. We extract the frequency of the quasi-radial oscillation f_0 from the Fourier transform of the time evolution of the minimum lapse function $\alpha_{\rm min}(t)$ (also described in Sec. 4.2.2). In order to identify the frequency $f_{\rm spiral}$ for every model, we first obtain a rough estimate of its frequency range using the empirical relations introduced in [49]. Then we pick the frequency at the maximum

in the GW spectrum within the estimated frequency ranges (orange dashed line in Fig. 4.6-4.8). Finally, we use the expression $f_{\text{spiral}\pm 0} \approx f_{\text{spiral}} \pm f_0$ to derive the frequency estimates for the combination tones $f_{\text{spiral}\pm 0}$.

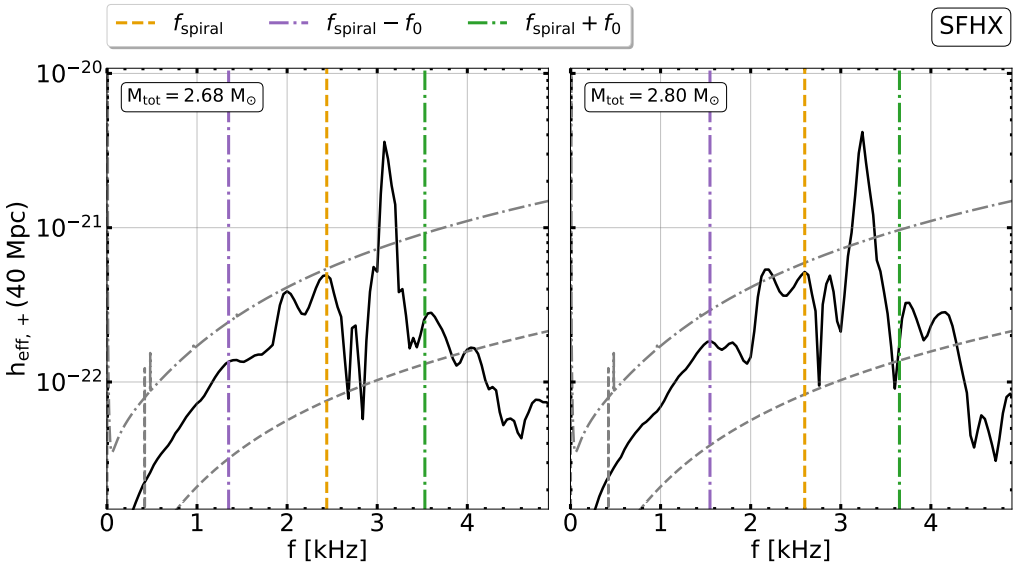

Figure 4.6: Effective GW spectra in the post-merger phase for the $M_{\text{tot},1}$ (left panel) and $M_{\text{tot},2}$ (right panel) models for the SFHX EoS. Colored vertical lines indicate f_{spiral}, $f_{\text{spiral}} - f_0$, $f_{\text{spiral}} + f_0$. The dash dotted curves denote the design sensitivity Advanced LIGO [2] and of the Einstein Telescope [3], respectively.

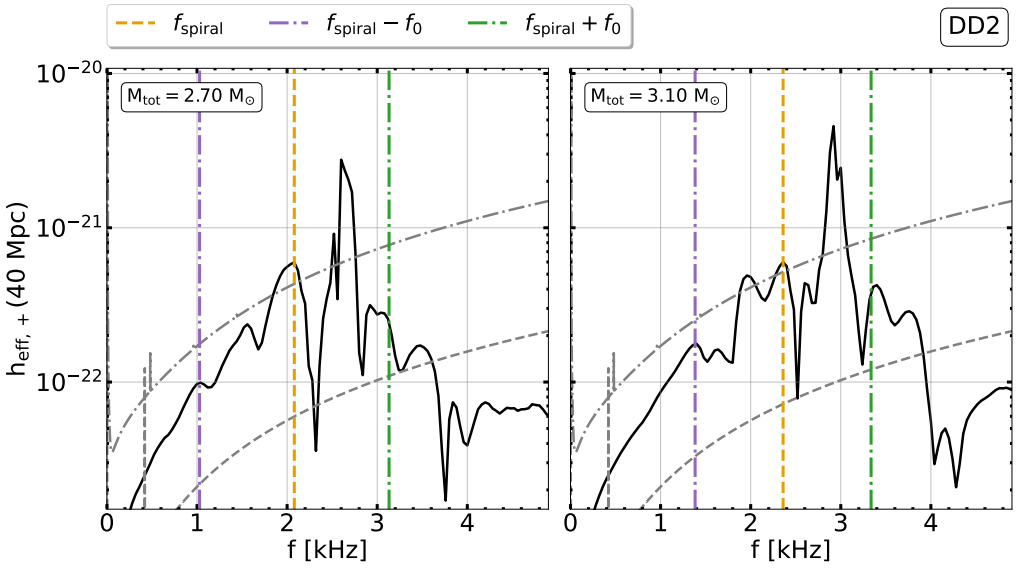

Figure 4.7: As in Fig. 4.6 but for the DD2 EoS.

As is apparent in Fig. 4.6-4.8, the combinations $f_{\text{spiral}} \pm f_0$ almost exactly match with frequency peaks in the GW spectra for all the models in our subset of simulations. This shows that the coupling spiral $\pm$ 0 is indeed a general spectral

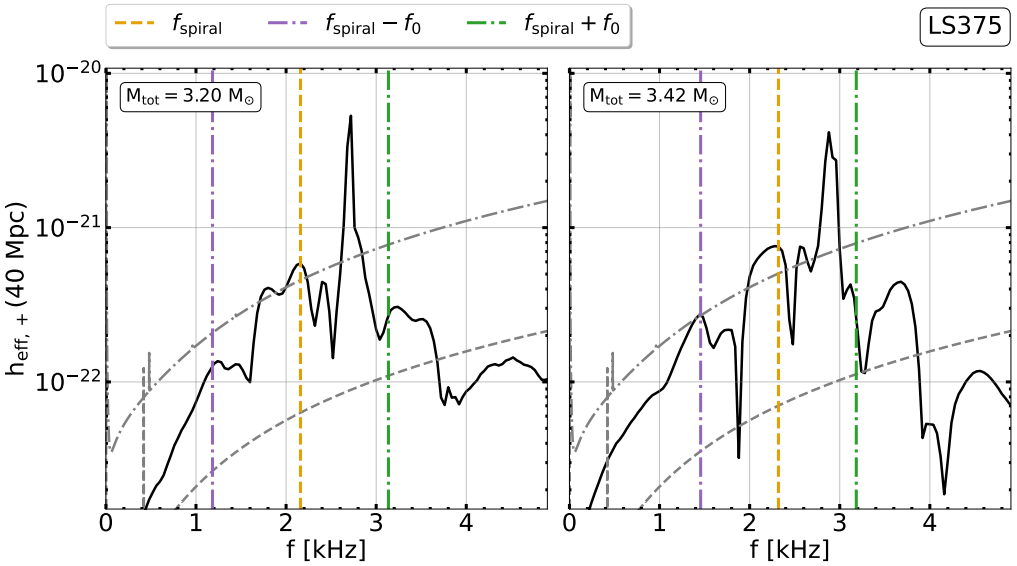

Figure 4.8: As in Fig. 4.6 but for the LS375 EoS.

feature in the GW spectra, which appears for various EoS models and mass ranges. We note that we have identified $f_{\mathrm{spiral}-0}$ for additional models in our data set of symmetric binary simulations and constructed empirical relations for $f_{\mathrm{spiral}-0}$ as a function of M_{chirp} and $R_{1.6}$ following the parametrization introduced [49] for the frequencies $f_{\mathrm{spiral}}, f_{2\pm0}$ (see Appendix C).

EoS	$M_{\mathrm{tot},1}$ $[M_\odot]$	$M_{\mathrm{tot},2}$ $[M_\odot]$	$M_{\mathrm{thres}}(q=1)$ $[M_\odot]$
SFHX	2.68	2.80	2.975
DD2	2.70	3.10	3.325
LS375	3.20	3.42	3.575

Table 4.1: Information about the subset of simulations. The values of M_{thres} are taken from [5].

4.2. Sequence of merger simulations with different total binary mass

In this section, we focus once again on the results obtained with the Einstein Toolkit. More specifically, we discuss the sequence of merger simulations with different total binary masses (see Sec. 3.1).

We focus on the dependence of the various components of the post-merger GW signal on total binary mass. As previously mentioned, the total mass M_{tot} ranges from 2.4 $M_\odot$ to 3.1 $M_\odot$ with a step size of 0.1 $M_\odot$ (including the reference simulation). We find a smooth transition in the GW spectra along the sequence, and find that the strength and presence of the various spectral components continuously change as the total binary mass M_{tot} approaches the mass for prompt

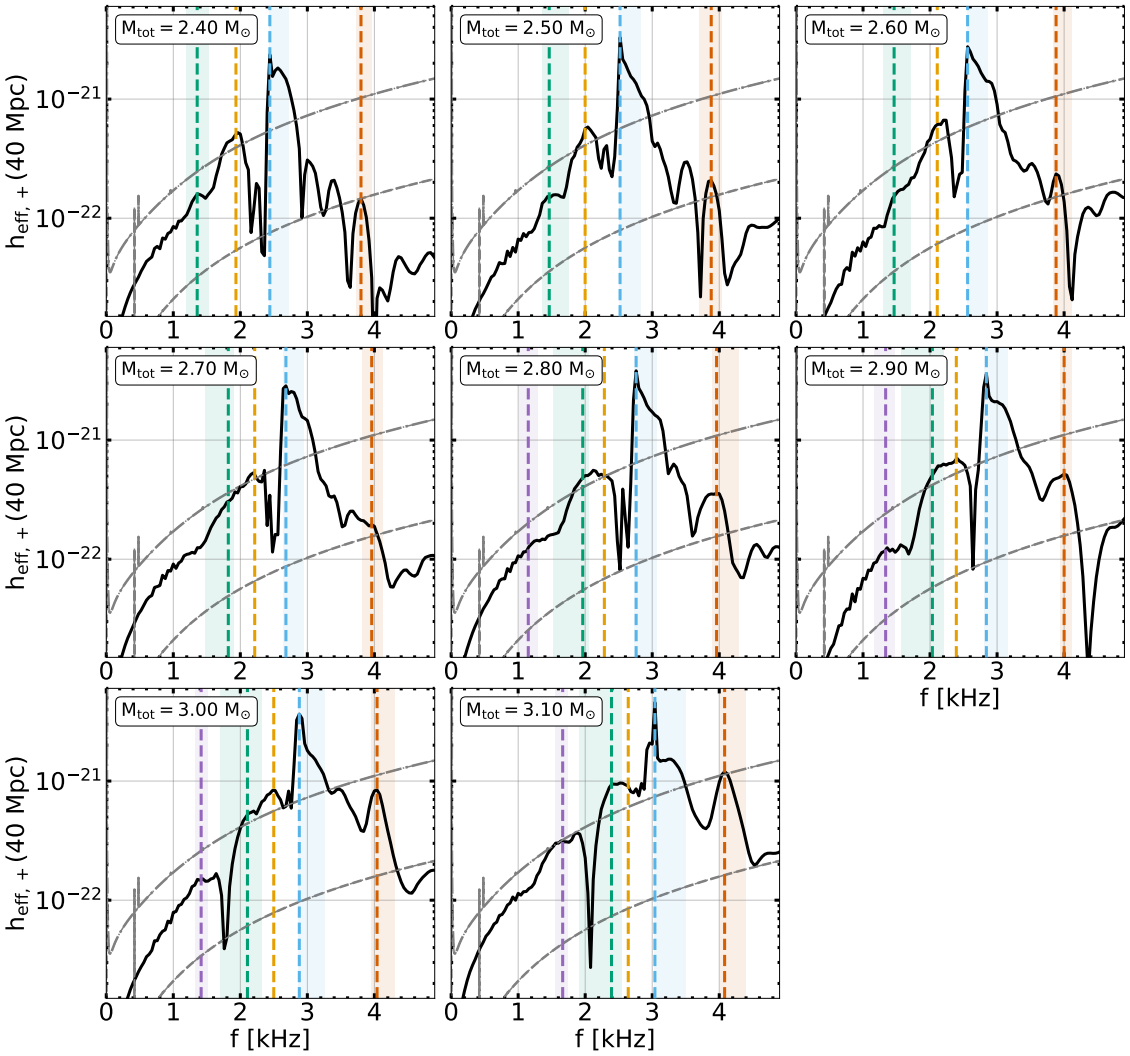

Figure 4.9: Effective GW spectra $h_{\mathrm{eff},+}(f)$ for the mass sequence. Purple dashed lines indicate $f_{\mathrm{spiral}-0}$. Purple shaded areas correspond to frequency ranges. The other colors follow the notation of Fig. 4.2. Figure adapted from [4].

BH formation M_{thres}. Figure 4.9 displays the effective GW spectra $h_{\mathrm{eff},+}(f)$ for different total binary masses M_{tot}, where the frequencies f_{peak}, f_{spiral}, $f_{2\pm0}$ and $f_{\mathrm{spiral}\pm0}$ are indicated.

4.2.1. Secondary GW peaks

We observe a clear dependence of the main and secondary peaks on the total binary mass as shown in Fig .4.9. The morphology of the GW spectra is broadly in agreement with the classification of the post-merger GW signals introduced in [28]. The latter is based on the presence and relative strength of the secondary peaks. For *low-mass* configurations ($M_{\mathrm{tot}} \leq 2.6\ M_{\odot}$) the frequencies f_{2-0} and f_{spiral} are well separated, while f_{2-0} is relatively weak because the quasi-radial oscillation is not strongly excited. In *high-mass* configurations ($M_{\mathrm{tot}} \geq 2.8\ M_{\odot}$), f_{2-0} becomes

more pronounced, and we observe a noticeable overlap between f_{2-0} and $f_{\rm spiral}$. We note that the absolute height of the $f_{\rm spiral}$ peak is approximately constant in all models. In contrast, the f_{2-0} peak becomes stronger as $M_{\rm tot}$ increases, by nearly one order of magnitude in $h_{\rm eff,+}(f)$.

In most of the models, the secondary frequency peak f_{2+0} is observationally less interesting due to its lower amplitude, when compared to the other secondary peaks, and because of the lower sensitivity of current detectors at higher frequencies. Nevertheless, the two models with the highest mass within our sequence of simulations exhibit an f_{2+0} with an amplitude comparable to the other secondary peaks, and thus becomes observationally relevant. Interestingly, the frequency f_{2+0} shows only a mild dependence on $M_{\rm tot}$ and ranges between 3.8 kHz and 4.0 kHz for the while mass sequence. The latter can be explained by the fact that $f_{\rm peak}$ is an increasing function of $M_{\rm tot}$ while f_0 decreases (see Chapter 7).

The high-mass configurations (and in particular the ones with total binary mass $M_{\rm tot} \geq 2.9\ M_\odot$) exhibit a significant frequency $f_{\rm spiral-0}$ peak as shown (purple dashed line) in Fig. 4.9. Because $f_{\rm spiral}$ grows with $M_{\rm tot}$ while f_0 decreases, the frequency $f_{\rm spiral-0}$ increases as the total binary mass approaches the threshold mass for prompt BH formation $M_{\rm thres}$. The strength of the $f_{\rm spiral-0}$ peak increases with the total binary mass $M_{\rm tot}$, and its absolute amplitude is always lower than that of aforementioned secondary features. However, relative to the projected detector sensitivity curves the signal-to-noise ratio of $f_{\rm spiral-0}$ coupling is roughly comparable to that of f_{2+0}. The $f_{\rm spiral-0}$ feature is thus important for configurations with binary masses close to $M_{\rm thres}$, where the quasi-radial mode is strongly excited, which enhances both $f_{\rm spiral-0}$ and $f_{2\pm0}$ (see lower right panel in Fig. 4.9).

4.2.2. Minimum of the lapse function

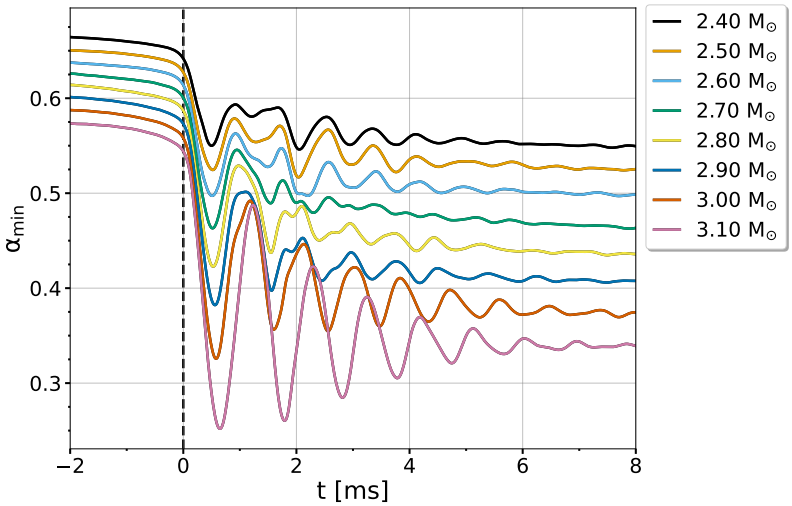

Figure 4.10: Time evolution for minimum lapse function $\alpha_{\rm min}(t)$ normalized to merging time $t_{\rm merge}$ along the sequence of models with varying $M_{\rm tot}$. Black vertical dashed line shows the merging time $t_{\rm merge}$. Figure taken from [4].

Furthermore, we investigate the time evolution of the minimum lapse function $\alpha_{\rm min}$ (as in [28]). As illustrated in Fig. 4.10 the behavior of $\alpha_{\rm min}(t)$ for all the models along the sequence is consistent with the respective GW spectra and shows a clear dependence on total binary mass $M_{\rm tot}$. The quasi-radial mode is stronger excited as the total mass increases, as already noted for the models discussed in [28]. The latter explains the enhancement of those GW features, which involve a coupling to this oscillation mode. The lower-mass and intermediate-mass models exhibit only a weakly excited quasi-radial mode. In those models, $\alpha_{\rm min}(t)$ contains an additional oscillation with lower frequency $f_{\rm peak}(t) - f_{\rm spiral}$, which is the dominant component at the early phase of the remnant evolution. The massive orbiting bulges generating $f_{\rm spiral}$ affect the remnant's compactness and thus lead to this low-frequency modulation (see [28] for details).

The trends present in Fig. 4.10 can be understood from the merger dynamics and the remnant properties. The high-mass models are associated to collisions with higher impact velocities (since they are more compact) and as a result the quasi-radial oscillation is strongly excited.

We perform the Fourier transform of the minimum lapse function, $\tilde{\alpha}_{\rm min}(f)$, and identify the aforementioned features, as shown in Fig. 4.11 (see also [148]). We note that we compute $\tilde{\alpha}_{\rm min}(f)$ using an appropriate window function to select the relevant post-merger phase and subtract the trend from the time series.

All of our models have a common feature, that is the pronounced quasi-radial oscillation frequency f_0 in the vicinity of 1 kHz. In low-mass configurations, we identify the low-frequency $f_{\rm peak}(t) - f_{\rm spiral}$ modulation (the additional peak at lower frequencies) with a strength comparable to that of the quasi-radial mode. There are cases where the $f_{\rm peak}(t) - f_{\rm spiral}$ modulation appears to be dominant in the initial phase in the time domain (see Fig. 4.10), however since the quasi-radial mode oscillates longer the f_0 peak in the post-merger spectrum is stronger.

The high-mass models exhibit a very dominant frequency peak f_0. The strength of the peak increases with total binary mass $M_{\rm tot}$, and it becomes broader and one-sided. The latter implies that the quasi-radial frequency undergoes an evolution, which can be verified by spectrograms of $\alpha_{\rm min}$ (see Appendix B). For intermediate-mass models the $f_{\rm peak}(t) - f_{\rm spiral}$ peak overlaps and merges with the f_0 peak, as $M_{\rm tot}$ increases. We remark that especially for high-mass models $f_{\rm peak}(t)$ initially evolves rapidly toward lower values, while being initially higher that the $f_{\rm peak}$ identified in the GW spectrum (see Appendix B). As a result, the difference $f_{\rm peak}(t) - f_{\rm spiral}$ at the early times, when the low-frequency modulation is present, is in fact larger than one would infer from the GW spectrum alone. In fact, in high-mass models the difference is roughly consistent with the left side of the main peaks in Fig. 4.11. Figure 4.11 displays the estimates for the frequency ranges for $f_{\rm peak}(t) - f_{\rm spiral}$ (red band).

4.2.3. Evolution of frequencies

As in the case of the reference simulation (see Sec. 4.1), the time evolution of $f_{\rm peak}(t)$ leads to an asymmetric (one-sided) peak for all the post-merger GW spectra along the sequence of models (see Fig. 4.9). The exact morphology of this peak

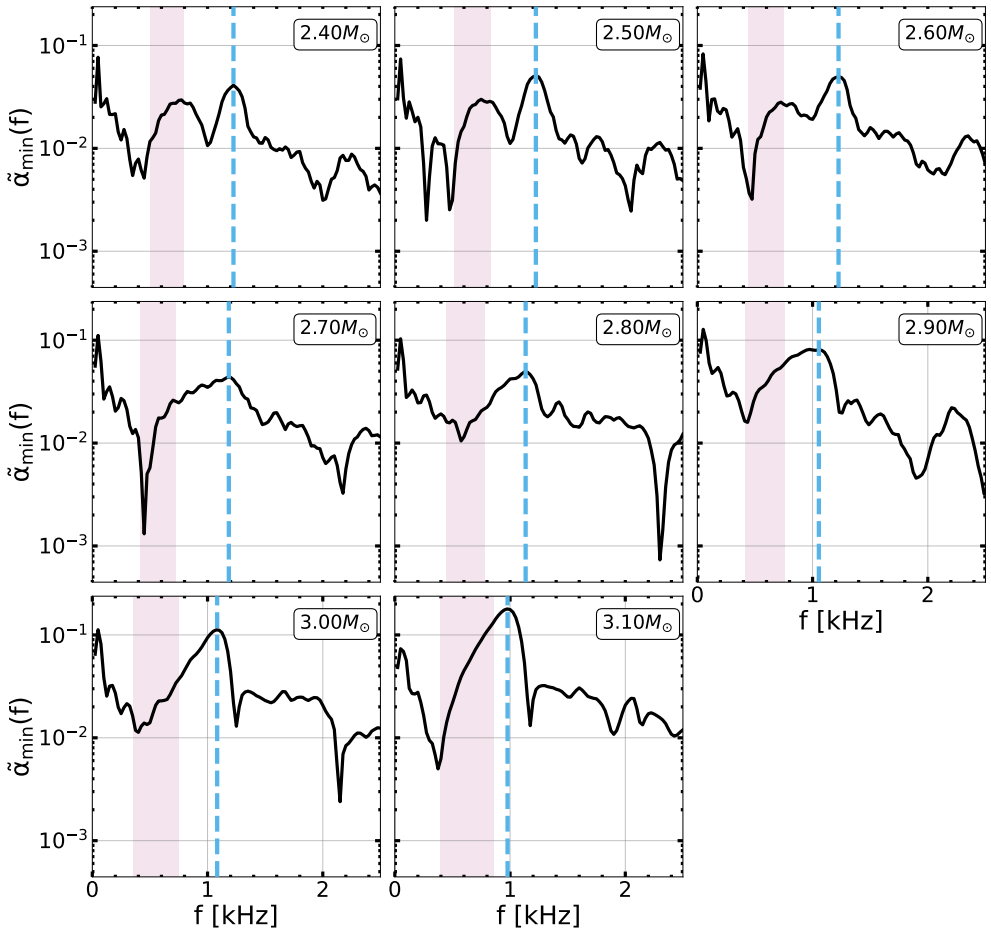

Figure 4.11: Fourier transform of the minimum lapse function along the sequence models with varying $M_{\rm tot}$. The vertical dashed line indicates the quasi-radial frequency f_0. The red band indicates the frequency range of $f_{\rm peak}(t) - f_{\rm spiral}$. Figure adapted from [4].

slightly varies as $M_{\rm tot}$ increases. To quantify the respective frequency drifts in $f_{\rm peak}(t)$ we employ the two-segment piecewise linear/constant function $f_{\rm peak}^{\rm analytic}(t)$ and perform a fit, as shown for the reference simulation in Sec. 4.1 (see Appendix B for the spectrograms used for the extraction of the time evolution of the $f_{\rm peak}(t)$ and Sec. 5.3 for empirical fits for the parameters of $f_{\rm peak}^{\rm analytic}(t)$ for the sequence of models). The analytic fit $f_{\rm peak}^{\rm analytic}(t)$ provides a frequency range for each model along the sequence, which we indicate by cyan bands in Fig. 4.9. These bands coincide well with the full structure of the main peak in the different spectra.

Similarly, we estimate the frequency ranges of the secondary peaks from the coupling between the quadrupolar and the quasi-radial mode. The frequency $f_0(t)$ is extracted from the spectrogram of the minimum lapse function $\alpha_{\rm min}(t)$, and using the analytic fit $f_{\rm peak}^{\rm analytic}(t)$, we obtain the time evolution of $f_{2\pm0}(t) = f_{\rm peak}^{\rm analytic}(t) \pm f_0(t)$. The evolution of $f_{2\pm0}(t)$ during the first milliseconds provides frequency ranges, which are overplotted in Fig. 4.9 (green and orange bands), and as is apparent, they are in good agreement with the $f_{2\pm0}$ peaks.

Furthermore, the frequency range of the coupling between the f_{spiral} and the quasi-radial model (for high-mass models) is estimated from the time-dependent $f_{\mathrm{spiral}-0}(t) = f_{\mathrm{spiral}} - f_0(t)$. The corresponding frequency range is overplotted in Fig. 4.9 (purple bands), and is in good agreement with the $f_{\mathrm{spiral}-0}$ peak.

As for the reference simulation, the main frequency f_{peak} in Fig. 4.9 for many binary masses does not exactly occur in the middle between f_{2-0} and f_{2+0} as is expected for $f_{2\pm0}$. Instead, we find that $\langle f_{\mathrm{peak}}^{t\in[0,t*]}(t)\rangle$ (which is higher than f_{peak} in all models) does agree very well with $\frac{1}{2}(f_{2-0} + f_{2+0})$; i.e., it lies as expected in the middle between the two secondary peaks. The latter can be explained by the fact that the combination tones are rapidly evolving features, and the $\langle f_{\mathrm{peak}}^{t\in[0,t*]}(t)\rangle$ is more representative for $f_{\mathrm{peak}}(t)$ at early times.

5. Analytic models for GWs in NS merger remnants

In this chapter, we present a new analytic model for the gravitational wave emission in the post-merger phase in NS merger remnants. The model consists of a number of physical parameters that are related to different oscillation modes, quasi-linear combination tones or nonlinear features that appear in the GW signal in the post-merger phase. The model incorporates a time-dependent frequency peak $f_{\rm peak}(t)$ described by a two-segment linear expression (see Chapter 4). We evaluate the effectiveness of the model, in terms of the fitting factor, equivalently, the reduction in the detection rate, along a sequence of equal-mass simulations of varying mass. We find that all parameters of the analytic model correlate with the total binary mass of the system. The model achieves high fitting factors for a wide range of binary masses, thus it can be used for the detection and parameter estimation of the post-merger phase in upcoming searches with upgraded second-generation detectors, such as aLIGO+ and aVirgo+, with future, third-generation detectors (Einstein Telescope and Cosmic Explorer) or with dedicated, high-frequency detectors.

5.1. Analytic and semi-analytic post-merger models

We develop analytic waveform models for the post-merger phase employing the spectral analysis of the post-merger GW signals described in Chapter 4. We build an *accurate analytic model* of the post-merger GW signal. Our model extends [42] which included fixed $f_{\rm peak}$, $f_{\rm spiral}$ and f_{2-0} frequencies with exponential damping, and [68] which introduced a linear time dependence, i.e. with a constant slope, of $f_{\rm peak}(t)$ throughout the time evolution. In this work, in comparison to the aforementioned works, we include the higher-frequency combination tone f_{2+0} and employ the two-segment piecewise linear model of Eq. (4.1) to model the time evolution of $f_{\rm peak}(t)$. We note that this model can easily be extended to include additional frequency components, such as $f_{\rm spiral-0}$ for high masses (see Sec. 4.1.3).

In addition to the fully analytic model, we also consider a *semi-analytic model*, which incorporates directly a numerical representation of $f_{\rm peak}(t)$ extracted from the spectrograms. This is extended in Chapter 6 to also include time-dependent secondary components $f_{2\pm0}(t)$.

We note that these models consist of a relatively large number of parameters, and therefore we employ several successive steps in order to determine the model's

parameters.These are described in the following subsections.

5.1.1. Analytic model

The analytic model consists of exponentially decaying sinusoids, where except for the dominant frequency $f_{\rm peak}(t)$, we assume all the other frequencies of the model to be constant in time. The model reads

$$\begin{aligned} h_+(t) &= A_{\rm peak}\, e^{(-t/\tau_{\rm peak})} \cdot \sin(\phi_{\rm peak}(t)) \\ &+ A_{\rm spiral}\, e^{(-t/\tau_{\rm spiral})} \cdot \sin(2\pi f_{\rm spiral} \cdot t + \phi_{\rm spiral}) \\ &+ A_{2-0}\, e^{(-t/\tau_{2-0})} \cdot \sin(2\pi f_{2-0} \cdot t + \phi_{2-0}) \\ &+ A_{2+0}\, e^{(-t/\tau_{2+0})} \cdot \sin(2\pi f_{2+0} \cdot t + \phi_{2+0}), \end{aligned} \tag{5.1}$$

where the $f_{\rm peak}$ component's phase, $\phi_{\rm peak}(t)$, is

$$\phi_{\rm peak}(t) = \begin{cases} 2\pi \left(f_{\rm peak,0} + \frac{\zeta_{\rm drift}}{2} t\right) t + \phi_{\rm peak}, & \text{for } t \le t_* \\ 2\pi\ f_{\rm peak}(t_*)\Big(t - t_*\Big) + \phi_{\rm peak}(t_*), & \text{for } t > t_* \end{cases} . \tag{5.2}$$

In the above expression, the phase $\phi_{\rm peak}$ is continuous and the corresponding frequency $f_{\rm peak}(t) = \frac{1}{2\pi}\frac{d\phi_{\rm peak}}{dt}$ exhibits a dependence as in Eq. 4.1.

In our analysis, the analytic model's parameters are determined in several steps and the model contains several frequency components, and as a result it is not straightforward to find the optimal values which describe the data. We find that by introducing a *normalization factor* $\mathcal{N}$ we obtain better fits with respect to the fitting factor (see Sec. 5.2). We thus define

$$h_+^{\rm Fit}(t) = \mathcal{N} \cdot h_+(t), \tag{5.3}$$

with $h_+(t)$ given as in Eq. (5.1). We drop the normalization factor $\mathcal{N}$ when simpler (under-performing) analytic models are employed (using only one or two frequency components). The normalization factor is only introduced as part of our procedure for determining the best fit, and therefore with other fitting procedures it may not be required.

Lastly, we improve the fits for this particular mass sequence and EoS by introducing a *phenomenological modification* to the analytic model in the description of the $f_{\rm peak}(t)$ component. Our quasi-linear model of Eq. (5.1), presumably due to the nonlinearities that are present immediately after merger, does not accurately describe the very early evolution. We observe a mild delay in the starting times of the exponentially decaying sinusoids between the $f_{\rm peak}$ component and the secondary components $f_{\rm spiral}$ and $f_{2\pm0}$ during the first ≈ 1.0 ms (see the spectograms in Appendix B). The latter is more pronounced in high-mass models. To mimic this delay, we multiply the first line of Eq. (5.1), corresponding to the $f_{\rm peak}$ component, by a Tukey window function, denoted here by $\mathcal{W}(t; s)$, where s is the roll-off parameter. We employ a roll-off parameter $s = 0.075$ for models with $M_{\rm tot} \le 2.9 M_\odot$ and $s = 0.1$ for models with $M_{\rm tot} > 2.9 M_\odot$.

The aforementioned phenomenological introduction of non-linear effects leads to more accurate fits of the initial phases of the secondary components. After ≈ 1.0 ms from the onset of the post-merger phase, when the evolution is close to quasi-linear (linear plus quasi-linear combination tones), the analytic model of Eq. (5.1) is sufficient for its description.

In summary, the complete analytic model of the + polarization of the post-merger signal amplitude reads

$$h_+^{\rm Fit}(t) \;=\; \mathcal{N}\cdot\Big(h_+^{\rm peak}(t)\cdot\mathcal{W}(t;s)+\sum_{\rm i} h_+^{\rm i}(t)\Big), \qquad (5.4)$$
$$\text{for} \quad i=\text{spiral},\, 2\pm 0,$$

where $h_+^{\rm i}(t) = A_{\rm i}\; e^{(-t/\tau_{\rm i})}\cdot\sin(\phi_{\rm i}(t))$.

The cross polarization $h_\times^{\rm Fit}(t)$ is obtained by adopting the parameters for the amplitudes, damping time scales and frequencies from $h_+^{\rm Fit}(t)$ and then assume a phase shift of 90^o degrees to each of the individual initial phases $\phi_{\rm i}$ (for i=peak, spiral, 2 ± 0).

5.1.2. Semi-analytic model

For the semi-analytic model we simply replace the phase $\phi_{\rm peak}(t)$ of the analytic model with the numerical phase $\phi_{\rm peak}^{\rm numerical}(t)$ derived from the spectrogram. We first extract the instantaneous frequency $f_{\rm peak}^{\rm spectrogram}(t)$ from the spectrogram, and then carry out the integration in time to obtain the phase at a particular time step t_i using the iterative formula

$$\phi_{\rm i+1} \;=\; \phi_{\rm i} + 2\pi f_{\rm peak,i}\cdot(t_{\rm i+1}-t_{\rm i})\,, \qquad (5.5)$$

where $\phi_{\rm i}\equiv\phi(t=t_{\rm i})$ and $f_{\rm peak,i}\equiv f_{\rm peak}(t=t_{\rm i})$. The initial phase $\phi_{\rm peak,0}\equiv\phi(t=0)$ is a parameter (like $\phi_{\rm peak}$ in the analytic model).

In Chapter 6 we extend semi-analytic model by including time-dependent secondary components $f_{2\pm0}(t)$ where the phases $\phi_{2\pm0}(t)$ are extracted from the spectrograms in a similar way.

5.1.3. Parameter extraction procedure

In this subsection we describe our multi-step procedure for obtaining the fitting parameters of our model. We first discuss the analytic description of $f_{\rm peak}(t)$, and then describe how we obtain the secondary frequencies $f_{\rm spiral}, f_{2\pm0}, f_{\rm spiral-0}$ from GW spectra. Then, we describe the method for the extraction of model parameters ($A_{\rm i}, \tau_{\rm i}$ for $i=$ spiral$, 2\pm0$) of the secondary components. Finally, we discuss the determination of the remaining parameters $A_{\rm peak}$, $\tau_{\rm peak}$, $\mathcal{N}$, $\phi_{\rm i}$ for $i=$ peak, spiral$, 2\pm0$ and the fit to the simulation data. For all models of our mass sequence we proceed as follows.

Analytic description of $f_{\rm peak}(t)$

The time-dependent $f_{\rm peak}(t)$ is extracted from the spectrograms as the frequency of the maximum wavelet coefficient at time t. $f_{\rm peak}(t)$ is parametrized using the 2-segment piecewise function Eq. (4.1). The parameters $\zeta_{\rm drift}, f_{\rm peak,0}, t_*$ are obtained by fitting the analytic function of Eq. (4.1) to the extracted $f_{\rm peak}(t)$ using a curve fitting routine. Finally, we insert the extracted parameters to the analytic model via $\phi_{\rm peak}(t)$ as in Eq. (5.2).

Secondary frequency peaks

The secondary frequencies $f_{\rm spiral}$, $f_{2\pm0}$ are computed in two steps. First, a rough estimate of the ranges of the different components is obtained, which is necessary to correctly identify the different features. Then we choose the frequency at the maximum in the GW spectrum within the estimated frequency ranges of the different components. We estimate $f_{\rm spiral}$ from the rest-mass density profiles on the equatorial plane (as done in [28]). For the estimate of $f_{2\pm0}$ we use the relation $f_{2\pm0} \approx f_{\rm peak} \pm f_0$. We replace $f_{\rm peak}$ by the mean value of $f_{\rm peak}(t)$ during the first milliseconds, while f_0 is the dominant frequency peak in the Fourier transform of the minimum lapse function $\alpha_{\rm min}$ (see Fig. 4.11). We note that our choices are in agreement with the empirical relations in [49].

Amplitudes A_i and decay timescales τ_i for secondary components

We describe the method to estimate the amplitudes $A_{\rm spiral}$, $A_{2\pm0}$ and timescales $\tau_{\rm spiral}$, $\tau_{2\pm0}$ using the spectrograms. We find that in our results the secondary frequency peaks in the GW spectrum are reproduced better using the following procedure.

We use spectrograms to extract the wavelet coefficients as functions of time t for the frequency components $f_{\rm spiral}$, $f_{2\pm0}$ denoted by $\mathcal{A}_{\rm spiral}(t)$, $\mathcal{A}_{2\pm0}(t)$. Then we consider a signal of the form $A_i\ e^{-t/\tau_i} \cos(2\pi\ f_i \cdot t)$, for $\mathrm{i} = \mathrm{spiral}, 2 \pm 0$, and treat each component separately. We compute the coefficients at $f_{\rm i}$ of this model's signal and using a curve fitting procedure we determine $A_{\rm i}$ and $\tau_{\rm i}$ such that the coefficient function matches the extracted $\mathcal{A}_{\rm i}(t)$. The curve fitting procedure adopts a trust-region-reflective algorithm [149–151].

We note that using this method, the various components are treated independently, and therefore in the case of overlapping frequencies the method loses accuracy since each component amplifies its neighboring component. As a result, the scheme may overestimate the amplitudes A_i. This is compensated by introducing the aforementioned normalization factor $\mathcal{N}$, which we determine in the next step.

Fit to simulation data

In the final step, the remaining parameters $A_{\rm peak}$, $\tau_{\rm peak}$, $\phi_{\rm i}$ for $\mathrm{i} = \mathrm{spiral}, 2 \pm 0$, $\mathcal{N}$ are determined. A fit of the analytic model to the simulation data is carried

out, using the aforementioned curve fitting routine. We insert the previously determined parameters in the analytic model.

We find that parameters of the $f_{\rm peak}$ feature, being the dominant component, are well determined in this step. In contrast, the secondary features of the signal are better reproduced from the spectrograms as described in Sec. 5.3.3.

5.2. Performance of the analytic and semi-analytic models

In this section, we discuss fits of the analytic and semi-analytic models to the GW signals (extracted from simulations) and quantify their performances. We compare the fits to the numerical relativity waveform in the time and frequency domains and examine how well certain GW features are reproduced.

The performance of the models is assessed with the noise-weighted fitting factor defined by

$$\mathrm{FF} \equiv \frac{(h_1, h_2)}{\sqrt{(h_1, h_1)(h_2, h_2)}}, \tag{5.6}$$

where (h_1, h_2) is the noise-weighted inner product between two waveforms and is given by

$$(h_1, h_2) \equiv 4\mathrm{Re}\int_0^\infty df \frac{\tilde{h}_1(f)\cdot\tilde{h}_2^*(f)}{S_h(f)}, \tag{5.7}$$

where $S_h(f)$ is the detector's noise spectral density, and $\tilde{h}_{\rm i}(f)$ is the Fourier transform of the waveform $h_{\rm i}(t)$ (for $i = 1, 2$).

In addition, we introduce simpler versions of our analytic model which include only a subset of GW features. By this, we assess the significance of the individual components of the GW signal.

5.2.1. GW fits

We start by presenting the analysis of the reference simulation ($M_{\rm tot} = 2.5M_\odot$), and then extend the discussion to the sequence of models with other binary masses.

Reference simulation

The parameters of the analytic model Eq. (5.4) for our reference simulation are determined with the method described in Sec. 5.1.3. Figure 5.1 shows the comparison of the simulation data to the analytic model in the time domain. Throughout the whole post-merger evolution of 24 ms, the agreement of the two signals is very good. In the early phase, the dominant and the secondary components are significant, whereas during the later evolution only the $f_{\rm peak}$ component is present. It is important to note that the time-dependent $f_{\rm peak}(t)$ simultaneously leads to a

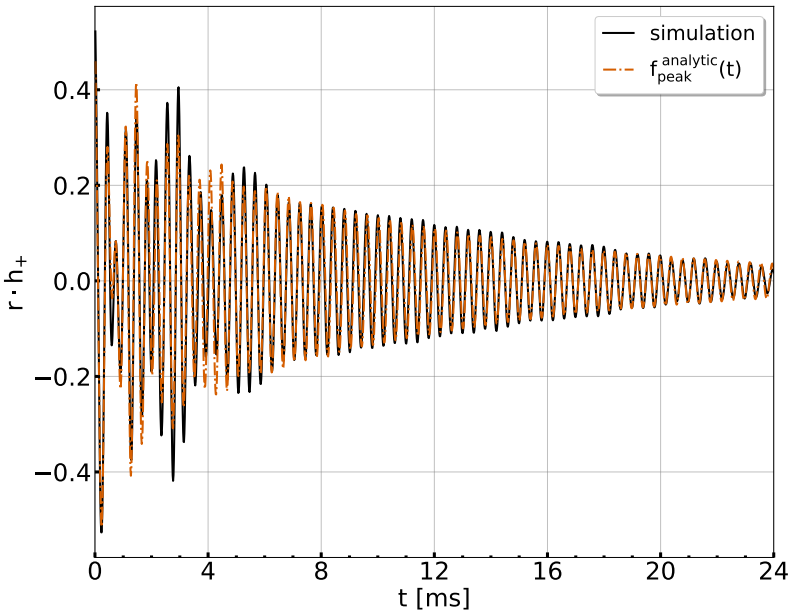

Figure 5.1: GW strain $r \cdot h_+(t)$ for the reference simulation and for the analytic model $h_+^{\rm Fit}(t)$ of Eq. (5.4). Figure taken from [4].

proper description of the early and the late phase. The model captures the phase evolution very well at late times.

The success of the analytic model is also seen in the GW spectrum $h_{\rm eff}(f)$ (see Fig. 5.2). The analytic model reproduces remarkably well the one-sided $f_{\rm peak}$ structure.

We further assess the time evolution of $f_{\rm peak}(t)$ and its analytic model of a 2-segment piecewise linear function $f_{\rm peak}^{\rm analytic}(t)$, Eq. (4.1). For this purpose, we generate the semi-analytic model, as described in Sec. 5.1.2. We extract $f_{\rm peak}^{\rm spectrogram}(t)$ from the spectrogram and insert the numerical phase $\phi_{\rm peak}(t)$ using Eq. (5.5) in the analytic function Eq. (5.4). All other parameters are determined as described in Sec. 5.1.3. We remark that the semi-analytic model cannot be used in real detection scenarios, nevertheless, it is a useful tool for assessing the effectiveness of analytic model. Figure 5.2 displays the resulting GW spectra, which are compared to the numerical waveform from the simulation. As apparent, both models yield spectra that are very close to the spectrum of the numerical simulation. The accuracy of the models is quantified by calculating their fitting factors (with respect to the numerical simulation) assuming the projected Einstein Telescope sensitivity curve [3]. We report fitting factors of FF $= 0.969$ for the semi-analytic model and FF $= 0.956$ for the analytic model. The semi-analytic model yields a slightly higher FF than the analytic model but this is expected since the former contains more accurate information about the $f_{\rm peak}$ component. However, the difference of only 1.34% between the fitting factors of the two models is small and thus demonstrates that using the analytic model $f_{\rm peak}^{\rm analytic}$ instead of the numerically extracted $f_{\rm peak}^{\rm spectrogram}(t)$ is sufficient for the description of the time evolution of the $f_{\rm peak}(t)$ component.

Both the analytic and semi-analytic models successfully reproduce the triplet of secondary frequencies $f_{\rm spiral}$, $f_{2\pm0}$ as demonstrated in Fig. 5.2. This implies that our fitting procedure gives reasonable estimates of the corresponding parameters A_i and τ_i. We note that the secondary peak f_{2-0}, for the purpose of detectability, is more important than f_{2+0}. Nevertheless, the inclusion of f_{2+0} makes the analytic model more complete and increases the quality of the fit because the absence of a frequency component in the early phase may spoil the determination of the other parameters. For similar reasons, the inclusion of the phenomenological Tukey window function $\mathcal{W}(t;s)$ for the $f_{\rm peak}$ component is useful.

Our model does not include the additional frequency peak at 3.5 kHz in Fig. 5.2 and therefore does not reproduce it. This frequency peak remains to be explained and modeled.

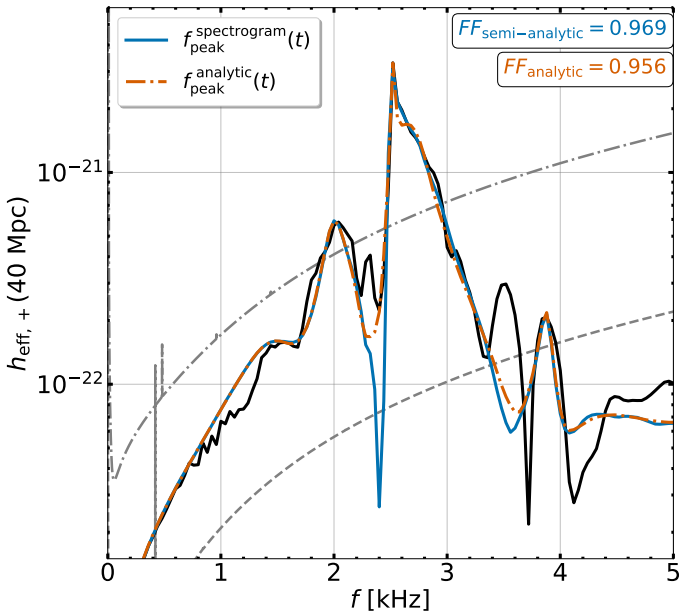

Figure 5.2: Post-merger effective GW spectra $h_{\rm eff,+}(f)$ for the numerical simulation (black line), for the analytic model $h_+^{\rm Fit}(t)$ (orange dashed line) and for the semi-analytic model (cyan line, see text), for the reference simulation. Colored boxes indicate the respective fitting factors FFs. Figure taken from [4].

Figure 5.3 displays the spectrograms of the simulation (upper panel) and of the analytic model (lower panel). We observe a very good agreement considering the simplicity of the analytic model.

Fitting factors along the whole sequence of merger simulations

We test the performance of the analytic model along the sequence of models with different $M_{\rm tot}$ (see Chapter 3.1). The spectra for the analytic fits (in comparison to the simulation spectra) are shown in Fig. 5.4. For all configurations the analytic model performs well. It achieves fitting factors FFs (assuming the sensitivity curve of Einstein Telescope [3]) in the range $[0.955, 0.979]$ for the majority of the models

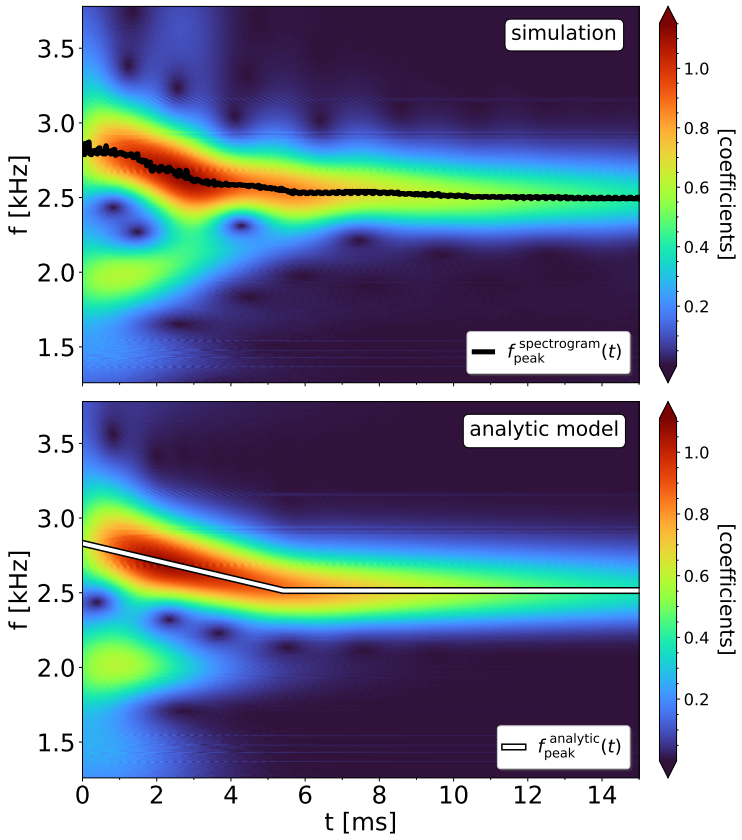

Figure 5.3: *Top panel*: spectrogram of $h_+(t)$ for the reference simulation. The black line corresponds to the numerically extracted $f_{\rm peak}^{\rm spectrogram}(t)$ as described in Fig. 4.1. *Bottom panel*: spectrogram of $h_+^{\rm Fit}(t)$ for the reference simulation. The white line illustrates $f_{\rm peak}^{\rm analytic}(t)$. Figure taken from [4].

with the exception being the most massive configuration of this sequence[1]. For this model (which is close to the threshold for prompt collapse), we find that an extended analytic model (introduced in Chapter 6) achieves a comparable fitting factor of 0.962.

The analytic model reproduces well the secondary frequency components of the spectra in Fig. 5.4. In addition, the shape of the frequency peaks agrees with that obtained from the simulations. This means that the parameter values obtained via our fitting procedure, as described in Sec. 5.1.3, describe well the secondary peaks. However, we note that the amplitude of the f_{2+0} combination tone, A_{2+0}, has to be individually amplified at the end of the above fitting procedure for models with $M_{\rm tot} \geq 2.8 M_\odot$, in order to obtain better agreement with the simulations.

[1] As for the reference simulation, we obtain only slightly better FFs for the semi-analytic model - even for the most massive model - and hence we only report the FFs for the analytic model along the whole sequence.

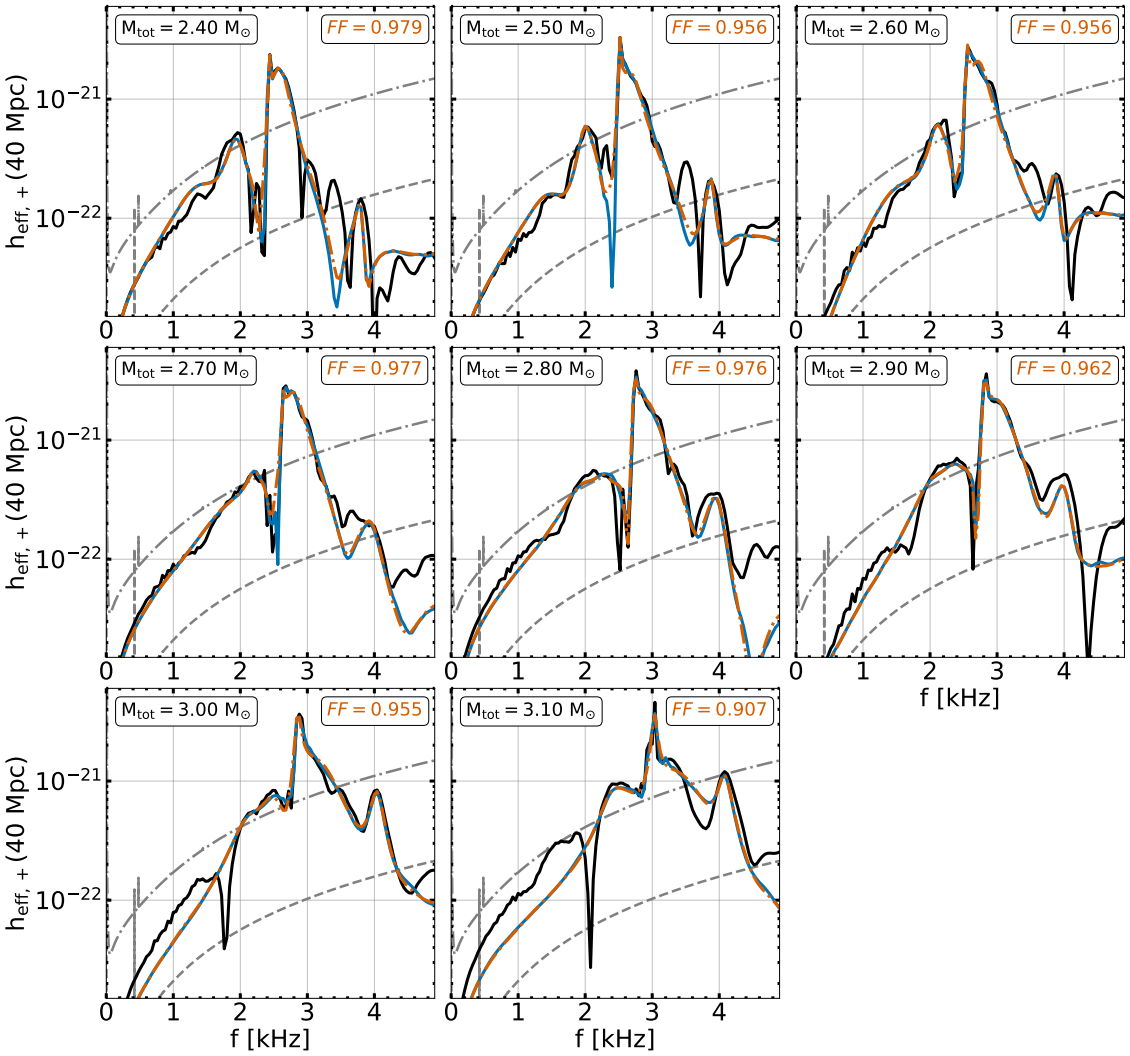

Figure 5.4: Post-merger effective GW spectra $h_{\mathrm{eff},+}(f)$ for the simulations (black lines), for the analytic model (orange dashed line), and the semi-analytic model (cyan line) along the whole sequence of models. The fitting factors FFs for the analytic model are reported in each case. Note that for the highest-mass model with $M_{\mathrm{tot}} = 3.1\ M_{\odot}$ an extended analytic model is introduced in Chapter 6, where a higher FF is achieved. Figure adapted from [4].

5.2.2. Simplified analytic models

To further test our analytic model, we consider simplified analytic models and quantify their performance using FFs. The purpose of such test, is to investigate whether models with less parameters, that are computationally less expensive, yield comparable quality in the fits. As previously, we first study the reference simulation and then extend the discussion to the whole sequence of merger simulations.

Model description	Name	Included components	Performance
`Complete analytic model`	Ac	$f_{\rm peak}^{\rm analytic}(t)$, $f_{\rm spiral}$, f_{2-0}, f_{2+0}	Best
`Complete semi-analytic model`	Sc	$f_{\rm peak}^{\rm spectrogram}(t)$, $f_{\rm spiral}$, f_{2-0}, f_{2+0}	Best
`Simplified (2-component) analytic model`	A2	$f_{\rm peak}^{\rm analytic}(t)$, $f_{\rm spiral}$ or f_{2-0}	Good
`Simplified (1-component) analytic model`	A1	$f_{\rm peak}^{\rm analytic}(t)$	Inadequate
`Simplified (const. frequencies) complete analytic model`	sAc	$\langle f_{\rm peak}^{t\in[0,t_*]}\rangle$, $f_{\rm spiral}$, f_{2-0}, f_{2+0}	Inadequate for this EoS

Table 5.1: Definitions for the various analytic, semi-analytic and simplified models that we consider. When the time-dependence is explicitly written, a time-dependent description is employed for that particular component. Table adapted from [4].

Definitions of the simplified analytic models

We introduce three simplified analytic models. For the first one we only consider the time-dependent $f_{\rm peak}(t)$ component, and for the second one we include the $f_{\rm peak}(t)$ component plus one secondary component. As before, the analytic 2-segment function $f_{\rm peak}^{\rm analytic}(t)$ models the $f_{\rm peak}(t)$ component. For low-mass models, including the reference simulation, the dominant secondary component is the $f_{\rm spiral}$, while for higher mass configurations f_{2-0} becomes the most prominent feature. For the third model, we keep $f_{\rm peak}(t)$ constant and equal to $f_{\rm peak} = \langle f_{\rm peak}^{t\in[0,t_*]}\rangle$, while all the secondary frequency components are included.

We emphasize that for the 2-component model (one secondary component) we do not incorporate the normalization factor $\mathcal{N}$. For the 1-component model we discard the phenomenological window $\mathcal{W}(t;s)$, because it leads to a slightly higher fitting factor in this case.

Table 5.1 summarizes information on the various analytic, semi-analytic and simplified models and their assigned names.

Fitting factors for the reference simulation

We use the aforementioned procedure to compute the fits for the complete analytic model (Ac), the 2-component analytic model (A2), and the 1-component analytic model (A1). We display the corresponding post-merger GW spectra in Fig. 5.5 for the reference simulation. Because all three models include the time-dependent description for $f_{\rm peak}^{\rm analytic}(t)$, as expected, they reproduce well the shape of the $f_{\rm peak}$

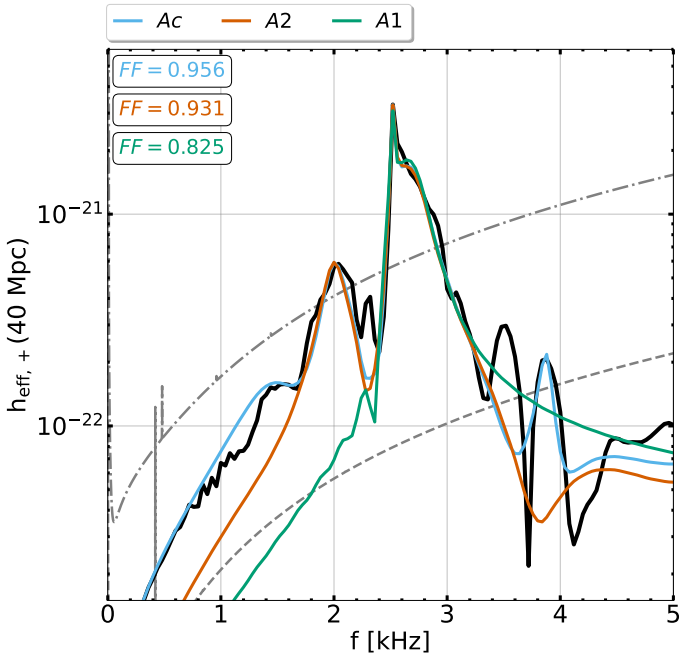

Figure 5.5: Post-merger effective GW spectra $h_{\mathrm{eff},+}(f)$ for the simulation (black lines) and for three analytic models, Ac (cyan line), A2 (orange line) and A1 (green line) for the reference simulation. In each case, the corresponding fitting factor FF is shown. Figure taken from [4].

peak. However, these models differ significantly with respect to the FFs. The complete analytic model achieves FF = 0.956. Unsurprisingly, the fewer components are included in the model, the worse is the value of the fitting factor. The 2-component model achieves FF = 0.931, whereas the 1-component model drops significantly the performance with FF = 0.825.

The impact of the differences in the achieved fitting factors is further understood when we convert them to the reduction in detection rates, which is considered to scale as $(1 - \mathrm{FF}^3) \cdot 100$ [152]. For the reference simulation shown in Fig. 5.5, the complete analytic model achieves a reduction of the detection rate of only 12.63%, whereas the simpler, 2-component and 1-component analytic models suffer from larger reductions of 19.30% and 43.85%, respectively.

The above comparison quantifies the importance of including at least one secondary component to the analytic description of the post-merger phase. This inclusion significantly increases the detectability of the signal with matched-filtered techniques, otherwise more than half of the candidate events would go undetected.

Phase evolution

We perform a comparison between the analytic model fits with respect to the gravitational phase $\phi(t)$ defined by

$$\phi(t) \quad = \quad -\arctan\left(\frac{h_\times(t)}{h_+(t)}\right). \tag{5.8}$$

The phase difference $\Delta\phi(t) = \phi^{\text{fit}}(t) - \phi^{\text{simulation}}(t)$ is computed between the analytic models and the GW signal from the simulation (see Fig. 5.6). In our analysis, the complete semi-analytic model (Sc) where the $f_{\text{peak}}(t)$ component is modeled by $f_{\text{peak}}^{\text{spectrogram}}(t)$ is also included. We split the post-merger signal in two phases: the initial phase, which lasts approximately 8 milliseconds and the late phase referring to the rest of the signal.

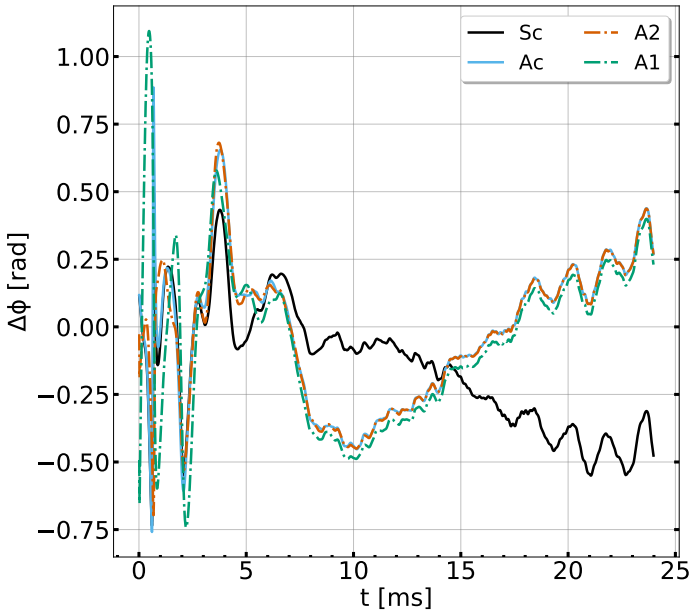

Figure 5.6: Gravitational phase difference $\Delta\phi(t)$ between simulation and analytic or semi-analytic model fits for the reference simulation in post-merger phase. Figure taken from [4].

The phase differences $\Delta\phi(t)$ in the early phase are characterized by low amplitude spikes which are present in all of the analytic models. The semi-analytic model follows the same trends, although with slightly lower amplitudes. The phase difference for the analytic models in the late post-merger phase is dominated by $f_{\text{peak}}^{\text{analytic}}(t)$. That is because by that time the secondary peaks have practically diminished. We note that the semi-analytic model has a phase evolution different from that of the analytic models, although the absolute value $|\Delta\phi(t)|$ is comparable.

Fitting factors along the whole sequence of merger simulations

We compare the fitting factors achieved by the complete analytic (Ac) and semi-analytic (Sc) models, and the simplified analytic models (A2, A1) along the whole sequence of merger simulations in Fig. 5.7. The corresponding reduction in detection rates is reported in Tab. 5.2. We find that the general trend agrees with our findings for the reference simulation, that is, the complete analytic and semi-analytic models perform best leading to the highest fitting factors. For the simple 1-component analytic model the fitting factors are between 0.82 and 0.86 for most

Reduction in detection rates (%)				
$M_{\rm tot}[M_\odot]$	Sc	Ac	A2	A1
2.4	5.01	6.17	9.86	43.03
2.5	9.01	12.63	19.30	43.85
2.6	7.88	12.63	13.45	37.93
2.7	3.56	6.74	21.88	40.52
2.8	5.30	7.03	9.01	42.82
2.9	8.45	10.97	17.73	41.36
3.0	11.53	12.90	22.38	55.75
3.1	24.39	25.39	33.01	72.28

Table 5.2: Reduction in detection rates for various analytic and semi-analytic models. The definition of each model is given in Tab. 5.1. Table taken from [4].

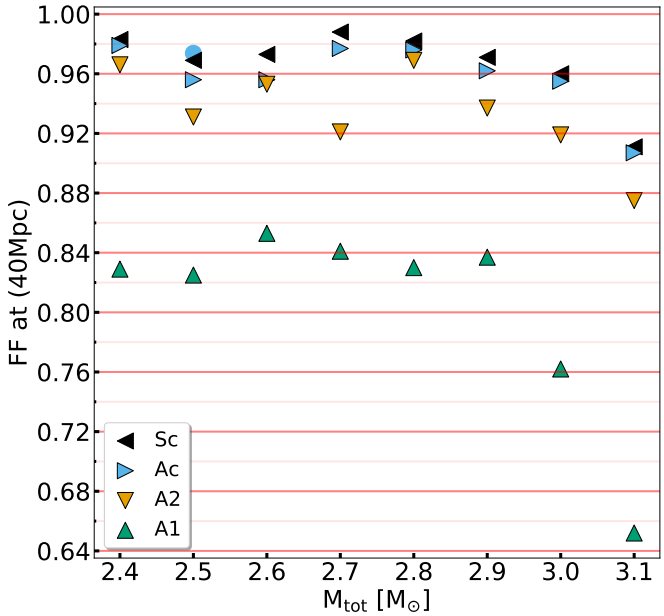

Figure 5.7: Fitting factors FFs for the analytic, and semi-analytic model fits for a source at polar distance of 40 Mpc using the Einstein Telescope sensitivity curve [3]. The blue circle displays the FF for the Ac model fit for the HR simulation (see Appendix A.2). Figure taken from [4].

simulations, however, they deteriorate drastically for the two highest-mass simulations, leading to a reduction of the detection rate of up to 72.28%. Even though the 2-component model performs significantly better than the 1-component model, however, it is still insufficient when compared to the complete analytic or semi-analytic models. We thus conclude that several secondary components such as $f_{\rm spiral}$ and $f_{2\pm0}$ should be included in post-merger GW templates, if a small reduction of the detection has to be achieved.

	Fitting factors (FFs)		Reduction in detection rates (%)	
$M_{\rm tot}[M_\odot]$	Ac	sAc	Ac	sAc
2.4	0.979	0.827	6.17	43.44
2.5	0.956	0.727	12.63	61.58
2.6	0.956	0.773	12.63	53.81
2.7	0.977	0.845	6.74	39.66
2.8	0.976	0.846	7.03	39.45
2.9	0.962	0.824	10.97	44.05
3.0	0.955	0.779	12.90	52.73
3.1	0.907	0.797	25.39	49.37

Table 5.3: Fitting factors FFs and reduction in detection rates (%) for the Ac and sAc analytic models for the post-merger GW emission (see Tab. 5.1 for definitions). Table taken from [4].

Importance of the 2-segment description of $f_{\rm peak}(t)$

We assess the importance of the time-dependent description of $f_{\rm peak}(t)$ in the analytic model in comparison to the constant frequency description. We employ the simplified complete analytic model (sAc) where $f_{\rm peak}(t)$ is constant and equal to $f_{\rm peak} = \langle f_{\rm peak}^{t\in[0,t_*]} \rangle$. Then, we perform the fits for the models Ac, sAc and compare the fitting factors FFs.

The fitting factors along the mass sequence are shown in Tab. 5.3 and Fig. 5.8 (top panel). The model sAc leads to small fitting factors FFs, ranging from 0.727 to 0.846, while the Ac model performs significantly better. The sAc model in terms of the reduction in detection rates, is significantly worse than the Ac model. We note that for the two highest mass models ($M_{\rm tot} = 3.0, 3.1\ M_\odot$) substituting $\langle f_{\rm peak}^{t\in[0,t_*]} \rangle$ with $f_{\rm peak}$ leads to FFs close to the ones obtained with Ac.

5.3. Parameters of the analytic model

In this section we discuss the analytic model's parameters and how they depend on the total binary mass $M_{\rm tot}$. We find a systematic dependence on $M_{\rm tot}$ for all the parameters of the model and obtain analytic descriptions of the respective dependencies using polynomial fits. We first discuss the analytic description of $f_{\rm peak}(t)$ and the parameters which determine the 2-segment piecewise function, Eq. (4.1). Subsequently, we provide empirical relations for the secondary frequency components. We then focus on the amplitudes $A_{\rm i}$, timescales $\tau_{\rm i}$ and normalization factor $\mathcal{N}$. We address the initial phases $\phi_{\rm i}$ and we find additional correlations between these parameters. Finally, with empirical relations for all the parameters of the analytic model (Ac) we construct a purely analytic model which uses exclusively analytic functions and discuss its performance.

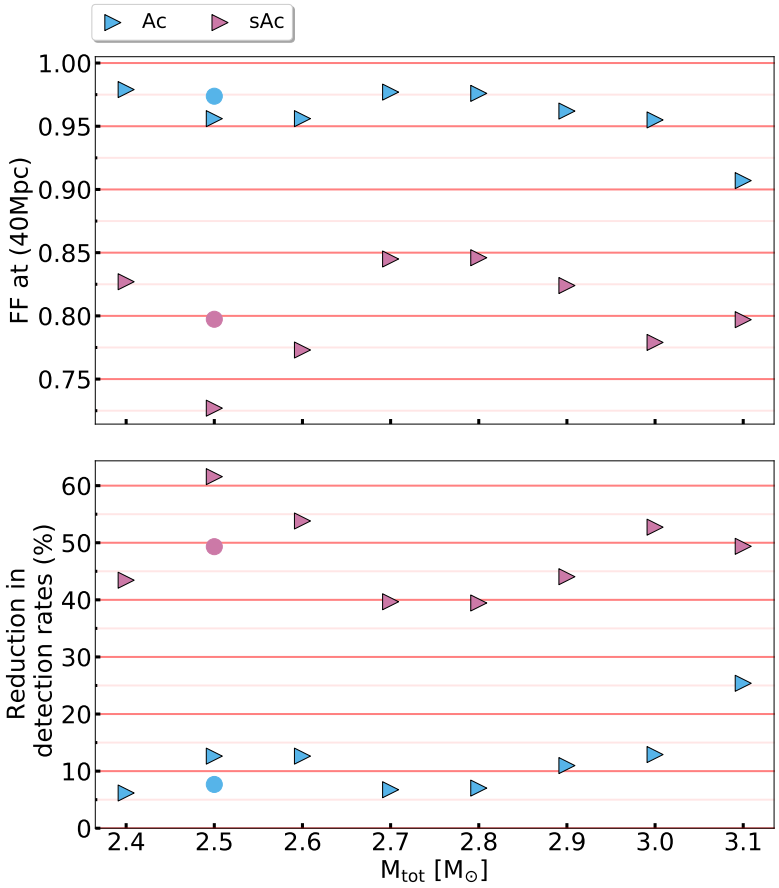

Figure 5.8: *Top panel*: Fitting factors FFs for the Ac and sAc analytic fits. *Bottom panel*: Reduction in detection rates for the Ac and sAc analytic fits. The circles indicate the FF (blue) and reduction in detection rates (pink) for the sAc model fit for the HR simulation (see Appendix A.2). Figure taken from [4].

5.3.1. $f_{\rm peak}(t)$ parametrization

Figure 5.9 displays the parameters $\zeta_{\rm drift}, t_*, f_{\rm peak,0}$, extracted from $f_{\rm peak}(t)$, as functions of total mass $M_{\rm tot}$ for our sequence of simulations. We find that these parameters follow specific dependencies that can be modeled by second and third order polynomials (black lines) respectively, given by

$$\begin{aligned} \zeta_{\rm drift} &= -1.420 \cdot M_{\rm tot}^3 + 11.085 \cdot M_{\rm tot}^2 \\ &\quad -28.834 \cdot M_{\rm tot} + 24.943, \qquad (5.9) \\ f_{\rm peak,0} &= +0.908 \cdot M_{\rm tot}^2 - 3.974 \cdot M_{\rm tot} + 7.058, \qquad (5.10) \\ t_* &= -8.523 \cdot M_{\rm tot}^2 + 40.179 \cdot M_{\rm tot} - 40.741. \qquad (5.11) \end{aligned}$$

The final frequency $f_{\rm peak}(t = t_*)$, which by definition is determined by the parameters $\zeta_{\rm drift}, f_{\rm peak,0}, t_*$ (black dashed curve) is determined by Eq. (5.9)-(5.11)) is shown in (bottom) Fig. 5.9.

The parameter $f_{\rm peak}(t_*)$ (see Fig. 5.9) approximately coincides with $f_{\rm peak}$ (defined as the frequency of the highest peak in the GW spectra). It also increases

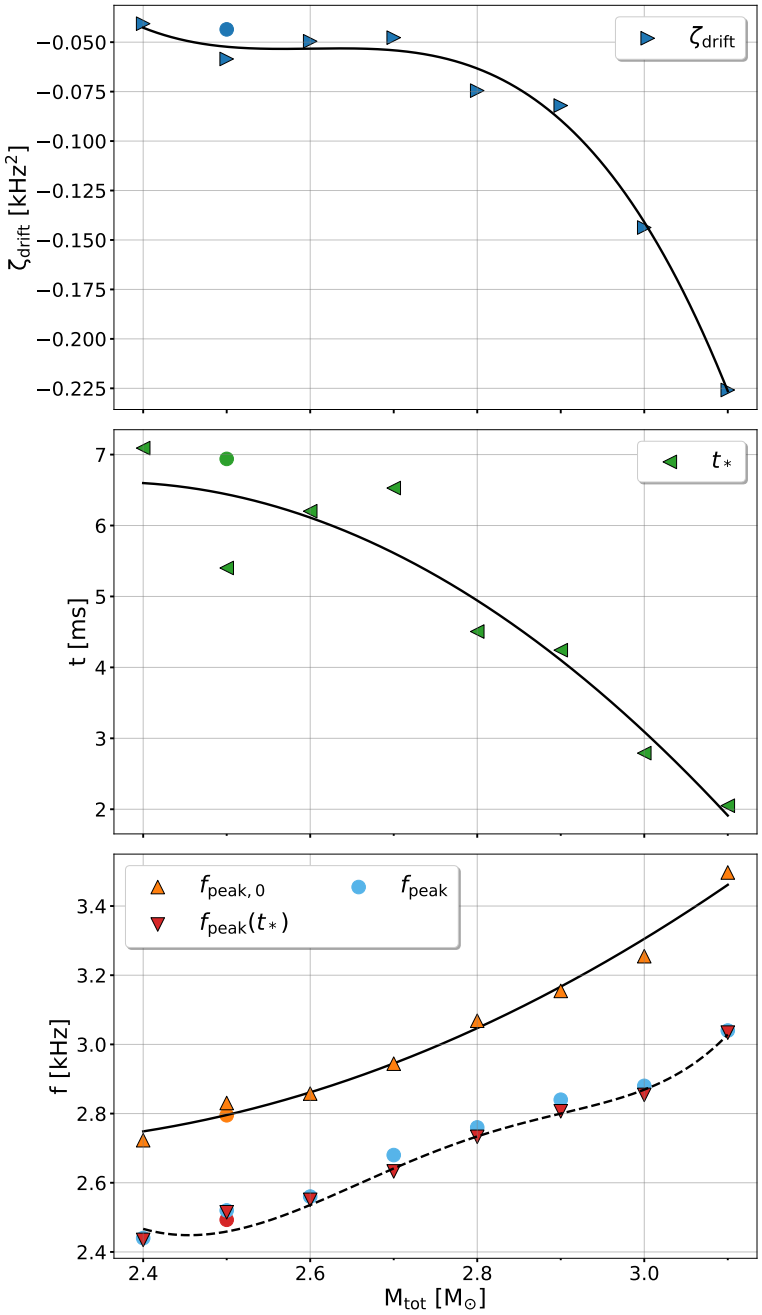

Figure 5.9: *Top panel*: $\zeta_{\rm drift}$ parameter along the mass sequence. The black curve shows a third order polynomial fit. *Middle panel*: t_* parameter along the mass sequence. The black curve shows a second order polynomial fit. *Bottom panel*: $f_{\rm peak,0}$ parameter (orange) along the mass sequence. The black solid curve shows a second order polynomial fit. In addition, data points (red) along the mass sequence are shown for $f_{\rm peak}(t_*)$, which is determined by $\zeta_{\rm drift}$, $f_{\rm peak,0}$, t_*. The black dashed curve is determined by polynomial fits to $\zeta_{\rm drift}$, $f_{\rm peak,0}$, t_*. Cyan circles indicate the $f_{\rm peak}$ extracted from the GW spectra (see Fig. 4.9). The circles indicate the respective parameters (for each figure) for the HR simulation (see Appendix A.2). Figure taken from [4].

with the total mass $M_{\rm tot}$ because the remnant becomes more compact. We note that $f_{\rm peak,0}$ shows a similar dependence on the total mass $M_{\rm tot}$. We previously mentioned that the evolution of $f_{\rm peak}(t)$ becomes faster and more significant for high-mass configurations, and that is confirmed by the difference $\Delta f_{\rm peak} = f_{\rm peak,0} - f_{\rm peak}(t_*)$. $\Delta f_{\rm peak}$ increases with total mass $M_{\rm tot}$ from 0.288 kHz for the model with the lowest mass to 0.462 kHz for the configuration with $M_{\rm tot} = 3.1 M_\odot$.

The duration of the frequency drift, t_*, is a decreasing function of the total binary mass $M_{\rm tot}$. We note that it is possible for t_*, in particular, to depend on the numerical scheme, resolution and physics of the simulation tool, which can affect the angular momentum redistribution of the remnant and possibly prolong or shorten the drift.

The slope parameter $\zeta_{\rm drift}$ is approximately constant ($\approx -0.060{\rm kHz}^2$) for $M_{\rm tot} \leq 2.8\ M_\odot$. However, a rapid decrease occurs as the total mass $M_{\rm tot}$ approaches $M_{\rm thres}$ (see Fig. 5.9). Such a trend may not be unexpected as a result of an accelerated evolution of the remnant (in the early post-merger phase) due to the strong gravity.

If it is possible to extract $\zeta_{\rm drift}$, t_* and $\Delta f_{\rm peak}$, one may use this information to estimate the proximity to a prompt collapse. For this, the occurrence of a faster frequency evolution for high-mass binaries should be confirmed for other EoS models, possibly considering $\zeta_{\rm drift}$, t_*, $\Delta f_{\rm peak}$ relative to $f_{\rm peak}$, instead of absolute values.

5.3.2. Secondary frequencies $f_{\rm spiral}$, $f_{2\pm0}$

Figure 5.10 shows the secondary frequency components $f_{\rm spiral}$, $f_{2\pm0}$ as a function of the total binary mass $M_{\rm tot}$. For comparison, we also show the mean value $\langle f_{\rm peak}^{t\in[0,t*]}(t)\rangle$ as a function of $M_{\rm tot}$. All these frequencies follow specific trends which we model with linear and second order polynomials for the f_{2+0} and $f_{\rm spiral}$, f_{2-0}, respectively. The fits read

$$f_{\rm spiral} = +0.319 \cdot M_{\rm tot}^2 - 0.758 \cdot M_{\rm tot} + 1.914, \quad (5.12)$$

$$f_{2-0} = +0.236 \cdot M_{\rm tot}^2 + 0.167 \cdot M_{\rm tot} - 0.433, \quad (5.13)$$

$$f_{2+0} = +0.371 \cdot M_{\rm tot} + 2.929. \quad (5.14)$$

The fit for $\langle f_{\rm peak}^{t\in[0,t*]}(t)\rangle$ is determined by the fits for $\zeta_{\rm drift}, t_*, f_{\rm peak,0}$ (see Chapter 5.3.1).

5.3.3. Amplitudes, timescales, normalization factor

We discuss the properties of the dominant component's parameters $A_{\rm peak}$, $\tau_{\rm peak}$, the parameters of the secondary components $A_{\rm spiral}$, $A_{2\pm0}$, $\tau_{\rm spiral}$, $\tau_{2\pm0}$ and the normalization factor $\mathcal{N}$. The parameters determined for the complete analytic model (Ac) are employed.

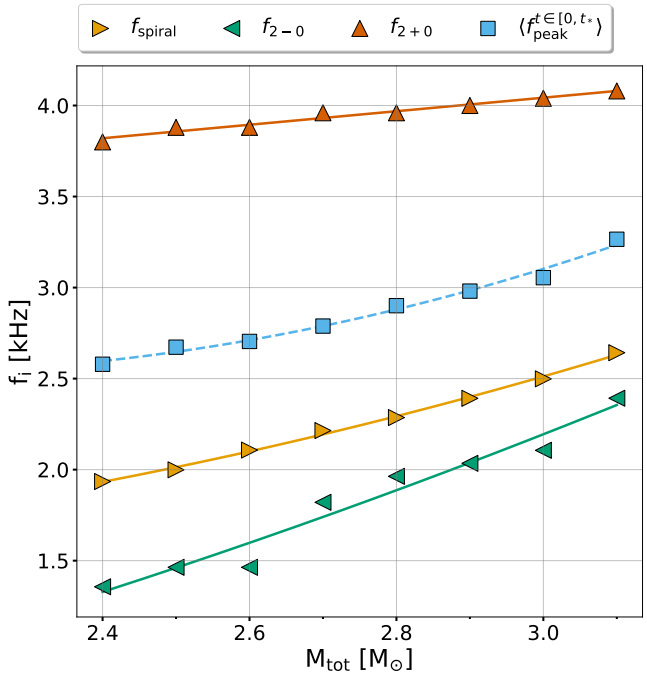

Figure 5.10: Secondary frequencies $f_{\rm spiral}$, $f_{2\pm0}$ and mean $\langle f_{\rm peak}^{t\in[0,t*]}(t)\rangle$ as a function of total binary mass. Continuous curves indicate the corresponding linear and second order polynomial fits.

$A_{\rm peak}$ and $\tau_{\rm peak}$

The parameters $A_{\rm peak}$, $\tau_{\rm peak}$ are displayed in Fig. 5.11a, 5.11b. $A_{\rm peak}$ and $\tau_{\rm peak}$ follow dependencies, which can be modeled by second order polynomial fits given by

$$A_{\rm peak} = -0.409 \cdot M_{\rm tot}^2 + 3.657 \cdot M_{\rm tot} - 6.130, \quad (5.15)$$
$$\tau_{\rm peak} = +7.782 \cdot M_{\rm tot}^2 - 53.040 \cdot M_{\rm tot} + 93.542. \quad (5.16)$$

$A_{\rm peak}$ increases with $M_{\rm tot}$, which may be expected, because the involved masses are higher and also the initial excitation is more pronounced. $\tau_{\rm peak}$ decreases as the total binary mass $M_{\rm tot}$ increases, indicating a stronger damping.

$A_{\rm spiral}, A_{2\pm0}, \tau_{\rm spiral}$ and $\tau_{2\pm0}$

The parameters A_i, τ_i (for i = spiral, 2 ± 0) are shown in Fig. 5.12a, 5.12b. The amplitudes $A_{\rm i}$ and timescales $\tau_{\rm i}$ exhibit dependencies on the total mass $M_{\rm tot}$ and follow specific trends. We quantify these trends by performing second order polynomial fits resulting in

$$\tau_{\rm spiral} = -0.874 \cdot M_{\rm tot}^2 + 3.521 \cdot M_{\rm tot} - 2.005, \quad (5.17)$$
$$\tau_{2-0} = +2.057 \cdot M_{\rm tot}^2 - 10.804 \cdot M_{\rm tot} + 14.606, \quad (5.18)$$
$$\tau_{2+0} = +8.469 \cdot M_{\rm tot}^2 - 48.785 \cdot M_{\rm tot} + 71.671, \quad (5.19)$$

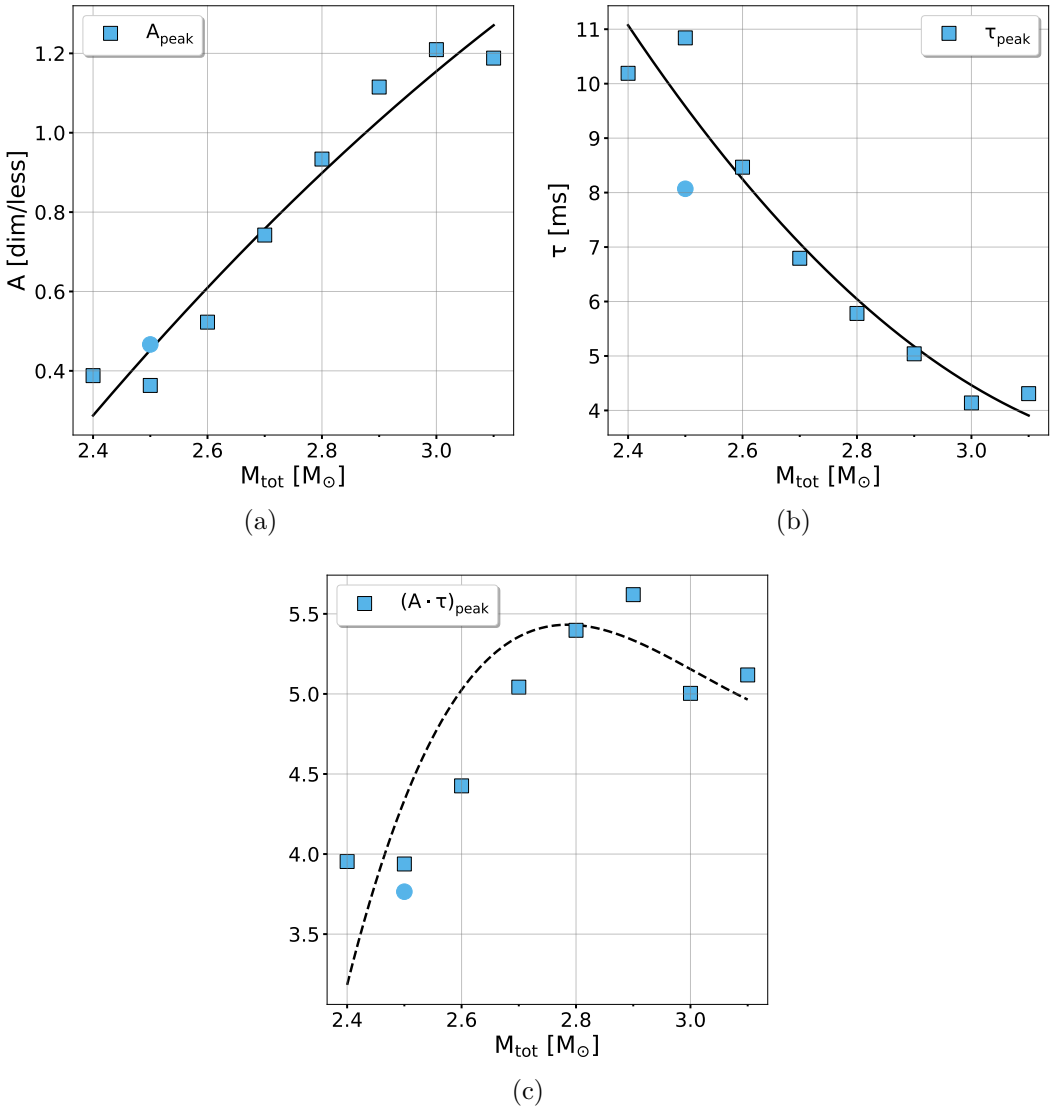

Figure 5.11: *Top left panel*: Analytic model dimensionless amplitude $A_{\rm peak}$ for $r \cdot h_+(t)$ for the analytic model which employs the $f_{\rm peak}^{\rm analytic}(t)$ description. Black curve corresponds to second order polynomial fit. *Top right panel*: Analytic model timescale $\tau_{\rm peak}$ for the analytic model which employs the $f_{\rm peak}^{\rm analytic}(t)$ description. Black curve corresponds to second order polynomial fit. *Bottom panel*: Analytic model products $(A \cdot \tau)_{\rm peak}$. Black dashed curves determined by fits to $A_{\rm peak}, \tau_{\rm peak}$. The blue circles indicate the respective parameters (for each figure) for the HR simulation (see Appendix A.2). Figure adapted from [4].

$$A_{\rm spiral} = +2.649 \cdot M_{\rm tot}^2 - 13.580 \cdot M_{\rm tot} + 17.752, \quad (5.20)$$

$$A_{2-0} = -1.704 \cdot M_{\rm tot}^2 + 10.004 \cdot M_{\rm tot} - 13.909, \quad (5.21)$$

$$A_{2+0} = +0.816 \cdot M_{\rm tot}^2 - 3.920 \cdot M_{\rm tot} + 4.734. \quad (5.22)$$

These relations are not particularly tight, especially for A_{2-0} and $\tau_{\rm spiral}$. This is likely caused by the difficulty to precisely extract secondary features from the complex signal. However, the amplitudes of all secondary features clearly increase

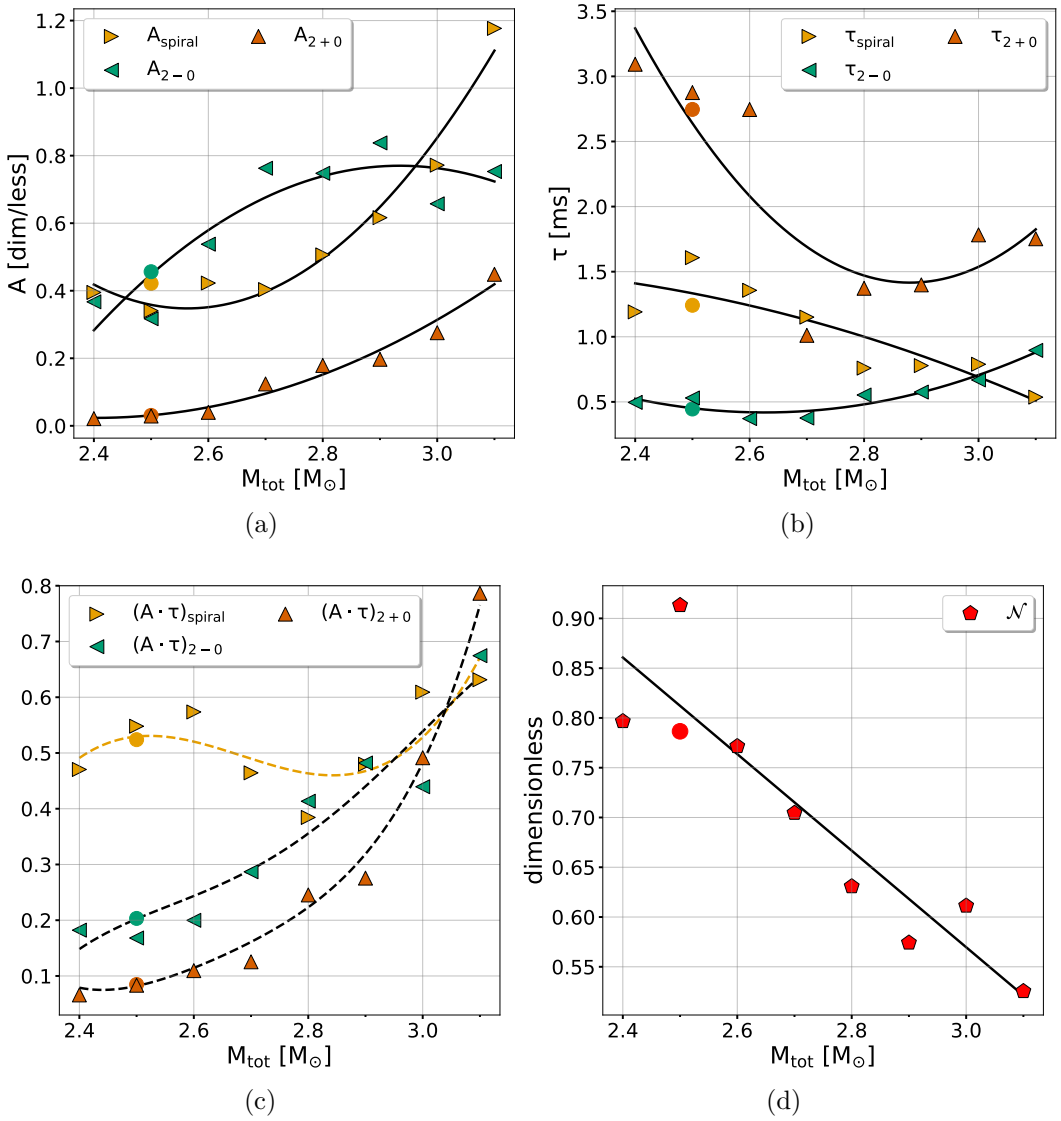

Figure 5.12: *Top left panel*: Analytic model dimensionless amplitudes $A_{\rm spiral}$, A_{2-0}, A_{2+0} for $r \cdot h_+(t)$ extracted from spectrograms. Black curves correspond to second order polynomial fits. *Top right panel*: Analytic model timescales $\tau_{\rm spiral}$, τ_{2-0}, τ_{2+0} extracted from spectrograms. Black curves correspond to second order polynomial fits. *Bottom left panel*: Analytic model products $(A \cdot \tau)_{\rm spiral}$, $(A \cdot \tau)_{2-0}$, $(A \cdot \tau)_{2+0}$. Black dashed curves determined by polynomial fits to A_i, τ_i for i=spiral,2 $\pm$ 0. Yellow dashed curve corresponds to the fourth order polynomial fit to $(A \cdot \tau)_{\rm spiral}$. *Bottom right panel*: Analytic model correction factor $\mathcal{N}$ for the analytic model which employs the $f_{\rm peak}^{\rm analytic}(t)$ description. Black curve corresponds to a linear fit. The colored circles indicate the respective parameters (for each quantity and figure) for the HR simulation (see Appendix A.2). Figure adapted from [4].

with mass.

The components $f_{2\pm0}$ become more prominent as the total mass $M_{\rm tot}$ increases, and this is seen in $A_{2\pm0}$ too (see Fig. 5.12a). This trend is understandable, due

to the stronger excitation of the radial oscillation mode which occurs for high-mass models. For low-mass configurations, the coupling to the radial oscillation is significantly suppressed (see Fig. 4.10), and consequently the amplitudes of the couplings f_{2-0} and f_{2+0} should be small, which is only the case for the f_{2+0} component. The relatively high amplitude A_{2-0} for small $M_{\rm tot}$ is most likely an artifact of the fit and is compensated by a very small decay timescale. As such, the weakness of the radial oscillation implies that the damping times $\tau_{2\pm0}$ are not very meaningful measures for low-mass systems. For higher total binary masses there is a noticeable mild increase of $\tau_{2\pm0}$, and this is in line with the behavior in Fig. 4.10. The $f_{\rm spiral}$ component's timescales show a mild decrease, corresponding to a faster dissipation of the tidal bulges. The amplitude of the $f_{\rm spiral}$ component similarly increases with $M_{\rm tot}$.

In addition, we consider the product $(A \cdot \tau)_{\rm i}$ as a quantitative measure for the strength of a secondary feature. The products $(A{\cdot}\tau)_{\rm i}$ for each frequency component are shown in Fig. 5.12c. Equations (5.17)-(5.22) are used in order to derive analytic expressions displayed by dashed curves. As expected, the products $(A \cdot \tau)_{2\pm0}$ increase systematically with $M_{\rm tot}$ and closely follow the analytic expressions. The product $(A \cdot \tau)_{\rm spiral}$ is roughly constant [2].

The strength of the secondary components quantified as in Fig. 5.12c resembles the behavior which was anticipated in [28]. It reproduces the different types of post-merger GW emission: for low-mass binaries the $f_{\rm spiral}$ component is dominant (Type III in the notation of [28]), for intermediate masses the strength of $f_{\rm spiral}$ and f_{2-0} is roughly comparable (Type II), and for models with very high $M_{\rm tot}$ the couplings with the radial oscillation are dominant over $f_{\rm spiral}$ (Type I). Thus, the products $(A \cdot \tau)_{\rm i}$ may serve as a quantitative measure to classify different types of post-merger dynamics and GW emission including the morphology of the spectrum.

We note that the method we employ for the derivation of $A_{\rm i}$, $\tau_{\rm i}$ introduces a bias whenever f_{2-0} and $f_{\rm spiral}$ are close (see Sec. 5.3.3). This is possibly one of the reasons for the scattering of $A_{\rm i}$, $\tau_{\rm i}$ from the analytic fits.

Normalization factor $\mathcal{N}$

The normalization factor $\mathcal{N}$ as a function of total mass $M_{\rm tot}$ for fits with the complete analytic model (Ac) is shown in Fig. 5.12d. We find a linear dependence on $M_{\rm tot}$ modeled by

$$\mathcal{N} \;=\; -0.485 \cdot M_{\rm tot} + 2.025 \tag{5.23}$$

For low-mass configurations, $\mathcal{N}$ becomes less important (close to 1) and more significant (close to 0.50) for high-mass configurations. One reason for such a trend may be that for estimating $A_{\rm i}$, $\tau_{\rm i}$ we treat each component separately. Since in low-mass configurations the components $f_{\rm spiral}$ and f_{2-0} are well separated, the parameters $A_{\rm i}$, $\tau_{\rm i}$ are accurately derived. In contrast, for high-mass configurations,

[2] $(A \cdot \tau)_{\rm spiral}$ shows a large scatter from the derived analytic expression (using Eq. (5.20), (5.17)), however, we find that a fourth order polynomial fit describes well the trend.

where the peaks overlap, the parameters may be overestimated and the correction becomes necessary.

Another reason may be the fact that the $f_{2\pm0}$ components are significantly weaker than the $f_{\rm spiral}$ components for low-mass systems (see e.g. the products $(A\cdot\tau)_{\rm i}$), and as a result, their contribution to the total signal is minor, and so, a single secondary feature does not require significant corrections by the normalization factor.

5.3.4. Initial phases $\phi_{\rm peak}$, $\phi_{\rm spiral}$, $\phi_{2\pm0}$

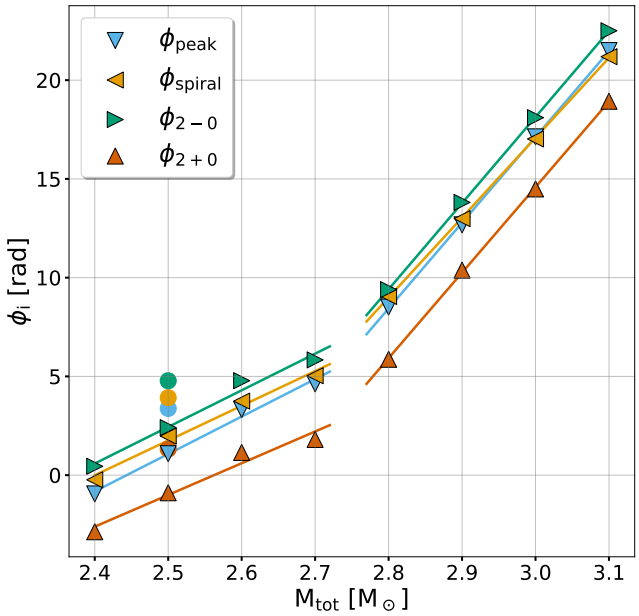

Figure 5.13: Initial phases $\phi_{\rm i}$ (for i=peak, spiral, 2 ± 0) for the analytic model which employs the $f_{\rm peak}^{\rm analytic}(t)$ description as a function of total binary mass. Colored curves correspond to piecewise linear fits. The colored circles indicate the respective parameters for the HR simulation (see Appendix A.2). Figure taken from [4].

We discuss the properties of the initial phases $\phi_{\rm i}$ (for i = peak, spiral, 2 ± 0) for all the models in the sequence of simulations. In this analysis we add multiples of 2π to the initial phases $\phi_{\rm i}$ such that $\phi_{\rm i}(M_{\rm tot})$ becomes an increasing function (see Fig. 5.13).

We find a tight correlation between $\phi_{\rm i}$ and the total mass $M_{\rm tot}$. This dependence is modeled with a 2-segment piecewise function consisting of two linear fits which intersect at total mass of $M_{\rm tot} = 2.7\ M_\odot$ (see Appendix B.2).

We stress that these remarkably tight correlations imply that the properties of the gravitational phase $\phi(t)$ (see Eq. (5.8)) in the early post-merger phase depend systematically on the total mass $M_{\rm tot}$.

We also find tight correlations between the initial phases $\phi_{\rm spiral}$, $\phi_{2\pm0}$ and $\phi_{\rm peak}$

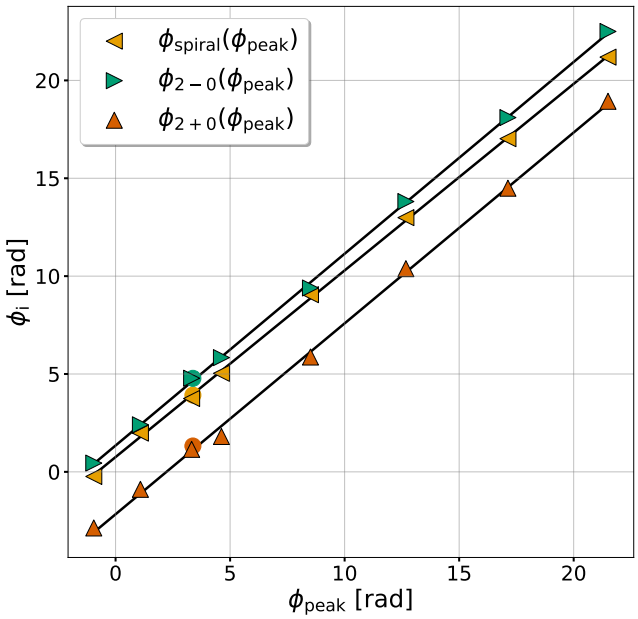

Figure 5.14: Initial phases $\phi_{\rm i}$ (for i=spiral, 2 ± 0) with respect to $\phi_{\rm peak}$ for the analytic model which employs the $f_{\rm peak}^{\rm analytic}(t)$ description. Black curves correspond to linear fits. The colored circles indicate the respective parameters for the HR simulation (see Appendix A.2). Figure taken from [4].

as shown in Fig. 5.14. These correlations are modeled with linear fits given by

$$\phi_{\rm spiral} = +0.953 \cdot \phi_{\rm peak} + 0.756 \tag{5.24}$$
$$\phi_{2-0} = +0.980 \cdot \phi_{\rm peak} + 1.345 \tag{5.25}$$
$$\phi_{2+0} = +0.975 \cdot \phi_{\rm peak} - 2.166. \tag{5.26}$$

There is only a small difference, at most by 3%, between the slope parameters in Eq. (5.24)-(5.26) and therefore they are approximately equal. We note that the slopes are also close to 1. The latter would imply a constant difference in phase between the $f_{\rm peak}$ component and the secondary components. These relations and the ones shown in Fig. 5.13 may be in reality even tighter and the small but finite scatter results from finite resolution in the simulations or the fitting procedure. Tight relations like these can be employed to reduce the complexity of the analytic fit by reducing the parameter space.

We find that the $\phi_{\rm peak}(M_{\rm tot})$ and $\phi_{\rm spiral}(\phi_{\rm peak})$, $\phi_{2\pm0}(\phi_{\rm peak})$ relations (see Eq. (5.24) to Eq. (5.26)) can be used to reduce the number of the analytic model's parameters (and thus the complexity of the fitting procedure) and still obtain good fits to the data. We test this by substituting the initial phases $\phi_{\rm i}$ with the predictions made by Eq. (B.1), Eq. (5.24)-(5.26). We find that the FFs only differ by a few percent (0.5-3%) compared to fits to the analytic model. When we perform a phase alignment in the waveforms the FFs differ by at most by $\approx$1% .

We overplot the initial phases $\phi_{\rm i}$ (for i=peak, spiral, 2 ± 0) for the HR simulation in Figures 5.13 and 5.14 (see Appendix A.2). These appear to be slightly larger than the ones from the mass sequence simulations, however, their relative

difference is similar to the mass sequence simulations as corroborated by Fig. 5.14.

Furthermore, we find that these tight correlations between the initial phases (Eq (5.24)-(5.26)) are unaffected by residual eccentricities in the ID (see Fig. A.3 and Appendix A.1).

5.3.5. Purely analytic model

Fitting Factors (FFs)			
$M_{\rm tot}[M_\odot]$	Ac	$\mathcal{P}(M_{\rm tot}, t)$	$\mathcal{P}(M_{\rm tot}, t; \phi_{\rm peak})$
2.4	0.979	0.653	0.801
2.5	0.956	0.795	0.847
2.6	0.956	0.912	0.913
2.7	0.977	0.878	0.922
2.8	0.976	0.878	0.899
2.9	0.962	0.848	0.905
3.0	0.955	0.595	0.864
3.1	0.907	0.887	0.898

Table 5.4: Fitting factors FFs for the analytic model Ac fits, the purely analytic model $\mathcal{P}(M_{\rm tot}, t)$, and the analytic model with one free parameter $\mathcal{P}(M_{\rm tot}, t; \phi_{\rm peak})$. Table taken from [4].

Furthermore, we introduce a *purely analytic model* $\mathcal{P}(M_{\rm tot}, t)$. This is possible due to the systematic dependence of all the parameters of the analytic model on the total binary mass. The model uses the analytic functions Eq. (5.9)-(5.23),(B.1)-(B.4), which depend only on $M_{\rm tot}$.

The model's performance is evaluated by computing the respective FFs. Table 5.4 shows the FFs for the analytic model $\mathcal{P}(M_{\rm tot}, t)$ compared to the Ac analytic fits. We observe a significant drop in the FFs as expected, however, the majority of the fits still result in FFs $\gtrsim 0.80$. The FFs can be further improved by considering an analytic model where $\phi_{\rm peak}$ is treated as a free parameter, denoted by $\mathcal{P}(M_{\rm tot}, t; \phi_{\rm peak})$. In this case, almost all configurations lead to FFs $\gtrsim 0.85$ (see Tab. 5.4).

These considerations show that it may be possible to determine the different analytic functions Eq. (5.9)-(5.23),(B.1)-(B.4) (or only piecewise linear segments of these functions) by several simulations and anticipated observations and then use those functions to interpolate the model in $M_{\rm tot}$.

6. Models close to prompt collapse

In this chapter we discuss the spectral properties of configurations with a total mass $M_{\rm tot}$ close to threshold mass for prompt collapse $M_{\rm thres}$. For these high-mass configurations, FFs decrease, which indicates that our model becomes less accurate.The first modification consists of a time-dependent treatment of $f_{2\pm0}(t)$, while the second is the inclusion of the $f_{\rm spiral-0}$ component (see Tab. 6.1). Finally, we describe how different frequency components and their higher-order combination tones may explain most of the spectral features in the GW spectrum.

6.1. Extended analytic models and GW fits

We separately introduce two modifications to the analytic model. First, we consider a dynamical evolution of $f_{2\pm0}(t)$. Second, we include the $f_{\rm spiral-0}$ component, i.e., an additional coupling between $f_{\rm spiral}$ and f_0 (see Sec. 4.1.3). Table 6.1 summarizes information for the extended analytic models.

Model description	Name	Components
`Extended analytic model 1`	M1	$f_{\rm peak}^{\rm analytic}(t)$, $f_{\rm spiral}$, $f_{2-0}(t)$, $f_{2+0}(t)$
`Extended analytic model 2`	M2	$f_{\rm peak}^{\rm analytic}(t)$, $f_{\rm spiral}$, f_{2-0}, f_{2+0}, $f_{\rm spiral-0}$

Table 6.1: Definitions for the two extended analytic models. When the time argument is explicitly written, a time-dependent description is employed for that particular component. Table taken from [4].

The importance of the time evolution of $f_{2\pm0}(t)$ is assessed by extracting $f_{2\pm0}(t)$ from spectrograms (see Chapter 4) and inserting the numerically extracted values into the analytic model (see Sec. 5.1.2). We find below that even the complete numerical description of $f_{2\pm0}(t)$ yields only a minor improvement, and thus we do not further discuss a parametrization of $f_{2\pm0}(t)$.

The fits to the simulation with total binary mass $M_{\rm tot} = 3.1\ M_\odot$ for the extended analytic models are shown in Fig. 6.1. We find that the inclusion of the time-evolving components $f_{2\pm0}(t)$ leads to a mild increase of the fitting factor: $\mathrm{FF}_{\rm new,1} = 0.916$ compared to the original of $\mathrm{FF}_{\rm old} = 0.907$ (see Sec. 5.2.1). This increase in FF slightly improves the reduction in detection rates from 25.39% to 23.14%. We also note that the model with the dynamical $f_{2\pm0}(t)$ qualitatively reproduces a small peak at approximately 1.9 kHz (orange curve in Fig. 6.1). However, it still does not yield a good description of the simulation below 2 kHz.

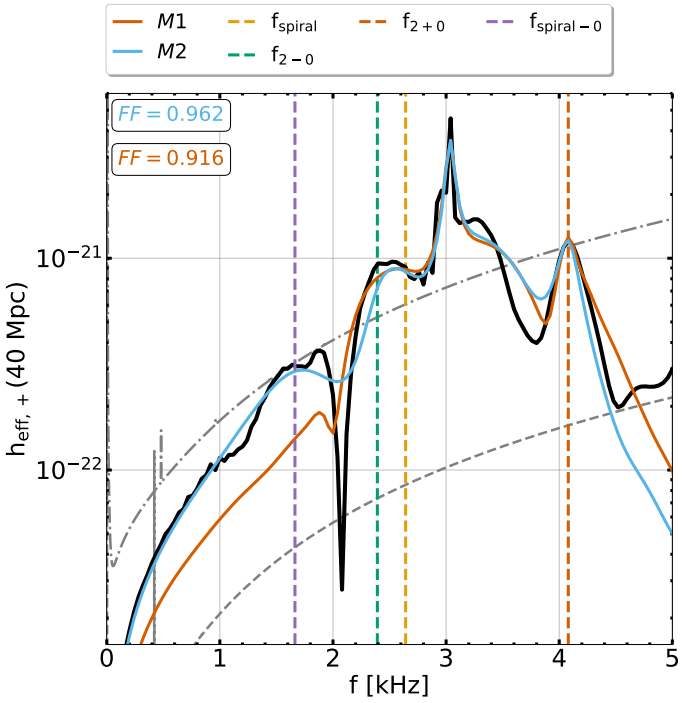

Figure 6.1: Effective GW spectra $h_{\mathrm{eff},+}(f)$ for simulation, and analytic models for $\mathrm{M_{tot}} = 3.1\ \mathrm{M_\odot}$ model. Black line corresponds to the simulation. Colored curves illustrate the analytic model fits as described by the labels. Colored boxes show the corresponding fitting factors FFs. Dashed vertical lines indicate secondary frequencies. Figure taken from [4].

The blue curve in Fig. 6.1 includes the $f_{\mathrm{spiral}-0}$ component. We assume the frequency $f_{\mathrm{spiral}-0}$ to be constant and we also adopt constant values for $f_{2\pm0}$ as in the original model. Since we do not observe a distinct peak in the GW spectrum for the frequency $f_{\mathrm{spiral}+0}$, we do not incorporate this component in our modified analytic model. We determine the parameters $A_{\mathrm{spiral}-0}$, $\tau_{\mathrm{spiral}-0}$ from the spectrograms as described in Sec. 5.1.3.

The inclusion of the $f_{\mathrm{spiral}-0}$ component substantially increases the fitting factor $\mathrm{FF_{new,2}} = 0.962$. The reduction in the detection rates is significantly improved to 11%. The importance of the $f_{\mathrm{spiral}-0}$ component is also apparent in the GW spectrum (compare orange and blue curve below 2 kHz). The $f_{\mathrm{spiral}-0}$ component has a large impact on the FF because as previously mentioned, the strength of $f_{\mathrm{spiral}-0}$ relative to frequency dependent sensitivity curve is similar to f_{2+0} (for this mass configuration).

We remark that the first modification (time-evolving $f_{2\pm0}(t)$) only slightly improves the analytic fits but increases the complexity of the model since a parametrization of $f_{2\pm0}(t)$ would require a number of additional parameters. The second modification (inclusion of $f_{\mathrm{spiral}-0}$) improves significantly the analytic fits (with respect to FFs) and only introduces a minimum of new parameters ($A_{\mathrm{spiral}-0}$, $\tau_{\mathrm{spiral}-0}$, $\phi_{\mathrm{spiral}-0}$), while the frequency is already derived from the other components).

6.2. Additional spectral features

Finally, we note that the different components and their couplings provide explanations for basically every feature in the GW spectrum up to about 6 kHz if one additionally considers higher order combination tones. This is corroborated by Fig. 6.2 which displays the GW spectrum for the simulation with total binary mass $M_{\rm tot} = 3.1\ M_\odot$, where we also draw the fit for the simplified analytic model (green curve). Those additional frequencies are estimated by employing the dominant frequency at early times $\langle f_{\rm peak}^{t\in[0,t_*]}\rangle$ and using the expressions $f_{2+20} \approx \langle f_{\rm peak}^{t\in[0,t_*]}\rangle + 2\cdot f_0$ and $f_{\rm spiral+20} \approx f_{\rm spiral} + 2\cdot f_0$. The respective frequency ranges are determined by inserting the time evolution of $f_0(t)$ and $f_{\rm peak}^{\rm analytic}(t)$. The estimated frequency ranges for f_{2+20} and $f_{\rm spiral+20}$ match relatively well with peaks in the GW spectrum. We note that the frequencies f_{2+20} and $f_{\rm spiral+20}$ are also expected to follow empirical relations, which can be exploited in more sophisticated analytic models.

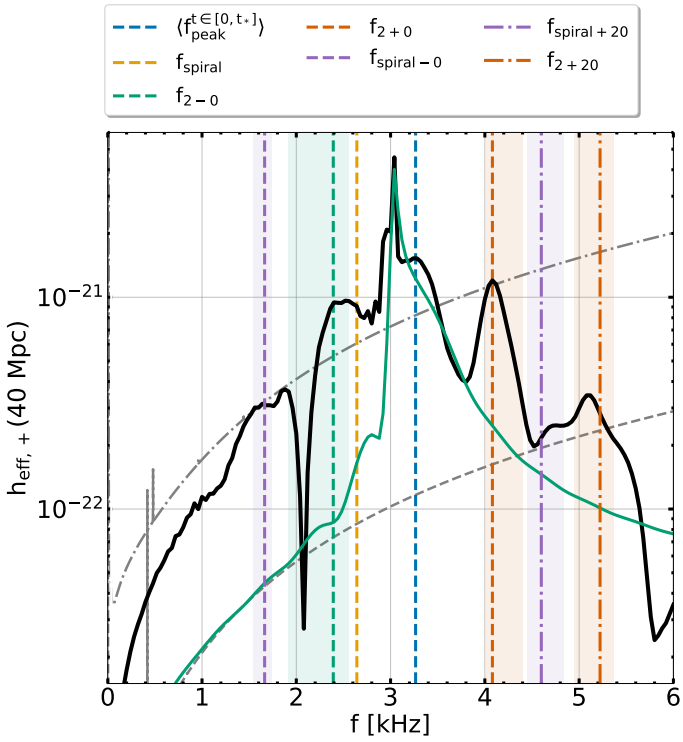

Figure 6.2: Effective GW spectra $h_{\rm eff,+}(f)$ for simulation, and simplified analytic model for $\rm M_{tot} = 3.1\ M_\odot$ model. Black line corresponds to the simulation. Green line displays the simplified 1-component analytic model (A1). Dashed, dash-dotted vertical lines indicate secondary frequencies $\langle f_{\rm peak}^{t\in[0,t_*]}\rangle$, $f_{\rm spiral}$, $f_{2\pm0}$, $f_{\rm spiral-0}$, f_{2+20}, $f_{\rm spiral+20}$. Shaded areas visualize their respective spread due to the time evolving frequencies. Figure taken from [4].

We also remark that the frequency component f_{2-20} is most likely less important than $f_{\rm spiral-0}$. We use the expression $f_{2-20} \approx \langle f_{\rm peak}^{t\in[0,t_*]}\rangle - 2\cdot f_0$ to estimate its frequency at $f_{2-20} = 1.309$ kHz, and this is significantly lower than the peak in the GW spectrum ($f_{\rm spiral-0} = 1.664$ kHz).

Another relevant feature is the re-excitation of the quadrupolar mode $f_{\rm peak}$, which occurs roughly 10 ms after merging in high-mass models, see Appendix B.2.2, possibly due to the excitation of a low-$|T/W|$ rotational instability (see, e.g. [153–155] and references therein). This feature is not captured by the adopted single exponential decay of the amplitude.

7. Quasi-radial oscillations in NS merger remnants

In this chapter we discuss the quasi-radial oscillation modes in NS merger remnants. To our knowledge, this is the first comprehensive analysis of quasi-radial oscillations in NS merger remnants. We analyse the libraries of binary NS simulations introduced in Sec. 3.2. For every remnant in our collection of simulations, we extract the quasi-radial oscillation frequency f_0 and the quadrupolar frequency $f_{\rm peak}$. We find a quasi-universal relation that connects the ratio $f_0/f_{\rm peak}$ to the proximity to the threshold mass for prompt formation of BH. Finally, we propose a method for determining the threshold mass $M_{\rm thres}$ and maximum mass $M_{\rm max}$ which relies on only one precise measurement of $M_{\rm tot}$, $f_{\rm peak}$, f_0.

7.1. The $f_0/f_{\rm peak}$ relation

In this section we introduce a new quasi-universal empirical relation which connects the quasi-radial oscillation frequency f_0, the quadrupolar oscillation frequency $f_{\rm peak}$, and the *proximity* to the threshold mass for prompt BH formation $\Delta M = M_{\rm thres} - M_{\rm tot}$ (see Fig. 7.2). In the following analysis, we only discuss symmetric binaries but our results can, in principle, be generalized for asymmetric binaries (see Sec. 7.4).

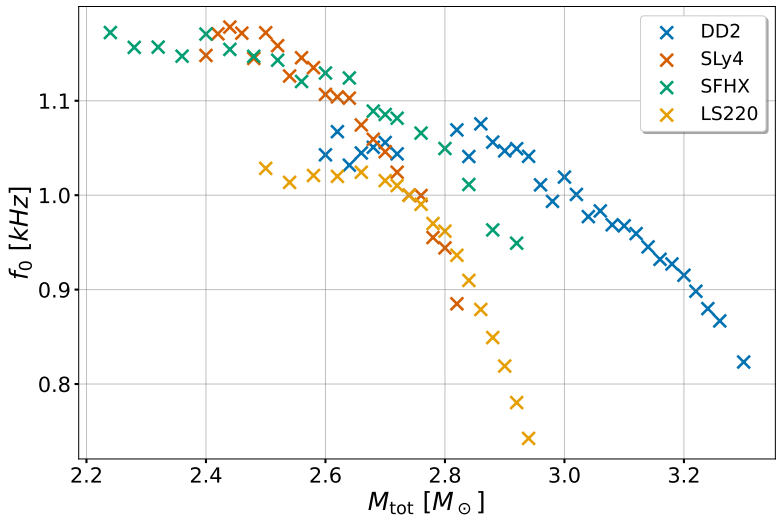

Figure 7.1: Quasi-radial oscillation frequencies f_0 for the DD2, SLy4, SFHX, and LS220 EoS models as a function of total binary mass.

For every simulation in our data set we extract the quasi-radial oscillation frequency f_0 from the Fourier transform of the time evolution of the maximum rest-mass density $\rho_{\max}(t)$ (alternatively, one may use the minimum lapse function $\alpha_{\min}(t)$ as in Chapter 4). We first detrend the data using a second order polynomial fit and employ the Tukey window function with a rolloff parameter of $s = 0.1$. We locate the peak with the maximum amplitude in the region of 1 kHz and then perform a second order polynomial fit where we finally identify f_0 as the frequency which corresponds the analytic maximum of the polynomial. We extract $f_{\rm peak}$ from the Fourier transform of the GW post-merger signals using the procedure described in Chapter 4 and we also employ the second order polynomial fit, as we do for f_0, to resolve $f_{\rm peak}$ more accurately. Furthermore, for the models where the coupling frequency f_{2-0} is adequately excited and thus can be identified in the GW spectrum, we compare the extracted frequency f_0 to the difference $f_{\rm peak} - f_{2-0} \approx f_0$ and find good agreement with the extracted f_0.

Figure 7.1 displays the frequencies f_0 as a function of total binary mass $M_{\rm tot}$ for the EoSs DD2, SLy4, SFHX, and LS220. We only present these four EoSs as an example but we note that the same conclusions can be drawn for all the EoSs in our data set. For every EoS model we simulate configurations with increasing total binary mass and only stop when $M_{\rm tot}$ is close to $M_{\rm thres}$. We find that, in contrast to $f_{\rm peak}$, the frequencies f_0 do not change drastically and generally range from approximately 0.8 kHz to 1.2 kHz.

For every EoS, we identify two trends in f_0 as the total mass $M_{\rm tot}$ increases: a) For the configurations with total mass $M_{\rm tot}$ being well below the threshold mass ($\Delta M \gtrsim 0.25\ M_\odot$), the frequencies f_0 are roughly constant and approximately around 1.0 kHz. We observe a correlation of the frequencies f_0 (in this $M_{\rm tot}$ regime) with the radius $R_{1.6}$ of the 1.6 $M_\odot$ non-rotating NS. b) For the configurations where $M_{\rm tot}$ approaches the threshold mass $M_{\rm thres}$ ($\Delta M \lesssim 0.25\ M_\odot$), the frequencies f_0 start to decrease significantly and tend to approach zero. This is a trend which is also observed in perturbative calculations [87] where the frequency of the fundamental radial oscillation mode goes to zero when the gravitational mass is close to $M_{\max}$ (for higher mass configurations the frequencies f_0 become complex and lead to unstable modes).

Furthermore, we introduce a new quasi-universal relation between the ratio $f_0/f_{\rm peak}$ and $\Delta M = M_{\rm thres} - M_{\rm tot}$, which measures the proximity to the threshold mass, shown in Fig. 7.2. As can be seen in Fig. 7.2, $f_0/f_{\rm peak}$ is an increasing function of ΔM. For all binaries in our data set, we compute the ratio $f_0/f_{\rm peak}$ and then use the total mass $M_{\rm tot}$ and the values of $M_{\rm thres}$ from [5] to determine ΔM. Figure 7.2 shows the ratios $f_0/f_{\rm peak}$ as a function of ΔM for the various EoS models employed in this work. As apparent, there is a noticeable scatter in this relation, however, all the EoS models exhibit this trend. We find that this relation can be modeled with a third order polynomial (see black curve and gray band in Fig. 7.2).

To better understand this relation, we first focus on the configurations with $M_{\rm tot}$ far from $M_{\rm thres}$ ($\Delta M \gtrsim 0.25\ M_\odot$). In this mass regime, the frequencies f_0 are roughly constant but also, depending on the softness/stiffness of the EoS, range from ≈ 0.9 kHz (stiff EoSs) to ≈ 1.2 kHz (soft EoSs). The frequencies $f_{\rm peak}$, for a

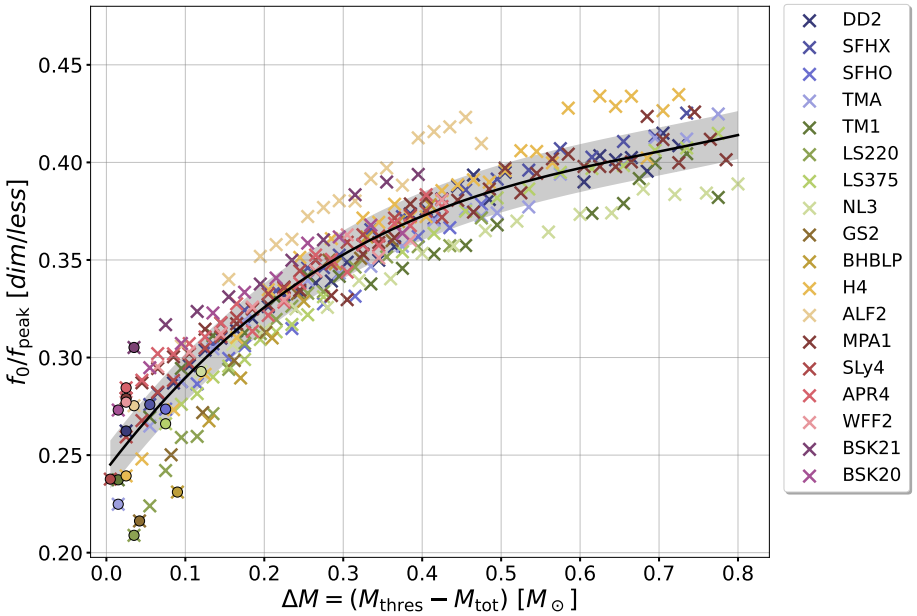

Figure 7.2: Quasi-universal relation of the ratio $f_0/f_{\rm peak}$ as a function of the proximity to the threshold mass ΔM. Black curve corresponds to the third order polynomial fit. Gray band indicates the average absolute error between the data and the fit.

fixed EoS mass sequence, increase with the total mass, however, they also exhibit a scatter in the frequency ranges. Low values of $f_{\rm peak}$ (around $2.0 - 2.4$ kHz) are attributed to stiff EoSs and high values (around $3.2 - 3.6$ kHz) to soft EoSs. By considering the ratio $f_0/f_{\rm peak}$, the EoS dependent scatter (in f_0 or $f_{\rm peak}$) due to the softness/stiffness of the EoS is cancelled out. The decreasing trend is maintained (originating from the increase of $f_{\rm peak}$ as the mass increases).

For the configurations where $M_{\rm tot}$ is close to $M_{\rm thres}$ ($\Delta M \lesssim 0.25\ M_\odot$), the frequencies f_0 decrease significantly. The frequencies $f_{\rm peak}$, again for a fixed EoS mass sequence, continue to increase at an even higher rate than previously as the total mass increases (see [156]). The combination of those effects lead to the slightly steeper trend in the $f_0/f_{\rm peak}$ relation around the vicinity of $\Delta M = 0$.

We note that the threshold masses $M_{\rm thres}$ for all these EoSs, are determined using another version of the SPH code which employs a different, more dissipative, kernel and thus some minor changes of a few percent in $M_{\rm thres}$ may affect the exact value of ΔM and possibly improve a bit the relation. We are currently performing additional simulations in this regard.

Finally, we remark that it may be observationally preferable to construct a variant of the $f_0/f_{\rm peak}$ relation where the ratio $f_0/f_{\rm peak}$ is replaced by $(f_{\rm peak} - f_{2-0})/f_{\rm peak} \approx f_0/f_{\rm peak}$ which uses quantities measured directly from the signal.

7.2. Determining M_{thres}

In this section we introduce a method for determining the threshold mass M_{thres} using the aforementioned f_0/f_{peak} relation. We consider a scenario where the total binary mass M_{tot}, the dominant frequency f_{peak}, and the quasi-radial oscillation frequency f_0 are measured with good accuracy. In practice, this means that we do not consider any uncertainties in $M_{\mathrm{tot}}, f_{\mathrm{peak}}, f_0$. The total binary mass M_{tot} can be determined by the inspiral phase, while the frequencies f_{peak} and f_0 from the post-merger phase using templates as the ones described Chapter 5. We note that the frequency f_0 has to be inferred by measuring at least one of the secondary frequencies $f_{2\pm0}$ or the doublet $f_{\mathrm{spiral}\pm0}$ and f_{spiral}. In Sec. 7.4 we discuss a generalization of our method where the total mass M_{tot} (threshold mass M_{thres}) is replaced by the chirp mass M_{chirp} (chirp threshold mass $M_{\mathrm{chirp}}^{\mathrm{thres}}$), which is the quantity measured with highest accuracy so far, but we find it more intuitive to introduce our scheme with regard to M_{tot}.

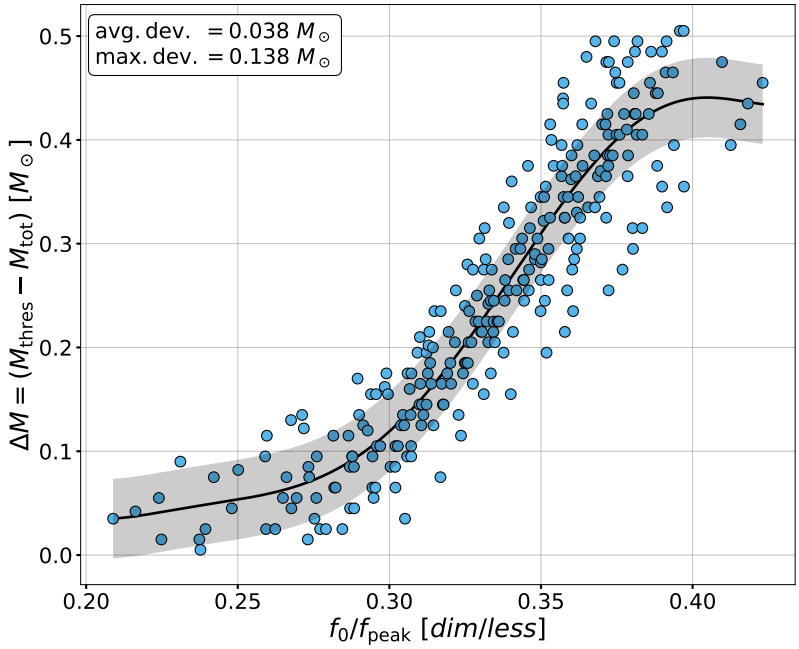

Figure 7.3: Proximity to threshold mass ΔM as a function of the ratio f_0/f_{peak} for all binaries in our data set. Black curve shows the sixth order polynomial fit. Gray band indicates the average absolute error between the data and the fit.

The f_0/f_{peak} relation can be used to determine the proximity to threshold mass $\Delta M = M_{\mathrm{thres}} - M_{\mathrm{tot}}$ (see Fig. 7.2), however, we find it more convenient to invert this relation and perform a fit on ΔM with respect to f_0/f_{peak} (see Fig. 7.3). In addition, we only consider a subset of our data set with models with proximity to threshold mass $\Delta M \leq 0.5\ M_\odot$. This choice is meaningful because models with larger ΔM are likely to have only weakly excited quasi-radial oscillations and thus a measurement of f_0 may be difficult. Moreover, our library of waveforms consists of considerably less simulations with $\Delta M > 0.5$ and so the empirical law we derive is statistically more accurate for low values of ΔM. Finally, we employ a sixth

order polynomial (and not a third order one in order to increase the accuracy) to model the general trend of the data. It reads

$$\begin{aligned}\Delta M &= +1.0463\cdot 10^5\,(\frac{f_0}{f_{\rm peak}})^6 - 1.9257\cdot 10^5\,(\frac{f_0}{f_{\rm peak}})^5 + 1.4455\cdot 10^5\,(\frac{f_0}{f_{\rm peak}})^4 \\ &- 5.6669\cdot 10^4\,(\frac{f_0}{f_{\rm peak}})^3 + 1.2257\ 10^4\cdot(\frac{f_0}{f_{\rm peak}})^2 - 1.3891\cdot 10^3\,(\frac{f_0}{f_{\rm peak}}) \\ &+ 64.572. \end{aligned} \tag{7.1}$$

We evaluate the quality of our fit with the average of the absolute deviation between the data and the empirical relation (see gray band in Fig. 7.3) and find it to be equal to 0.038 $M_\odot$. This quantity is important because it shows how well our relation describes the majority of our data and avoids the biases which come from extreme models. A rather conservative index for assessing this relation is the maximum deviation, which is equal to 0.138 $M_\odot$. The latter can be interpreted as the maximum uncertainty in our predictions. Since we consider a precise measurement in total mass $M_{\rm tot}$ and so the uncertainty in $M_{\rm tot}$ is zero, any uncertainty in the relation (7.1) becomes the uncertainty in predicting the threshold mass using the expression $M_{\rm thres} = M_{\rm tot} + \Delta M$.

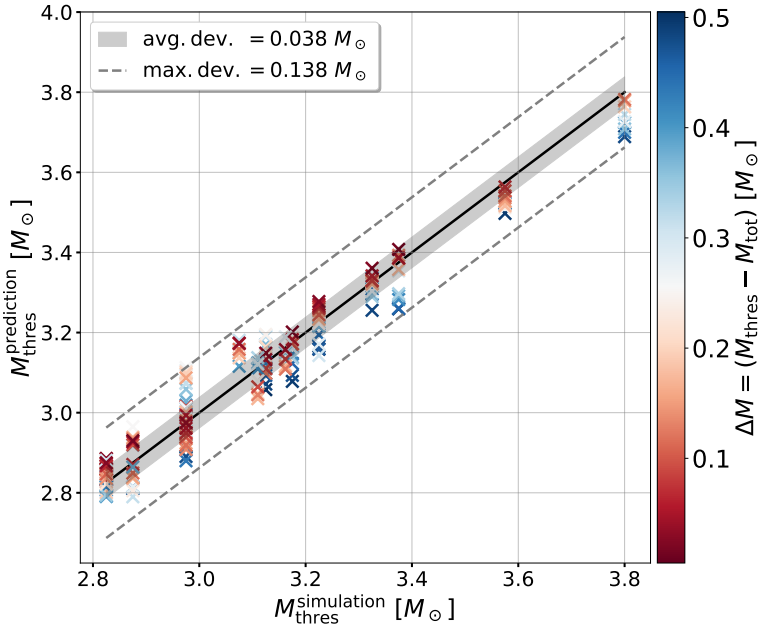

Figure 7.4: Threshold mass predictions $M_{\rm thres}^{\rm prediction}$ as a function of the numerical relativity values $M_{\rm thres}^{\rm simulation}$. Black line indicates the perfect match of $y = x$. Gray band shows the average absolute error between the predictions and the data. Gray dashed lines show the maximum deviation between the fit and the data. Color bar indicates the proximity to threshold mass ΔM.

We then convert the estimates of ΔM to $M_{\rm thres}$. We treat every model in our sample as a potential detection where $M_{\rm tot}$, $f_{\rm peak}$, and f_0 are known with zero uncertainties. From the ratio $f_0/f_{\rm peak}$ and the empirical relation (7.1) we obtain

the proximity to threshold mass ΔM and then predict the threshold mass using the expression $M_{\rm thres} = M_{\rm tot} + \Delta M$. Figure. 7.4 shows the comparison between our predictions ($M_{\rm thres}^{\rm prediction}$) and the numerical relativity values ($M_{\rm thres}^{\rm simulation}$) calculated in [5], where the colors indicate the proximity to threshold mass ΔM. The predictions agree relatively well with the numerical relativity calculations with an average deviation of 0.038 $M_\odot$. The latter is identical to the average deviation on ΔM, which is expected as previously explained. The aforementioned apply to the maximum deviation which is equal to 0.138 $M_\odot$.

Table 7.1 provides information about the scheme's predictions $M_{\rm thres}^{\rm prediction}$ for all EoS models of our sample. We find that the ΔM which results to the lowest deviation from the simulation value, that is, our *best prediction* (BP), is not necessarily the one with the smallest ΔM for the respective EoS (see Tab. 7.1). This may be explained in the following manner: The accuracy of the method increases when the pair $(f_0/f_{\rm peak}, \Delta M)$ coincides with (or is close to) the empirical law Eq. (7.1). For a fixed EoS mass sequence, the scatter of the points $(f_0/f_{\rm peak}, \Delta M)$ compared to Eq. (7.1) is not necessarily a monotonic function of ΔM, and thus it may be that intermediate values of ΔM are closer to Eq. (7.1) than lower/higher values of ΔM. In practice, binaries with $(f_0/f_{\rm peak}, \Delta M)$ being outside of the gray band in Fig. 7.3 underestimate or overestimate $M_{\rm thres}$ with an error larger than 0.038 $M_\odot$, and this can occur at different ΔM regimes for the different EoS models.

EoS	$M_{\rm thres}^{\rm simulation}$ $[M_\odot]$	$M_{\rm thres}^{\rm BP}$ $[M_\odot]$	$M_{\rm thres}^{\rm MD}$ $[M_\odot]$	$\Delta M^{\rm BP}$ $[M_\odot]$	$\Delta M^{\rm MD}$ $[M_\odot]$
DD2	3.325	3.325	3.256	0.305	0.485
SFHX	2.975	2.972	2.913	0.095	0.495
SFHO	2.875	2.871	2.790	0.075	0.315
TMA	3.175	3.172	3.078	0.095	0.495
TM1	3.375	3.385	3.259	0.215	0.495
LS220	2.975	2.975	2.880	0.035	0.435
LS375	3.575	3.563	3.497	0.075	0.495
NL3	3.800	3.782	3.689	0.120	0.480
GS2	3.162	3.157	3.109	0.042	0.122
BHBLP	3.110	3.109	3.035	0.410	0.170
H4	3.125	3.125	3.195	0.425	0.245
ALF2	2.975	2.976	3.113	0.435	0.255
MPA1	3.225	3.226	3.143	0.345	0.305
SLy4	2.825	2.820	2.870	0.405	0.265
APR4	2.825	2.821	2.886	0.345	0.025
WFF2	2.825	2.822	2.881	0.225	0.305
BSK21	3.075	3.116	3.181	0.395	0.315
BSK20	2.875	2.864	2.965	0.375	0.255

Table 7.1: $M_{\rm thres}$ determined from numerical relativity, best predictions of the threshold mass $M_{\rm thres}^{\rm BP}$, predictions which lead to the maximum deviation to the numerical relativity threshold mass $M_{\rm thres}^{\rm MD}$, and the corresponding proximity to threshold mass ΔM, for all the EoSs in our data set.

We also provide the threshold mass estimate which deviates the most from the actual value of $M_{\rm thres}$, that is our *maximum deviation* (MD) estimate, and its corresponding ΔM. From the configurations where the predictions of $M_{\rm thres}$ deviate from the numerical relativity value by less than the average deviation (gray band) we find an average ΔM approximately equal to 0.24 $M_\odot$. This quantity gives only a rough estimate for the optimal ΔM where the method can produce good performance. Generally, the scheme performs well for the majority of the EoSs with the exception being the BSK21 EoS where the best prediction has an absolute difference of 0.053 $M_\odot$ (see Tab. 7.1).

7.3. Constraints on $M_{\rm max}$

Furthermore, we introduce a method to convert the predictions of $M_{\rm thres}$ to predictions on the maximum mass $M_{\rm max}$ for a non-rotating NS. As previously, we assume one detection where a precise measurement of $M_{\rm tot}$, $f_{\rm peak}$, and f_0 occurs. We then use the $f_0/f_{\rm peak}$ relation and $M_{\rm tot}$ to determine the threshold mass $M_{\rm thres}$ with an average error of 0.038 $M_\odot$(see Sec. 7.2). Subsequently, we determine $R_{1.6}$ from $f_{\rm peak}$ and $M_{\rm tot}$ using empirical relations like those in [49]. Finally, we utilize the bi-linear relations introduced in [5] to determine $M_{\rm max}$ using $M_{\rm thres}$ and $R_{1.6}$.

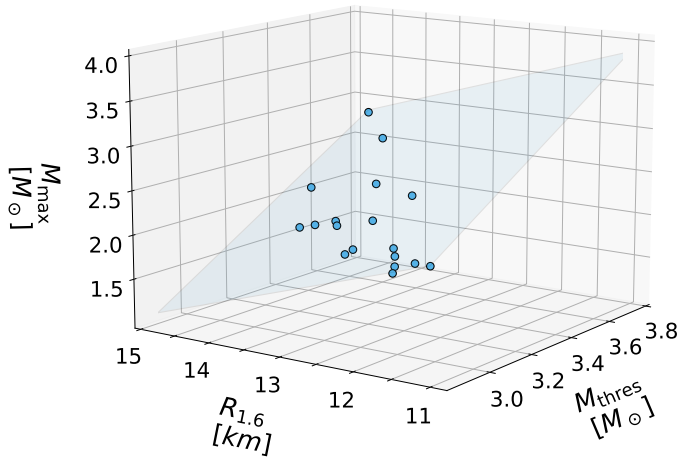

Figure 7.5: Bi-linear relation for the maximum mass $M_{\rm max}$ as a function of the threshold mass $M_{\rm thres}$ and $R_{1.6}$. Blue points correspond to the values of $M_{\rm max}$ and $R_{1.6}$ for the EoSs considered in this work.

More specifically, a precise measurement of $f_{\rm peak}$ can be used to determine $R_{1.6}$. To achieve this one may employ the empirical relations introduced in [49] which connect $R_{1.6}$ to $f_{\rm peak}$ and chirp mass $M_{\rm chirp}$[1]. The authors provide different versions of these fits for only symmetric and general ratio binaries with a 1σ

[1]Because we assume a precise measurement of the total mass $M_{\rm tot}$, the chirp mass $M_{\rm chirp}$ would be also measured accurately since $M_{\rm tot}$ is inferred from $M_{\rm chirp}$ (see Sec. 7.4 for an extension of our method).

standard deviation of 0.108 km and 0.117 km, respectively. Alternatively, one may invert the empirical relation of $f_{\rm peak}$ as a function of $R_{1.6}$ introduced in [48], which exhibits an average deviation of $\approx$ 35 meters. This relation is computed for a fixed total binary mass of $M_{\rm tot} = 2.7\ M_\odot$, however once $M_{\rm tot}$ is known, new empirical relations for $R_{1.6}(f_{\rm peak}(M_{\rm tot}))$ can be constructed with possibly slightly different average deviations.

Finally, we use bi-linear empirical relations from [5] to predict $M_{\rm max}$. The authors provide the bi-linear relations for $M_{\rm thres}(M_{\rm max}, R_{1.6})$ (for different EoS subsets and mass ratios), which can be trivially converted to $M_{\rm max}(M_{\rm thres}, R_{1.6})$ and thus predict the maximum mass $M_{\rm max}$ for various EoS models. The bi-linear relation reads

$$M_{\rm max} \;=\; \tilde{A}\cdot M_{\rm thres} + \tilde{B}\cdot R_{1.6} + \tilde{C} \tag{7.2}$$

where the coefficients $\tilde{A}, \tilde{B}, \tilde{C}$ are derived from A, B, C of the $M_{\rm thres}(M_{\rm max}, R_{1.6})$ relation (no. 14) in Tab. I in [5] via the relations $\tilde{A} = +\frac{1}{A}$, $\tilde{B} = -\frac{B}{A}$, $\tilde{C} = -\frac{C}{A}$.

Figure 7.5 displays the maximum masses $M_{\rm max}$ for all the EoS models considered in this data set overplotted on the bi-linear relation Eq. (7.2). As apparent, the data fit very well the bi-linear relation with an average deviation of 0.0344 $M_\odot$.

Our method can be summarized in the following three steps:

1) $R_{1.6}$ is inferred from $f_{\rm peak}$ and $M_{\rm tot}$ using the relations of [49].

2) $M_{\rm thres}$ is inferred from $M_{\rm tot}, f_{\rm peak}, f_0$ with the method described in Sec. 7.2

3) $M_{\rm max}$ is inferred using the bi-linear relation $M_{\rm max}(M_{\rm thres}, R_{1.6})$ introduced in [5].

We estimate the uncertainty in the prediction of $M_{\rm max}$ in step 3) by propagation of the error in steps 1) and 2). Since we consider precisely measured $M_{\rm tot}, f_{\rm peak}, f_0$, which is a reasonable assumption for future generation detectors, we only propagate the uncertainty in measuring $M_{\rm thres}$ ($\hat{s}_{\rm M_{thres}}$) and $R_{1.6}$ ($\hat{s}_{\rm R_{1.6}}$). The expected uncertainty in $M_{\rm max}$ ($\hat{s}_{\rm M_{max}}$) in Eq. (7.2) is obtained from the expression

$$\begin{aligned}\hat{s}_{\rm M_{max}} &= \sqrt{\left(\frac{\partial M_{\rm max}}{\partial M_{\rm thres}}\right)^2 \hat{s}^2_{\rm M_{thres}} + \left(\frac{\partial M_{\rm max}}{\partial R_{1.6}}\right)^2 \hat{s}^2_{\rm R_{1.6}}} \\ &= \sqrt{\tilde{A}^2\ \hat{s}^2_{\rm M_{thres}} + \tilde{B}^2\ \hat{s}^2_{\rm R_{1.6}}}\end{aligned} \tag{7.3}$$

We obtain $\hat{s}_{\rm M_{thres}}$, $\hat{s}_{\rm R_{1.6}}$ from the average deviation between the empirical relations and the respective data used for the fits (see Sect. 7.2 and [49]). These correspond to $\hat{s}_{\rm M_{thres}} \approx 0.038\ M_\odot$ and $\hat{s}_{\rm R_{1.6}} = 0.108$ km (for the relation of the symmetric binaries in [49]). Finally, we estimate the uncertainty in $M_{\rm max}$ to be $\hat{s}_{\rm M_{max}} = 0.0725\ M_\odot$. For zero uncertainty in $R_{1.6}$ we obtain $\hat{s}_{\rm M_{max}} = 0.066\ M_\odot$.

As previously done, we treat each simulation as a mock detection where $M_{\rm tot}$ ($M_{\rm chirp}$), $f_{\rm peak}, f_0$ are precisely known, and then use the steps 1) to 3) to estimate $M_{\rm max}$. As is apparent, the accuracy of our method depends on how good our predictions for $R_{1.6}$ and $M_{\rm thres}$ are in steps 1) and 2). We have already discussed

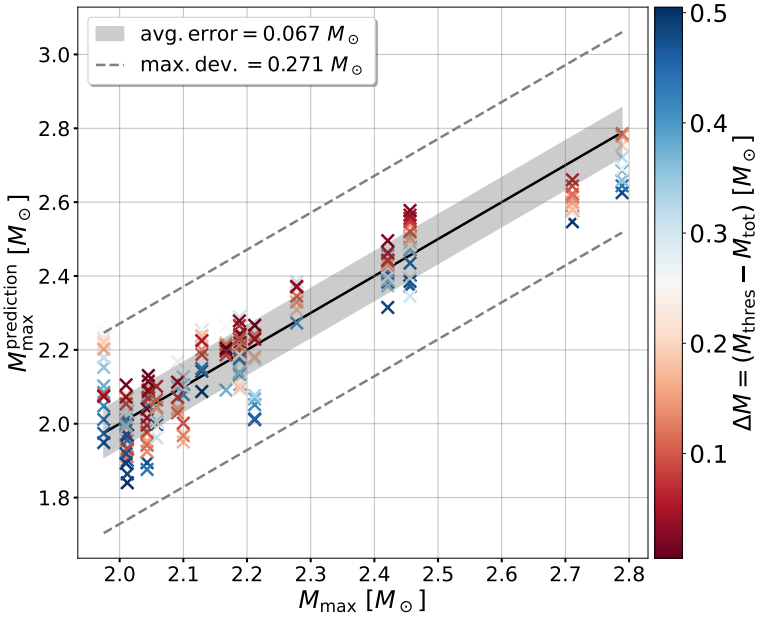

Figure 7.6: Maximum mass predictions $M_{\rm max}^{\rm prediction}$ as a function of $M_{\rm max}$ derived from the EoSs. Black line indicates the perfect match of $y = x$. Gray band shows the average absolute error between the predictions and the data. Gray dashed lines show the maximum deviation between the fit and the data. Color bar indicates the proximity to threshold mass ΔM.

the uncertainties in $M_{\rm thres}$ from the $f_0/f_{\rm peak}$ relation, however, for the uncertainty in $R_{1.6}$ we rely on the reported values in [49]. We test the empirical relation of [49] on our data set and find an average deviation of ≈ 219 meters (instead of 108 meters). One explanation may be that the data set employed in [49] includes 118 waveforms in total, while our data set (configurations with $\Delta M < 0.5\ M_\odot$) is more than two times larger with a total of 270 waveforms. Another reason may be that we focus on configurations with $M_{\rm tot}$ close to $M_{\rm thres}$ and therefore we may deviate from the total mass parameter space used in [49]. For these reasons, we consider the scenario where $R_{1.6}$ is determined with an ideal empirical relation of $f_{\rm peak}$ and $M_{\rm tot}$, and is equal to the value of $R_{1.6}$ obtained directly from the EoS. This test allows us to decouple the errors between the predictions in $M_{\rm thres}$ and $R_{1.6}$, and evaluate the performance of our new method which utilizes the knowledge of $f_0/f_{\rm peak}$.

Figure. 7.6 displays the $M_{\rm max}$ predictions ($M_{\rm max}^{\rm prediction}$) for all the simulations of our data set ($\Delta M \lesssim 0.5\ M_\odot$) in comparison to the values of $M_{\rm max}$ obtained directly from the EoS model. The black line shows the ideal match ($y = x$), while the colors indicate the proximity to threshold mass ΔM. We find an average deviation between the predictions and the $M_{\rm max}$ values obtained from the EoS of $0.067\ M_\odot$. This is not surprising as it is almost equal to the value computed from the error propagation with zero uncertainty in $R_{1.6}$. The maximum deviation is $0.271\ M_\odot$, which is a rather large value, but as can be seen from Fig. 7.6 it is mostly due to two EoS model outliers.

So far, we assumed perfect knowledge of $R_{1.6}$ which may not be the case in a

EoS	$M_{\rm max}$ $[M_\odot]$	$M_{\rm max}^{\rm BP}$ $[M_\odot]$	$M_{\rm max}^{\rm MD}$ $[M_\odot]$	$\Delta M^{\rm BP}$ $[M_\odot]$	$\Delta M^{\rm MD}$ $[M_\odot]$
DD2	2.421	2.419	2.315	0.425	0.485
SFHX	2.129	2.142	2.258	0.455	0.255
SFHO	2.058	2.064	1.963	0.115	0.315
TMA	2.010	2.010	1.893	0.415	0.495
TM1	2.212	2.228	2.011	0.215	0.495
LS220	2.043	2.040	1.876	0.035	0.435
LS375	2.711	2.661	2.547	0.075	0.495
NL3	2.789	2.786	2.626	0.120	0.480
GS2	2.091	2.100	2.168	0.362	0.282
BHBLP	2.100	2.099	1.951	0.290	0.170
H4	2.012	2.022	1.840	0.345	0.505
ALF2	1.975	1.974	2.246	0.455	0.255
MPA1	2.456	2.471	2.577	0.425	0.025
SLy4	2.045	2.049	2.134	0.405	0.265
APR4	2.189	2.191	2.095	0.145	0.185
WFF2	2.188	2.187	2.289	0.225	0.305
BSK21	2.278	2.273	2.384	0.395	0.315
BSK20	2.167	2.185	2.265	0.335	0.255

Table 7.2: $M_{\rm max}$ derived from the EoSs, best predictions of the maximum mass $M_{\rm max}^{\rm BP}$, predictions which lead to the maximum deviation to the maximum mass $M_{\rm max}^{\rm MD}$, and the corresponding proximity to threshold mass ΔM, for all the EoSs in our data set.

detection scenario. In addition, as we mentioned previously, using relations from other works and different data sets may introduce systematic uncertainties in $R_{1.6}$ which would propagate to predictions in $M_{\rm max}$. For these reasons, we perform an additional test in order to evaluate the impact of the error in $R_{1.6}$ but also keep the uncertainties under control. For every mock detection in our data set we add a noise to the values of $R_{1.6}$ such that $R_{1.6} \to R_{1.6} + \delta R_{1.6}$ and then calculate the predictions in $M_{\rm max}$. $\delta R_{1.6}$ is drawn from a uniform distribution $\mathcal{U}[-\Delta R, +\Delta R]$ where $-\Delta R$ and $+\Delta R$ are the lower and upper limits, respectively. We consider three noise realizations, $\mathcal{U}[-100\text{ m}, +100\text{ m}]$, $\mathcal{U}[-200\text{ m}, +200\text{ m}]$, and the extreme case of $\mathcal{U}[-400\text{ m}, +400\text{ m}]$. We find average deviations of 0.067 $M_\odot$, 0.071 $M_\odot$, and 0.0857 $M_\odot$ and maximum deviations of 0.265 $M_\odot$, 0.288 $M_\odot$, 0.316 $M_\odot$ for the three cases ($\Delta R = 100, 200, 400$ m), respectively. Interestingly, the difference in the average deviations is negligible for the first two cases, even though the noise distributions differ significantly. In the third, extreme, case, the average scatter is larger than the others, however, it is still relatively small. It may be that the additional scatter in $R_{1.6}$ is compensated by the scatter in $M_{\rm thres}$ and thus the final prediction of $M_{\rm max}$ is only mildly affected. The maximum deviations are systematically increasing but this is expected due to the larger noise and the fact that is dictated by only one data point.

7.4. Extensions

In this section we introduce two extensions to our method. First, we illustrate how a generalization of the $f_0/f_{\rm peak}$ relation to different mass ratios is possible. Then we discuss a variation of the $f_0/f_{\rm peak}$ relation where the proximity to the threshold mass ΔM is replaced by the proximity to the threshold chirp mass ($M_{\rm chirp}^{\rm thres}$) defined as $\Delta M_{\rm chirp} = M_{\rm chirp}^{\rm thres} - M_{\rm chirp}$.

7.4.1. Asymmetric binaries

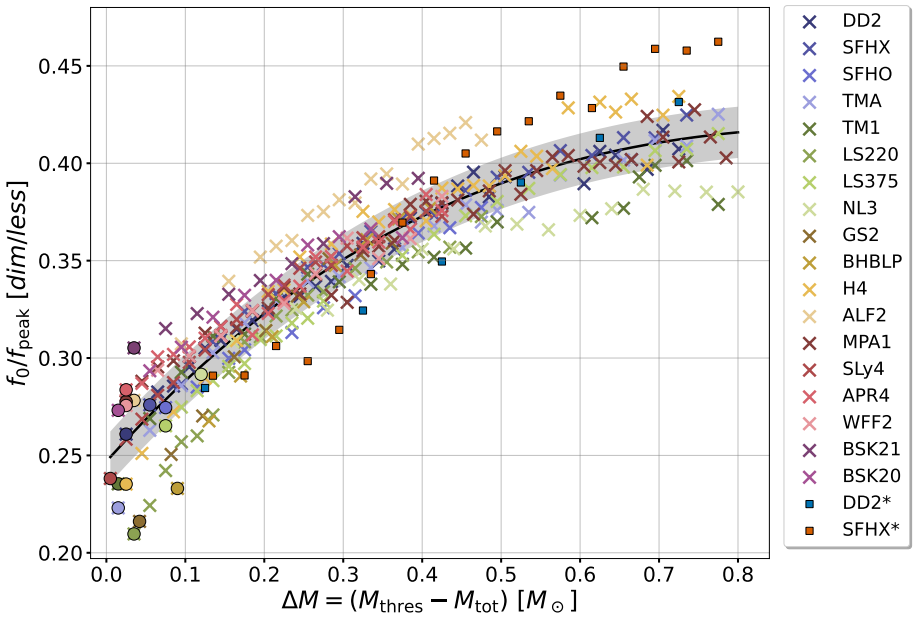

Figure 7.7: Quasi-universal $f_0/f_{\rm peak}$ relation for the extended data set which includes asymmetric binaries of $q = 0.9$. Black curve corresponds to the third order polynomial fit. Gray band indicates the average absolute error between the data and the fit.

We extend our analysis on the $f_0/f_{\rm peak}$ relation and include configurations from the data set described in Sec. 3.2.2. We consider the mass sequences with the DD2 and SFHX EoS models and a binary mass ratio of $q = 0.9$. We note that the SFHX and DD2 sequences consist of 17 and 6 simulations (for $\Delta M \leq 0.8\ M_\odot$), respectively. We will refer to these asymmetric sequences with the name of the EoS along with a star symbol as DD2* and SFHX*. We note that we do not include the mass sequence for the SLy4 EoS and $q = 0.9$ in this analysis. This is because for a portion of those models the quasi-radial mode is only weakly excited, and identifying f_0 is not trivial. Similarly, we do not include the sequences with lower values of q because as the asymmetry grows, the radial oscillation becomes weaker, additional spectral features may emerge, and thus it is not straightforward to identify f_0 just from the Fourier transform of $\rho_{\rm max}(t)$ but an eigenmode analysis is required (see [27]). We remark that while this section serves as an example on

how the method can be extended, it is not a detailed and systematic study of the impact of binary mass and mass ratio on f_0 and its amplitude. We plan to conduct a comprehensive study of these concepts in future work.

We compute the frequencies f_0 and $f_{\rm peak}$ as previously described. Figure 7.7 displays the ratios $f_0/f_{\rm peak}$ as a function of ΔM for the extended data set. As is evident, the asymmetric binary sequences DD2* and SFHX* are in agreement with the quasi-universal $f_0/f_{\rm peak}$ relation. There is a noticeable scatter for a portion of the SFHX* models, however, the general trend is the same. The general agreement is not unexpected because, at least qualitatively, the quantities $f_{\rm peak}$, $M_{\rm thres}$, and f_0 do not change significantly as the ratio q changes (even though the amplitude of the f_0 oscillation is clearly affected by it). Nevertheless, a quantitative comparison between f_0 and $f_{\rm peak}$ for different mass ratios is not yet carried out (see [5] for a systematic study of the impact of q to $M_{\rm thres}$). All of the above suggest that an $f_0/f_{\rm peak}$ relation for all different mass ratios may exist. However, it may also be that multiple $f_0/f_{\rm peak}$ relations can be constructed for different mass ratios q (or mass ratio ranges), leading to more tight relations than in the case of a general q.

7.4.2. Chirp-mass parametrization

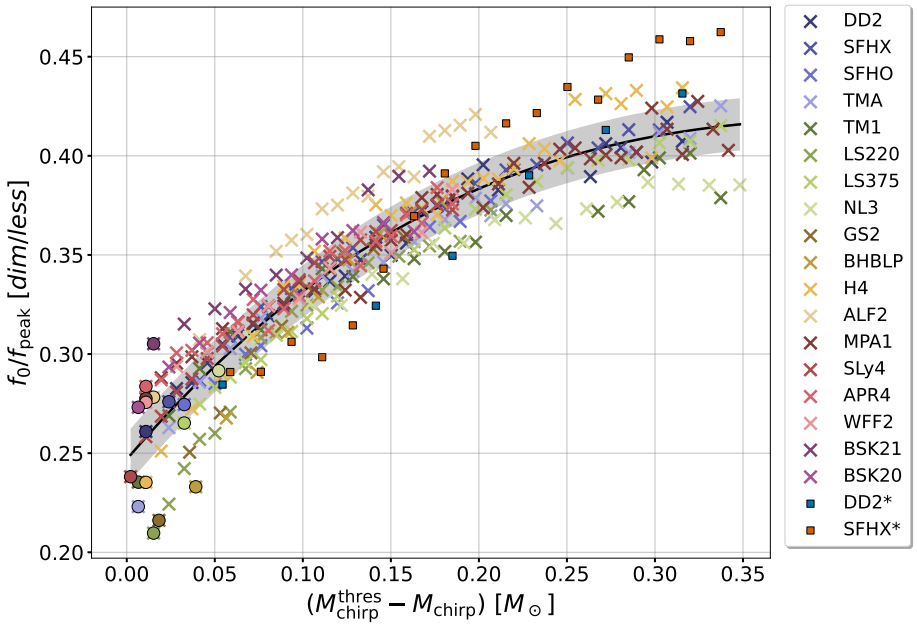

Figure 7.8: Modified quasi-universal relation of $f_0/f_{\rm peak}$ as a function of the proximity to threshold chirp mass $\Delta M_{\rm chirp}$ for the extended data set. Black curve corresponds to the third order polynomial fit. Gray band indicates the average absolute error between the data and the fit.

We discuss a variant parametrization for the $f_0/f_{\rm peak}$ relation which is a function of proximity to the threshold chirp mass ($M^{\rm thres}_{\rm chirp}$) defined as $\Delta M_{\rm chirp} = M^{\rm thres}_{\rm chirp} - M_{\rm chirp}$. This one may be preferable since the chirp mass $M_{\rm chirp}$ is the quantity measured directly from the inspiral signal and so for asymmetric bina-

ries we only need this one instead of $M_{\rm tot}$ and q (which may be determined less accurately). We consider the extended data set described in Sec. 7.4.1 which consider symmetric and asymmetric binaries. For every EoS model we convert the threshold mass $M_{\rm thres}$ to a chirp mass by assuming a binary with total mass equal to $M_{\rm thres}$ and mass ratio q. Figure 7.8 displays the modified $f_0/f_{\rm peak}$ relation parametrized with respect to $\Delta M_{\rm chirp}$. The general trend still holds, and thus this variant may be used to determine the threshold chirp mass $M_{\rm chirp}^{\rm thres}$. Nevertheless, the previous analysis has to be repeated for this relation in order to quantitatively compare the two parametrizations.

8. Conclusions

The goal of this thesis project was to investigate the GW spectral features of NS merger remnants using 3-dimensional simulations in numerical relativity. To this end, we employed two different codes (the Einstein Toolkit and an SPH code) to perform several simulations where the total binary mass $M_{\rm tot}$, the EoS model, and the binary mass ratio are varied.

In the first project of this work, we used the fully general relativistic Einstein Toolkit code to simulate a sequence of models with increasing total binary mass for an EoS model compatible with current observational constraints. We investigated the spectral properties of the GW emission of NS merger remnants and developed an accurate analytic model for the post-merger GW emission, which employs exponentially decaying sinusoids. The main findings of this project were published in [4].

We discussed the GW spectral features and their dependence on total binary mass. Furthermore, we investigated the time evolution of certain frequency components using spectrograms. We found that the dominant frequency component ($f_{\rm peak}$) in the GW spectrum exhibits a time evolution which can be described by an analytic 2-segment piecewise function. For high-mass configurations, we identified a new mechanism which explains a low frequency peak (in the GW spectra), caused by a coupling between the antipodal bulges ($f_{\rm spiral}$) and the quasi-radial mode (f_0). Our analytic model incorporates a time-dependent $f_{\rm peak}(t)$ and three secondary components. The model's performance is assessed using the noise-weighted fitting factor FF where we found good agreement with the simulations with FF > 0.95 for the majority of the models. We found that accurate post-merger GW templates (with large FFs) should incorporate at least two secondary components ($f_{\rm spiral}$, f_{2-0}) by considering simplified analytic models with fewer frequency components and comparing their fitting factors. In addition, we explored the dependencies of the analytic model's parameters, and correlations among them, on the total binary mass. These are important because they may constrain the corresponding parameter space. Finally, potential modifications to the analytic model for the configurations with $M_{\rm tot}$ close to $M_{\rm thres}$ were explored.

Our model's high FFs are comparable to, and in some cases even higher than, those of the best-performing fits reported in [64, 65, 68, 70]. They are also (along with those of [68]) higher than the average FFs reported in [64,65,70]. However, in most of those studies, a relatively large sample of binary simulations with varied EoS models is employed, which may decrease their overall performance. In this work, we first focus on understanding the underlying physical mechanisms, and different combination tones, which produce the various GW spectral features, and only then describe them with our model.

We provided an in-depth analysis of the dependence of the spectral properties of the remnants on the total binary mass and presented an analytic model with a clear physical interpretation which describes accurately the GW emission. We showed that subdominant frequency components are essential for the construction of faithful GW templates. This is a first step in the direction of constructing a complete general purpose template which depends on the binary mass, the binary mass ratio, and the EoS model. These GW templates are necessary for the detections and parameter estimation, and thus the extraction of the binary properties, in the upcoming searches with the upgraded second-generation detectors aLIGO+, aVirgo+, with future, third-generation detectors such as Einstein Telescope, Cosmic Explorer. The difference between our model and those presented in the literature, is that we focused on understanding the underlying mechanisms which produce these features (couplings, combination tones, frequency evolution), and their dependence on total binary mass.

More specifically, the models of the mass sequence exhibit a time-dependent $f_{\rm peak}(t)$ which is expressed as an one-sided frequency peak in the GW spectrum. We modeled this evolution with a 2-segment piecewise function (see Eq. (4.1)) and reproduced the one-sided structure remarkably well using the analytic model. We have shown (see also [68]) that, at least for some EoS models, the inclusion of a time-dependent treatment for the quadrupolar frequency $f_{\rm peak}$ improves significantly the ability to accurately model the waveform (large FFs). In addition, we found that as the total binary mass increases, the secondary components $f_{2\pm0}$ become more pronounced and there is an overlap between f_{2-0} and $f_{\rm spiral}$ (in agreement with the classification scheme introduced in [28]). We evaluated the significance of various subdominant features in the GW spectrum using simplified analytic models with fewer frequency components. We found systematic dependencies for all the analytic model's parameters with respect to the total binary mass, which can be modeled using second order polynomials. We also discovered tight correlations between the initial phases of the secondary components and the initial phase of the quadrupolar mode, which may suggest a constant phase difference between the $f_{\rm peak}$ and secondary components. These results are important because they provide a detailed description of the evolution of the various spectral features at different masses, and thus have to be taken into account in the GW data analysis since they can constrain the parameter space and reduce the computational cost in future detections.

In our analysis, we introduce a hierarchical procedure to determine analytic model's parameters based on curve fitting procedures. Although our scheme is relatively fast and computationally efficient, it is rather complex and requires several not-fully automated steps in order to obtain the optimal fit. Ideally, one may employ an alternative, maybe computationally more expensive, approach which guarantees that the optimal parameters are determined in a more robust manner. We plan to explore more sophisticated and robust parameter estimation techniques, such as the Bilby Bayesian inference library [157], which also generate distributions in the parameter space. These provide further information about the model's parameters and thus allow us to better understand the underlying correlations between those.

In future work, we plan to evaluate the model's performance on a large sample of EoS models and for asymmetric NS mergers. For instance, we first aim to simulate sequences of models with different binary mass ratios for the same EoS model. This way, we can examine the impact of the mass ratio q on the different secondary components. For instance, it is expected that the quasi-radial oscillation mode is only weakly excited when the binary becomes more asymmetric because the low mass star is disrupted at lower orbital frequencies. In this case, it may be that the secondary components $f_{2\pm0}$ become less relevant as the asymmetry of the system grows. In addition, the question of whether the tidal bulges are formed in asymmetric binaries is still not addressed. If the contribution of these components is only weak, simplified GW templates with fewer parameters may be proposed for asymmetric binaries. Finally, we plan to explore the dependence of the analytic model's parameters on the EoS model. For instance, it may be that specific parameters, such as the amplitude of the quadrupolar mode, exhibit different trends for the various EoS models which can then be used for constraining the EoS model.

In the second project of this work, we have built one of the largest data sets of binary NS merger simulations created so far, using the SPH code for a wide range of binary masses, ratios, and EoS models. With this data set, we studied the quasi-radial oscillation modes f_0 in NS merger remnants. These are responsible, through different coupling mechanisms, for several secondary components in the GW spectrum and thus can potentially be measured in future detections. We introduced a scheme for determining the threshold mass $M_{\rm thres}$ and maximum mass $M_{\rm max}$ of a NS which relies on only one accurate measurement of $M_{\rm tot}, f_0, f_{\rm peak}$.

More specifically, from symmetric NS merger simulations, we extracted the quasi-radial frequency f_0 for several sequences of increasing mass for different EoSs. We developed a method for the prediction of the threshold mass $M_{\rm thres}$ and the maximum mass $M_{\rm max}$, which employs a quasi-universal relation between $f_0/f_{\rm peak}$ and the proximity to threshold mass $\Delta M = M_{\rm thres} - M_{\rm tot}$, and relies on one detection of the inspiral and post-merger signal. Our method requires a precise measurement of $M_{\rm tot}, f_{\rm peak}$ and f_0, where f_0 is derived from the secondary components of the GW post-merger spectrum. With these measurements, the quasi-universal relation is employed and the proximity to threshold mass is estimated and subsequently converted to a measurement of $M_{\rm thres}$. The scheme performs well with predictions of $M_{\rm thres}$ that deviate from the numerical relativity values with an error of 0.040 $M_\odot$. Subsequently, the measurement of $M_{\rm thres}$ is converted to a prediction for the maximum mass $M_{\rm max}$ of a NS using bi-linear empirical relations between $M_{\rm thres}$, $M_{\rm max}$ and $R_{1.6}$ (introduced in [5]). The radius $R_{1.6}$ can be estimated from empirical laws which connect $M_{\rm tot}, f_{\rm peak}$ with $R_{1.6}$. This method exhibits an average deviation between the predictions of $M_{\rm max}$ and the values directly obtained from the EoS of 0.068 $M_\odot$. Using the measurements of $M_{\rm thres}$ and $M_{\rm max}$, we can thus probe the properties of high-density matter. Finally, we showed that this method is also applicable for mildly asymmetric sequences of binaries with $q = 0.9$ using additional sequences with two other EoS models.

Our proposed method showed that further constraints on the EoS can be derived by extracting the complete information contained in the GW post-merger

signal. Interestingly, this method gives an estimate for $M_{\rm thres}$ (and thus $M_{\rm max}$) from configurations which are not necessarily close to $M_{\rm thres}$ ($\Delta M \lesssim 0.5\ M_\odot$). This direction of research is important because, assuming that a sufficient sensitivity is achieved in future-generation detectors and the post-merger phase can be measured for a source with similar properties as GW170817, it is imperative to have the tools to extract all the information about the EoS contained in the post-merger GW signal.

We also note that a subset of the binary NS merger simulations is currently used by external collaborators for the development of a hierarchical Bayesian model for deriving constraints on the incompletely known EoS using an ensemble analysis of barely-informative, marginal detections of the NS merger GW post-merger signal.

Finally, we note that our large data set of binary NS mergers provides plenty of possibilities for future work. For example, we plan to assess the capabilities of our analytic model on a large set of binary waveforms with different EoS models and binary mass ratios. The large size of this data set allows us to construct accurate empirical relations for the frequencies of the different oscillation modes and combination tones and potentially develop a GW post-merger template which describes a large range of $M_{\rm tot}$, q, and EoS models. Furthermore, we plan to further explore the effect of the binary mass ratio q on the frequencies $f_{\rm peak}$, $f_{\rm spiral}$ and f_0. Another direction of future work may be the systematic study of the dynamical ejecta produced during the merger phase, which play an important role in the kilonova EM emission. We note that even though the dynamical ejecta in NS mergers have already been thoroughly investigated in the literature, our data set provides a fine sampling of the $M_{\rm tot}, q$ parameter space which may provide new information.

A. Numerical setup

In this chapter we further discuss the numerical setup for simulations described in Sec. 3.1. We investigate the impact of residual eccentricity in the ID, initial orbital separation, numerical resolution, and pi-symmetry on the spectral features.

A.1. Effect of residual eccentricity in ID and of initial orbital separation

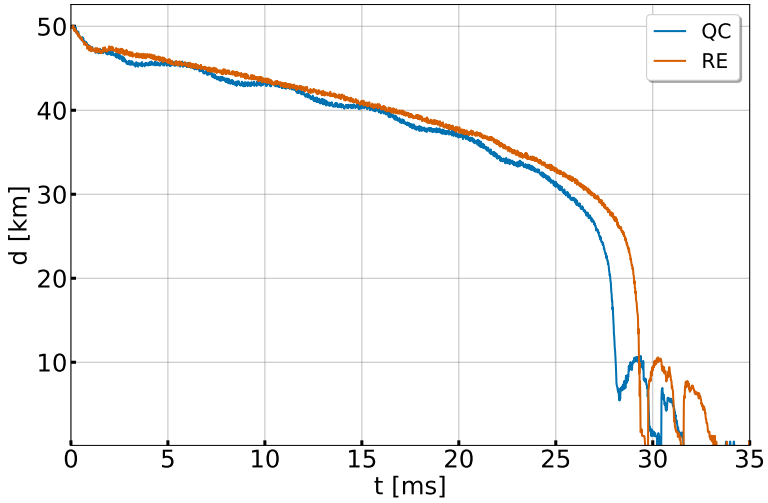

Figure A.1: Time evolution of the coordinate separation distance $d(t)$ for the simulations QC (blue) and RE (orange). Figure taken from [4].

We investigate the effect of the residual eccentricity in the ID to the spectral features. We reduce the residual eccentricity in the ID using the method described in Sec. 2.5. We perform two additional simulations with total binary mass $M_{\rm tot} = 2.5\ M_\odot$ (as in the reference simulation) and initial separation distance of $d = 50$ km. In order to reduce the eccentricity we employ the aforementioned iterative procedure (see Sec. 2.5 and [118]), which uses a few revolutions during the inspiral. It performs better at large initial separation, e.g. $d = 50$ km, which is why we choose a larger d for these tests. Otherwise the numerical setup is the same as for the mass sequence simulations (see Sec. 3.1). Considering these two additional simulations we can assess the impact of eccentricity on the spectral features since this is the only parameter, which differs between those two calculations. We

refer to the simulation with the quasi-circular ID and the simulation with reduced eccentricity as QC and RE, respectively.

The separation distance between the two NSs is computed by assuming that the center of mass of the star coincides with the location of the maximum rest-mass density $\rho_{\max}$. With these coordinates $(x_{\max}, y_{\max})$ in the orbital plane we define the separation distance by

$$d(t) = 2 \cdot \sqrt{x_{\max}^2 + y_{\max}^2}. \tag{A.1}$$

where the factor 2 reflects the pi-symmetry of the system.

The time evolution of the coordinate separation distance $d(t)$ for both simulations is shown in Fig. A.1. We find that the residual eccentricity in the QC simulation is $e \approx 0.0088$ and the reduced residual eccentricity of the RE simulation is $e \approx 0.00089$. As expected, the QC simulation exhibits small modulations in the separation distance $d(t)$, while in the RE simulation these oscillations disappear, due to the reduced eccentricity.

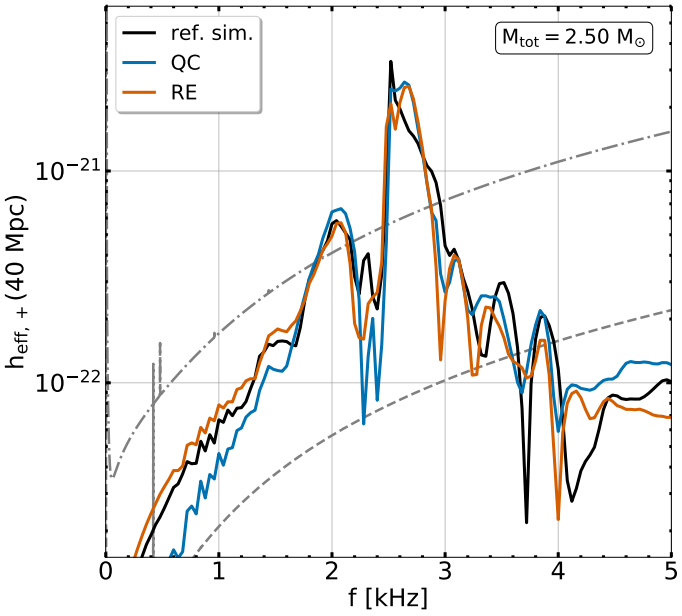

Figure A.2: Effective GW spectra $h_{\mathrm{eff},+}(f)$ for the reference simulation (black) and simulations QC (blue) and RE (orange). The dash dotted curves denote the design sensitivity Advanced LIGO [2] and of the Einstein Telescope [3], respectively. Figure taken from [4].

The GW spectra for the reference simulation and the simulations QC and RE are shown in Fig. A.2. The spectra agree in the general features and their morphology, and the frequency peaks coincide. The spectra exhibit an f_{peak} which is one-sided, and a dominant secondary peak, f_{spiral}, with comparable strength. We conclude that it is unlikely that the residual eccentricity in the ID affects the mechanisms for the frequency of evolution of f_{peak} or the formation of the antipodal bulges and thus f_{spiral}. We observe small differences in the amplitudes of the

frequency peaks. These might be explained by differences in the impact velocities during the collision. However, these differences can also be seen between the reference simulation and the simulation QC, which only differ in initial separation distance. We also note that the morphology of the main peak is to some extent affected by the initial orbital separation.

We compute the analytic (Ac) and semi-analytic (Sc) model fits for the two simulations and find large fittings factors of FF $\gtrsim 0.970$ (see Tab. A.1). The initial phases $\phi_{\rm i}$ (for $\rm i = peak, spiral, 2 \pm 0$) are overplotted together with Eq. (5.24)-(5.26) in Fig. A.3. We find that the tight correlations between the phases still hold and the impact of residual eccentricities is negligible. The initial phases $\phi_{\rm i}$ (for $i = \rm peak, spiral, 2 \pm 0$) are shifted with additions or subtractions of multiples of 2π.

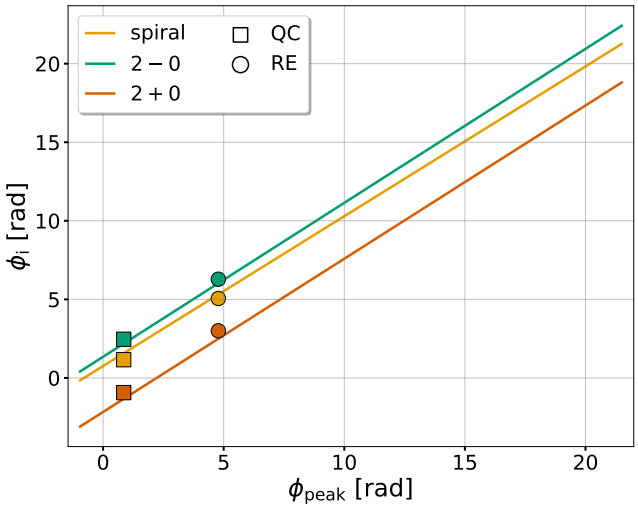

Figure A.3: Initial phases $\phi_{\rm i}$ (for i=spiral, 2 ± 0) with respect to $\phi_{\rm peak}$ for the analytic model (Ac) fits for the simulations QC (square) and RE (circle). Colored lines correspond to Eq. (5.24)-(5.26). Figure taken from [4].

Fitting Factors (FFs)		
Simulation	Sc	Ac
QC	0.969	0.978
RE	0.981	0.979

Table A.1: Fitting factors FFs for the analytic (Ac) and semi-analytic (Sc) model fits for the simulations QC and RE.

A.2. Resolution study

Furthermore, we study the impact of the resolution on the spectral properties. We carry out an additional high resolution simulation with total binary mass $M_{\rm tot} = 2.5\ M_\odot$ (as in the reference model) and finest grid spacing of $dx = 185$ m

(keeping same number of refinement levels). The rest of the numerical setup is identical to the one described in Sec. 3.1. We refer to the high resolution simulation as HR.

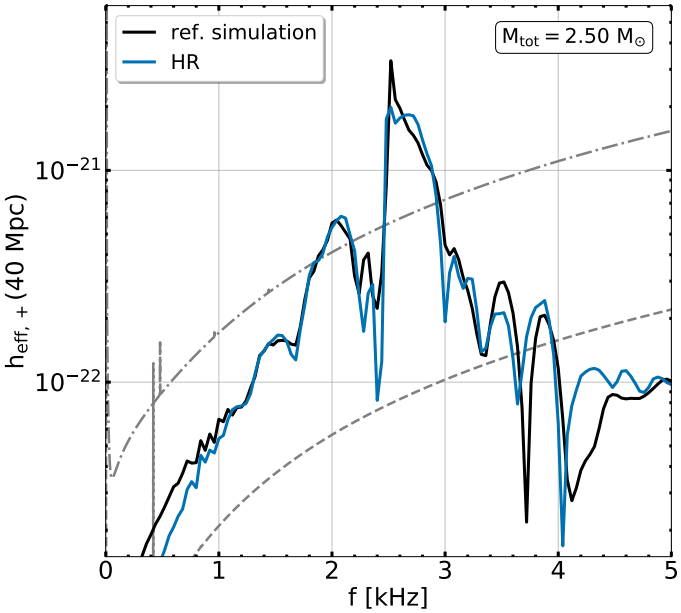

Figure A.4: Effective GW spectra $h_{\mathrm{eff},+}(f)$ for the reference simulation (black) and the high resolution simulation HR (blue). The dash dotted curves denote the design sensitivity Advanced LIGO [2] and of the Einstein Telescope [3], respectively. Figure taken from [4].

The GW spectra for the reference and HR simulation are shown in Fig. A.4. The agreement between the frequency peaks is remarkable, although there are small differences in the morphology of the main peak. The time-dependent $f_{\mathrm{peak}}(t)$ is in agreement in both simulations, and also we find a very good match between the secondary frequencies, especially for f_{spiral}, f_{2-0}. The spectrograms for the two simulations are shown in Fig. A.5. These confirm that in spite of the differences in the structure of the main peak shown in the spectra of Fig. A.4, the time-evolution of $f_{\mathrm{peak}}(t)$ is qualitatively similar in both cases. It can thus be described by the same analytic model that we describe in the main text.

Fitting Factors (FFs)		
Simulation	Sc	Ac
ref.	0.969	0.956
HR	0.978	0.974

Table A.2: Fitting factors FFs for the analytic (Ac) and semi-analytic (Sc) model fits for the HR simulation.

We also compute the analytic (Ac) and semi-analytic (Sc) model fits for the HR simulation and find large fitting factors of FF $\gtrsim 0.970$ (see Tab. A.2). We note that for this particular configuration the FFs are even larger than the ones obtained for the reference simulation.

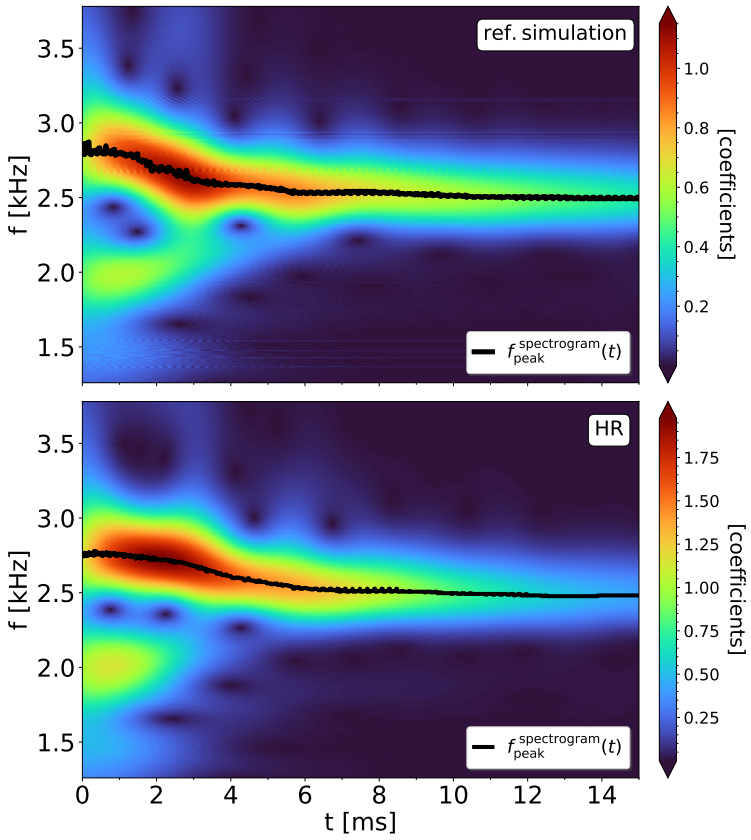

Figure A.5: *Top panel*: spectrogram of $h_+(t)$ for the reference simulation. *Bottom panel*: spectrogram of $h_+(t)$ for the high resolution simulation HR. The black curves correspond to the numerically extracted $f_{\mathrm{peak}}^{\mathrm{spectrogram}}(t)$ for the reference simulation and HR, respectively. Figure taken from [4].

A.3. Effect of pi-symmetry

We discuss the impact of the pi-symmetry during the simulations. We perform additional simulations using the same numerical setup as described in Sec. 3.1 but without pi-symmetry. We consider models with $M_{\mathrm{tot}} = 2.5\ M_\odot$, $2.7\ M_\odot$, $2.9\ M_\odot$ and $3.0\ M_\odot$. Figure A.6 displays the GW spectra for the simulations with and without pi-symmetry. We find a very good agreement between the respective GW spectra. We conclude that imposing pi-symmetry does not impact the spectral features and in particular the $f_{\mathrm{spiral}\pm 0}$ coupling, which is discussed in Sec. 4.1.3, is unaffected by the pi-symmetry.

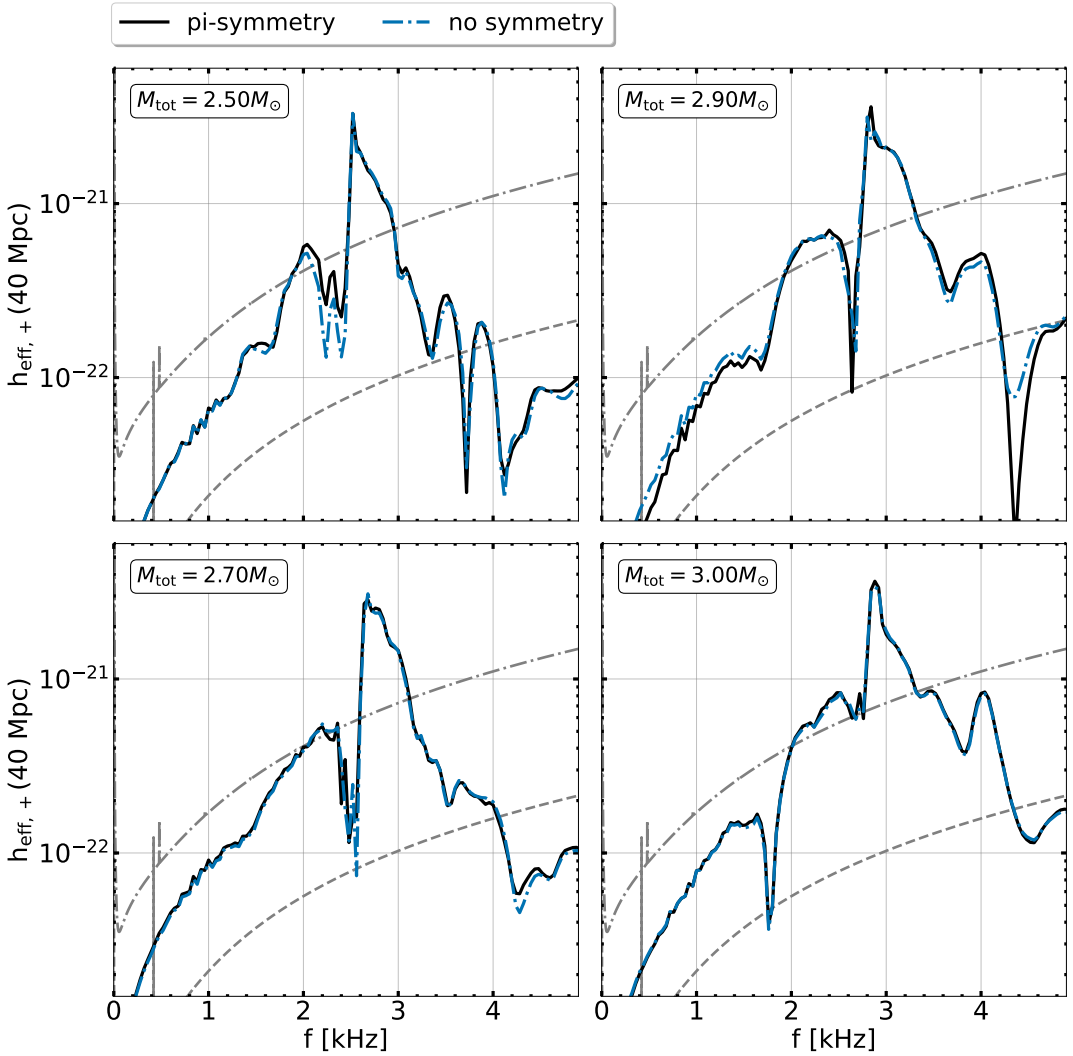

Figure A.6: Effective GW spectra $h_{\rm eff,+}(f)$ for the $M_{\rm tot} = 3.0\ M_\odot$ simulation with pi-symmetry (black) and without pi-symmetry (blue). The dash dotted curves denote the design sensitivity Advanced LIGO [2] and of the Einstein Telescope [3], respectively. Figure adapted from [4].

B. Analytic model & spectral analysis

In this chapter we provide additional figures regarding the discussion of Chapter 4, Chapter5.

B.1. Spectral properties of the mass sequence models

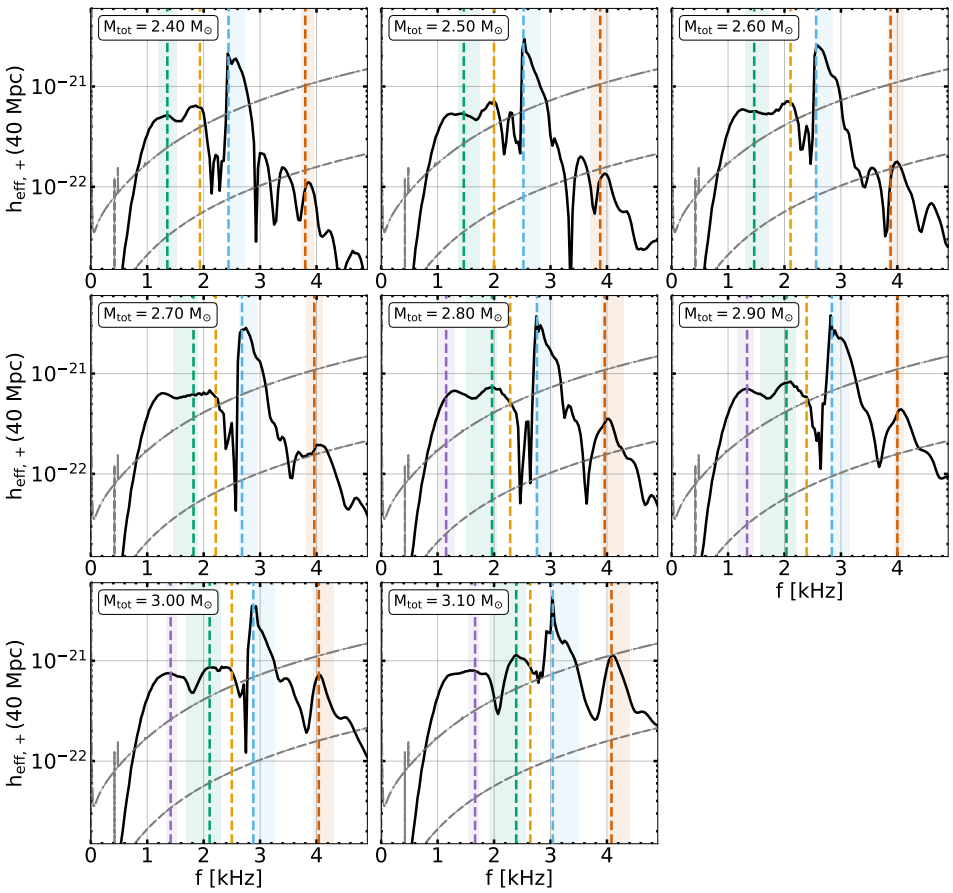

Figure B.1: As Fig. 4.2 but including the inspiral signal. Figure taken from [4].

We present supplementary figures for the mass sequence models described in Sec. 3.1. Figure B.1 shows the GW spectra including the inspiral signal. Figure B.2

displays the spectrograms for the post-merger GW signal $h_+(t)$. Figure B.3 provides the spectrograms for the minimum lapse function $\alpha_{\min}(t)$ starting at a few milliseconds before the merging phase.

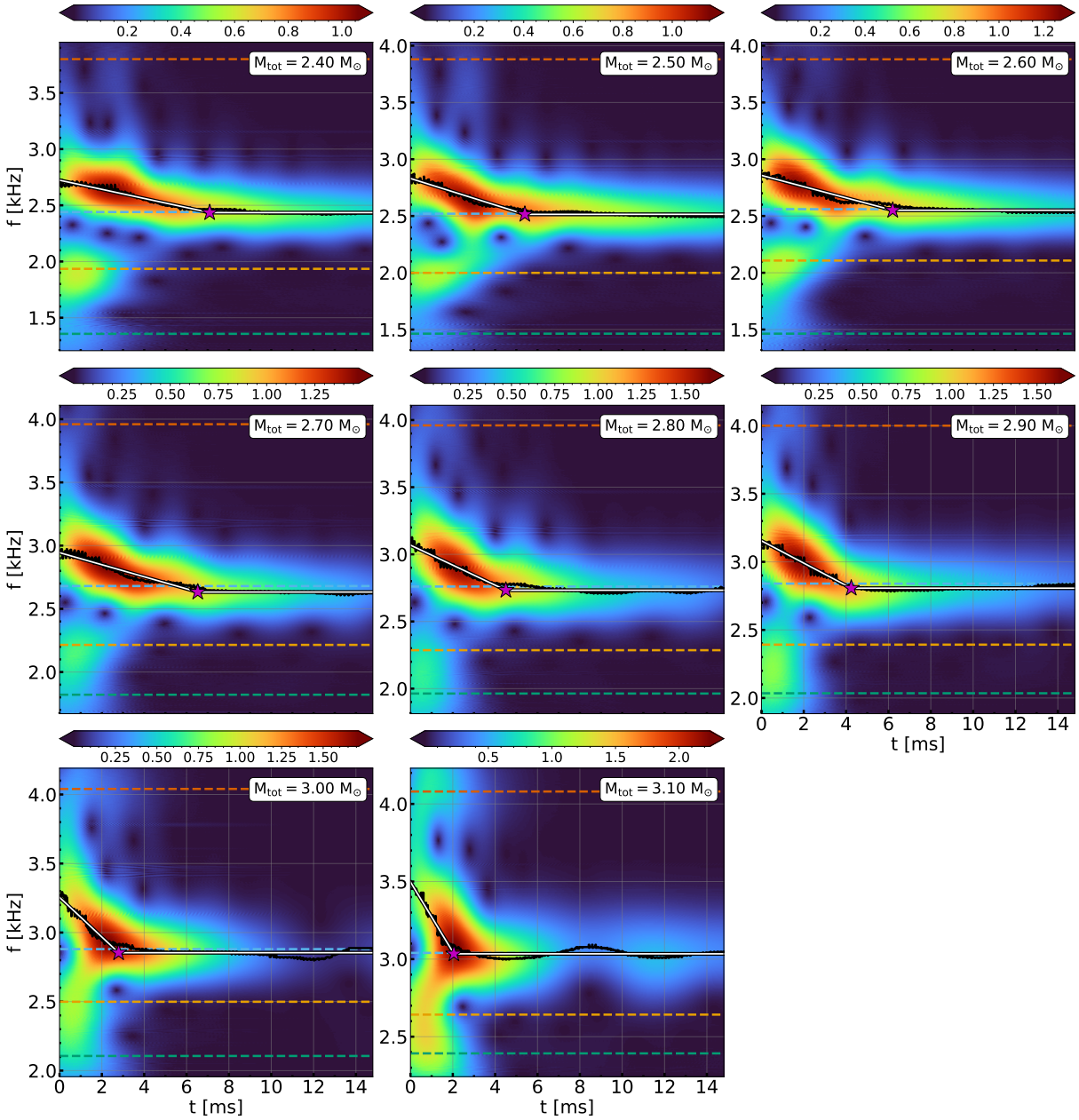

Figure B.2: As Fig. 4.1 but for all models in our mass sequence. Figure taken from [4].

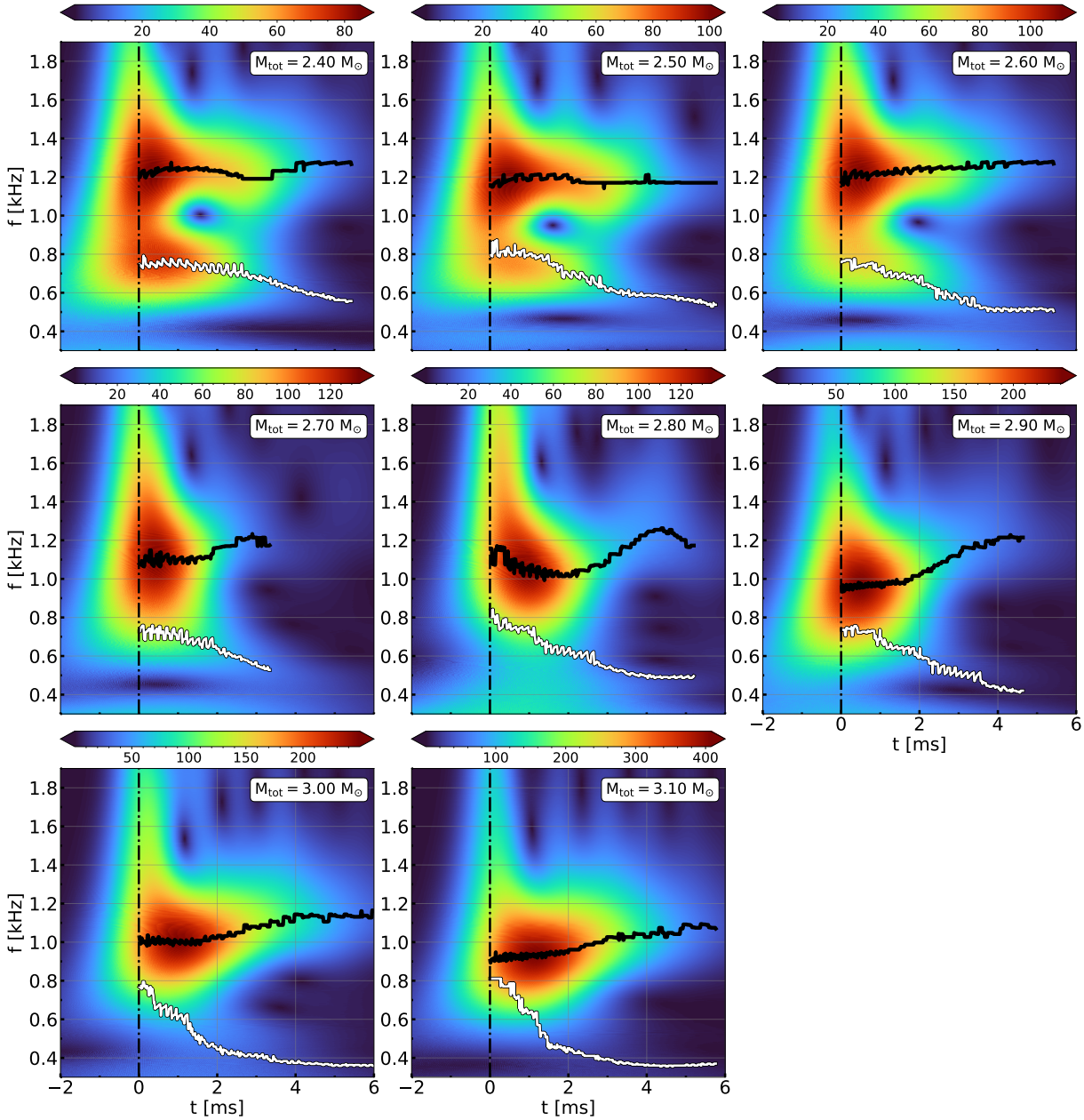

Figure B.3: As Fig. 4.3 but for all models of our mass sequence. Figure taken from [4].

B.2. Analytic model

In this section we present supplementary figures regarding the analytic model introduced in Sec. 5.

B.2.1. Spectrogram analysis

We quantitatively analyze the spectrograms of the numerical simulation and of the analytic fit. Figures Fig. B.4a to Fig. B.4c depict the wavelet coefficients

$\mathcal{A}_{\rm peak}(t)$, $\mathcal{A}_{\rm spiral}(t)$, $\mathcal{A}_{2-0}(t)$, which we extract at the corresponding frequencies from the spectrograms as function of time, for the simulation (blue line) and for the analytic fit (orange line). The three coefficient curves of the simulation data are reproduced very well by the analytic model. For illustration purposes, we omit the normalization factor $\mathcal{N}$ and overlay the corresponding exponentially decaying sinusoid functions for each frequency component while we rescale the coefficient curves by a constant factor which ensures that the maxima of $\Big(h_{\rm peak}(t)\mathcal{W}(t;s)\Big)$ and $\mathcal{A}_{\rm peak}(t)$ coincide.

We note that the three components exhibit different magnitudes of the coefficient curves $\mathcal{A}_{\rm i}(t)$, whereas the amplitudes $A_{\rm i}$ (i = peak, spiral, $2-0$) of the analytic model are roughly comparable. For our reference simulation with a total binary mass $M_{\rm tot} = 2.5 M_\odot$, we actually expect that the $f_{\rm spiral}$ component is the strongest secondary feature, which is also suggested by the GW spectrum, and in fact the maxima of the coefficients show this hierarchy. We thus remark that the amplitudes $A_{\rm i}$ of the analytic model may have only a limited physical meaning, while other quantities, such as the surface area under $\mathcal{A}_{\rm i}(t)$, the maxima of $\mathcal{A}_{\rm i}(t)$ or the product $A_{\rm i} \cdot \tau_i$ may turn out to be more representative for the merger dynamics and GW emission.

B.2.2. Sequence of simulations with different masses

Figure B.5 shows the time-domain signals for the simulation and the analytic model along the sequence of simulations with different masses. Notice the possible excitation of a low-$|T/W|$ rotational instability in the highest-mass model, after ~ 10 ms from the onset of merger [153–155].

B.2.3. Initial phases

We find that the initial phases $\phi_{\rm peak}$, $\phi_{\rm spiral}$, $\phi_{2\pm0}$ correlate with the total binary mass $M_{\rm tot}$. We model this dependence with a 2-segment piecewise function consisting of two linear fits which intersect at $M_{\rm tot} = 2.7\ M_\odot$. These are given by

$$\phi_{\rm peak} = \begin{cases} +18.957 \cdot M_{\rm tot} - 46.321 & \text{for } M_{\rm tot} \leq 2.7\ M_\odot \\ +43.425 \cdot M_{\rm tot} - 113.152 & \text{for } M_{\rm tot} > 2.7\ M_\odot \end{cases} \tag{B.1}$$

$$\phi_{\rm spiral} = \begin{cases} +17.580 \cdot M_{\rm tot} - 42.199 & \text{for } M_{\rm tot} \leq 2.7\ M_\odot \\ +40.448 \cdot M_{\rm tot} - 104.258 & \text{for } M_{\rm tot} > 2.7\ M_\odot \end{cases} \tag{B.2}$$

$$\phi_{2-0} = \begin{cases} +18.541 \cdot M_{\rm tot} - 43.911 & \text{for } M_{\rm tot} \leq 2.7\ M_\odot \\ +43.613 \cdot M_{\rm tot} - 112.705 & \text{for } M_{\rm tot} > 2.7\ M_\odot \end{cases} \tag{B.3}$$

$$\phi_{2+0} = \begin{cases} +16.064 \cdot M_{\rm tot} - 41.163 & \text{for } M_{\rm tot} \leq 2.7\ M_\odot \\ +43.309 \cdot M_{\rm tot} - 115.341 & \text{for } M_{\rm tot} > 2.7\ M_\odot \end{cases} \tag{B.4}$$

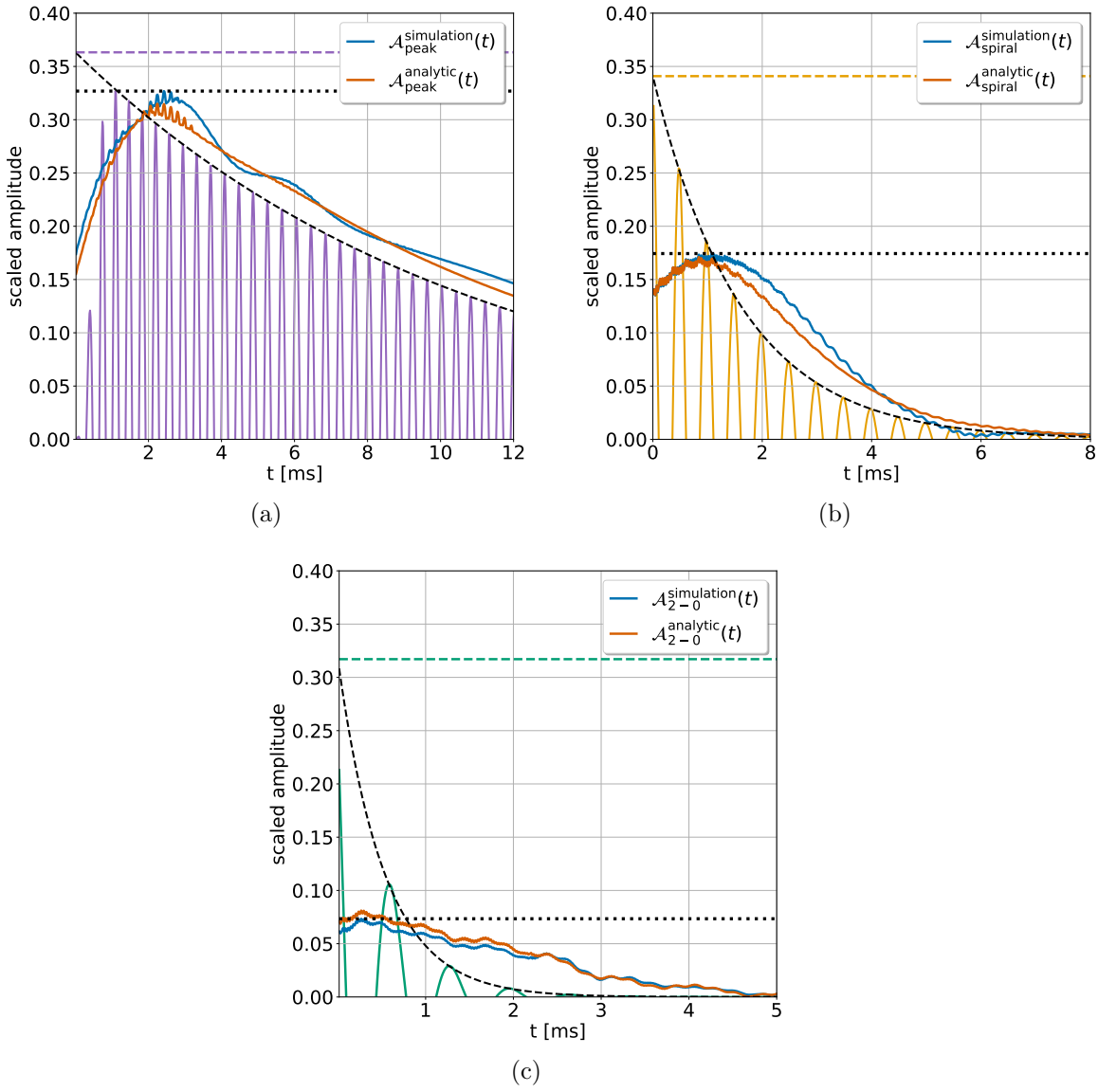

Figure B.4: *Top left panel*: Coefficient curves $\mathcal{A}_{\text{peak}}(t)$ for the f_{peak} component extracted from the spectrograms of simulation and analytic model. Purple dashed line indicates amplitude A_{peak}. Black dotted horizontal line shows maximum of $\mathcal{A}_{\text{peak}}(t)$ for simulation. Purple sinusoidal curve shows f_{peak} component as used in the analytic model. Dashed black curve shows its exponential decay. *Top right panel*: Coefficient curves $\mathcal{A}_{\text{spiral}}(t)$ for the f_{spiral} component extracted from spectrograms of simulation and analytic model. Yellow dashed line shows the amplitude A_{spiral}. Black dotted horizontal line indicates the maximum of $\mathcal{A}_{\text{spiral}}(t)$ for simulation. Yellow sinusoidal curve shows f_{spiral} component as used in the analytic model. Dashed black curve shows its exponential decay. *Bottom panel*: Coefficient curves $\mathcal{A}_{2-0}(t)$ for the f_{2-0} component extracted from spectrograms of simulation and analytic model. Yellow dashed line shows amplitude A_{2-0}. Black dotted horizontal line indicates maximum of $\mathcal{A}_{2-0}(t)$ for simulation. Yellow sinusoidal curv shows f_{2-0} component as used in the analytic model. Dashed black curve shows its exponential decay. Figures taken from [4].

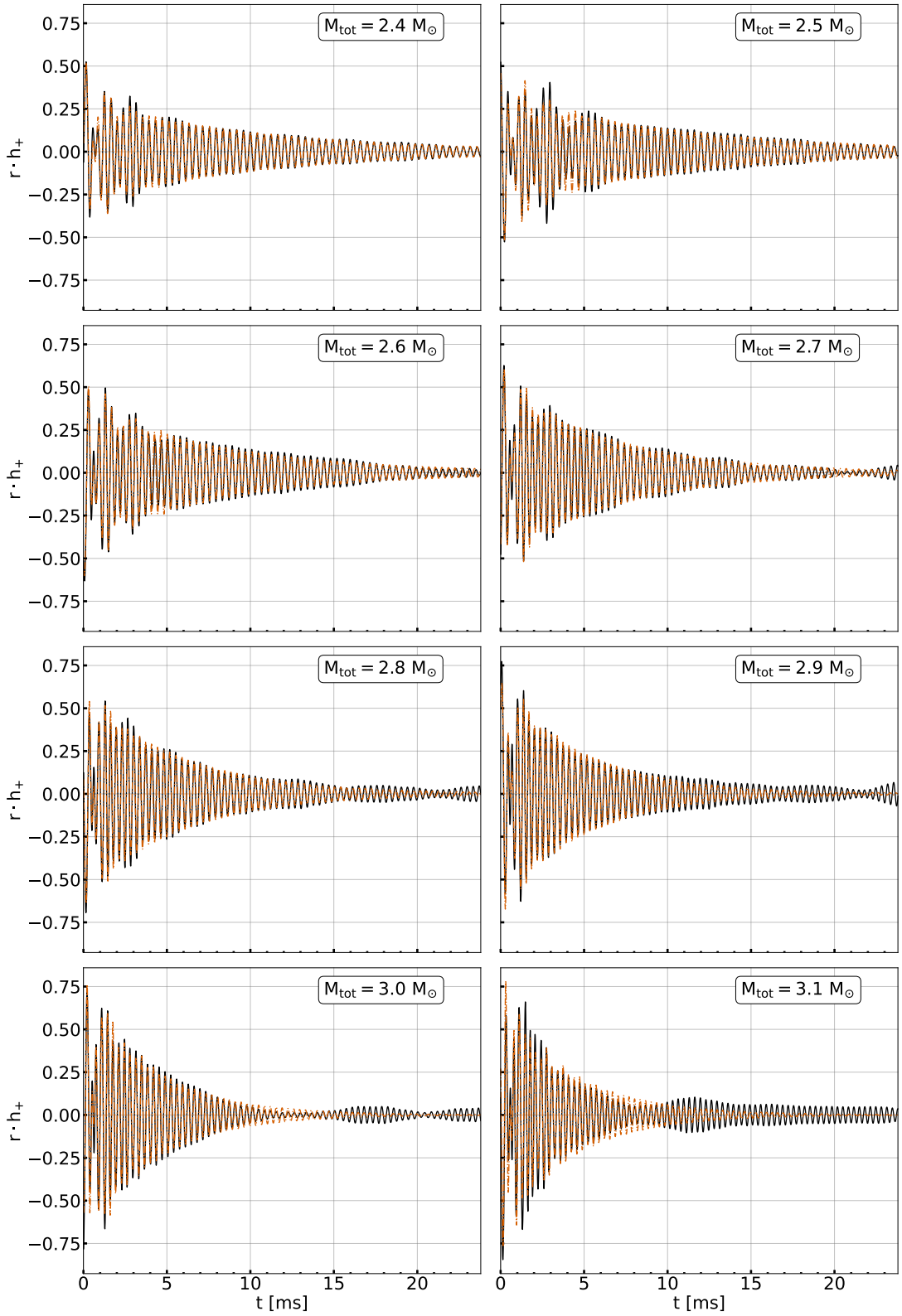

Figure B.5: As Fig. 5.1 but for all models of our mass sequence. Figure adapted from [4].

B.2.4. Empirical relations

In subsection we summarize the notation and the units for all the parameters of our analytic model. Table B.1 provides information about the analytic model's parameters. The fits are carried out for the signals $r \cdot h_s(t)$ (for $s = +, \times$).

Analytic model's parameters		
Symbol	Unit	Equation
M	$M_\odot$	-
$h_{\text{eff},+}(f) = f \cdot \widetilde{h}_+(f)$	dimensionless	-
Sensitivity curve $\equiv \sqrt{S_h(f) \cdot f}$	dimensionless	-
f_{peak}	kHz	-
f_{spiral}	kHz	-
$f_{2\pm0}$	kHz	-
$f_{\text{spiral}\pm0}$	kHz	-
ζ_{drift}	kHz^2	(5.9)
$f_{\text{peak},0}$	kHz	(5.10)
t_*	ms	(5.11)
A_{peak}	dimensionless	(5.15)
τ_{peak}	ms	(5.16)
τ_{spiral}	ms	(5.17)
τ_{2-0}	ms	(5.18)
τ_{2+0}	ms	(5.19)
A_{spiral}	dimensionless	(5.20)
A_{2-0}	dimensionless	(5.21)
A_{2+0}	dimensionless	(5.22)
$\mathcal{N}$	dimensionless	(5.23)
ϕ_{peak}	rad	(B.1)
ϕ_{spiral}	rad	(5.24),(B.2)
ϕ_{2-0}	rad	(5.25),(B.3)
ϕ_{2+0}	rad	(5.26),(B.4)

Table B.1: The analytic model's parameters. Table taken from [4].

C. Empirical relations

In this chapter we present empirical relations for f_{spiral}, $f_{\mathrm{spiral}-0}$, and f_0 constructed using the data set described in Sec. 3.2.1. We find that the secondary frequency f_{spiral} correlates well with the quadrupolar frequency f_{peak} for a wide range of binary masses. We identify $f_{\mathrm{spiral}-0}$ in the post-merger GW spectra and construct empirical relations, which may aid the construction of GW templates like those described in Chapter 5. Furthermore, we propose an empirical relation which connects f_0 to f_{peak} and M_{chirp}. We note that these empirical relations can also be used to constrain the incompletely known EoS.

C.1. Description of data

In this section we describe the two different subsets of the symmetric binary simulations that we use for the construction of the empirical relations.

For the empirical relations for the frequencies f_{spiral} and $f_{\mathrm{spiral}-0}$ we only consider binaries where the proximity to threshold mass is roughly $\Delta M \gtrsim 0.1\ M_{\odot}$. This is because for models close to prompt collapse the GW spectrum is more complicated and the identification of f_{spiral} is not trivial. It may be that additional oscillation modes and combination tones are excited (see Chapter 6), or for some EoS models f_{spiral} is not sufficiently strong. In these cases, a close inspection of the density profiles (see [28]) is required for identifying f_{spiral}. In this work, we follow the method described in Sec. 4.1.3 in order to identify f_{spiral} and $f_{\mathrm{spiral}-0}$. In summary, we use the empirical relations of [49] to obtain a rough estimate of f_{spiral} and then pick the frequency at the maximum in the GW spectrum in the vicinity of the estimate. Similarly, we identify $f_{\mathrm{spiral}-0}$ using the approximate relation $f_{\mathrm{spiral}-0} \approx f_{\mathrm{spiral}} - f_0$. The frequency f_0 for each model is extracted using the method described in Chapter 7. In addition, we note that for low masses $f_{\mathrm{spiral}-0}$ is typically not excited. Thus, when there is no clear frequency peak in the vicinity of the estimate of $f_{\mathrm{spiral}-0}$, we do not include the corresponding model in the construction of the empirical relation.

In the empirical relation for f_0 we do not have the aforementioned problem for high-mass models because determining f_0 is relatively straightforward at least for symmetric binaries. However, as in the case of $f_{\mathrm{spiral}-0}$, we exclude low mass configurations where the quasi-radial model is only weakly excited.

C.2. $f_{\rm spiral}$

We introduce a quasi-universal relation between the secondary frequency $f_{\rm spiral}$ and the quadrupolar frequency $f_{\rm peak}$. Figure C.1 displays the frequencies $f_{\rm spiral}$ as a function of $f_{\rm peak}$ for all the binaries considered in this subset of simulations. Such relations were introduced in [41] but only for fixed binary masses, while in this work we consider a wide range of masses. We remark that we do not find quasi-universal relations of the other secondary components, $f_{2\pm0}$ and $f_{\rm spiral\pm0}$, as a function of $f_{\rm peak}$. This is because the other components contain information of f_0, which does not follow such simple relation (see Chapter 7). In contrast, the angular velocity of the antipodal bulges is expected to correlate with the inner core of the remnant and $f_{\rm peak}$. We model the $f_{\rm spiral}(f_{\rm peak})$ relation with a linear function and find an average absolute error between the data and the fit of 0.05 kHz. The analytic fit reads

$$f_{\rm spiral} \;=\; +0.9571\; f_{\rm peak} - 0.5246. \tag{C.1}$$

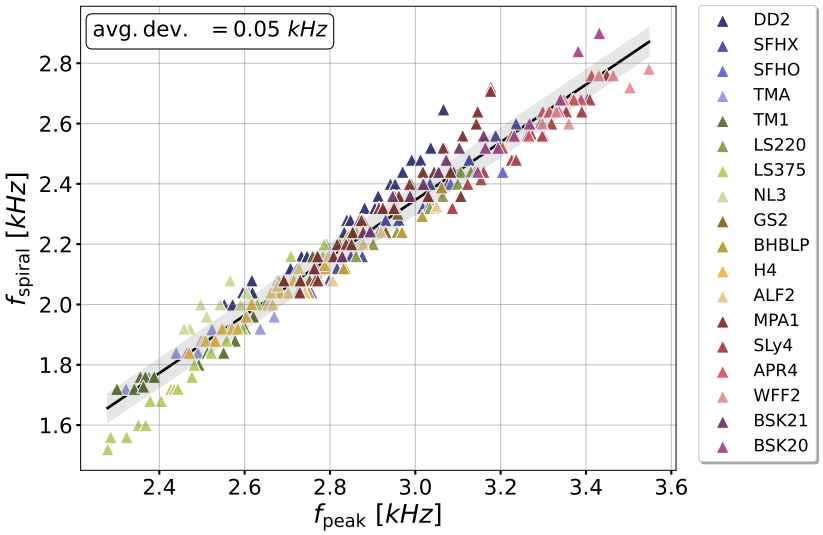

Figure C.1: $f_{\rm spiral}$ as a function of $f_{\rm peak}$ for a wide range of symmetric binary simulations.

C.3. $f_{\rm spiral-0}$

The authors of [49] computed empirical relations for the frequencies $f_{\rm peak}$, f_{2-0}, $f_{\rm spiral}$. They considered the scaled by $M_{\rm chirp}$ frequencies $f_i/M_{\rm chirp}$ (for $i =$ peak, 2-0, spiral) and performed the fits using a two-parameter function of the form

$$\begin{aligned} f_i/M_{\rm chirp} \;=\; & a_1 M_{\rm chirp} + b_1 R_x + a_2 M_{\rm chirp}^2 + b_2 R_x^2 \\ & + c M_{\rm chirp} \cdot R_x + d, \end{aligned} \tag{C.2}$$

where $i =$ peak, 2-0, spiral, R_x is the radius of the NS with gravitational mass x with $x = 1.2, 1.4, 1.6, 1.8$. Relations like these can be employed in GW templates. For this reason, we use Eq. (C.2) for $R_x = R_{1.6}$ and perform a fit for the frequency $f_{\mathrm{spiral}-0}$ for our subset of symmetric binary merger simulations. Figure C.2 displays our empirical relation for $f_{\mathrm{spiral}}/M_{\mathrm{chirp}}$ as a function of M_{chirp} and $R_{1.6}$. The two-parameter fit reads

$$\begin{aligned} f_{\mathrm{spiral}-0}/M_{\mathrm{chirp}} \;=\; & +6.112\; M_{\mathrm{chirp}} - 1.409\; R_x \\ & -0.790\; M_{\mathrm{chirp}}^2 + 0.058\; R_x^2 \\ & -0.256\; M_{\mathrm{chirp}} \cdot R_x \\ & +7.275. \end{aligned} \tag{C.3}$$

We convert the predictions from the empirical relation to values of $f_{\mathrm{spiral}-0}$ and find an average absolute deviation between the data the empirical relation of 0.0517 kHz and a maximum deviation of 0.264 kHz. Both numbers are comparable to those of the empirical fits for $f_{\mathrm{peak}}, f_{\mathrm{spiral}}, f_{2-0}$ in [49].

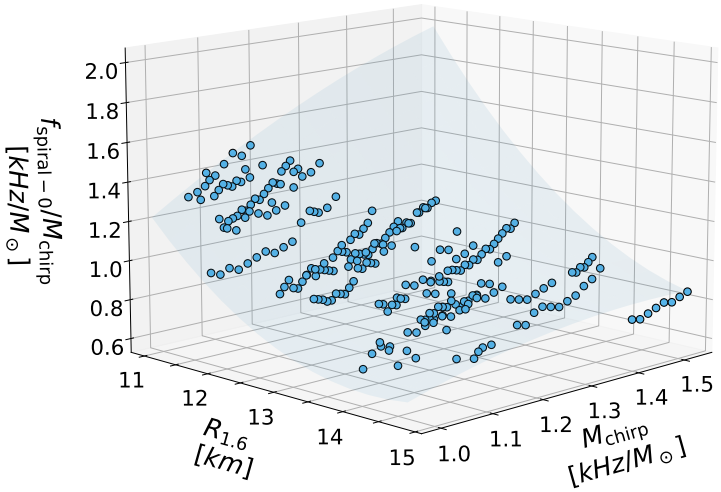

Figure C.2: $f_{\mathrm{spiral}-0}/M_{\mathrm{chirp}}$ as a function of $R_{1.6}$ and M_{chirp} for the subset of symmetric binary merger simulations.

As can be seen in Fig. C.2, the values of $f_{\mathrm{spiral}-0}/M_{\mathrm{chirp}}$ follow a rather smooth trend. This implies that the mechanism which produces this frequency component, namely the spiral $\pm\, 0$ coupling, depends systematically on the characteristics of the system. This supports our conjecture that $f_{\mathrm{spiral}-0}$ is indeed a general feature of the GW spectra, which may be measurable in future searches.

C.4. f_0

We find a correlation between the quasi-radial frequencies f_0/M_{chirp}, the chirp mass M_{chirp}, and the quadrupolar frequency f_{peak} (see Fig. C.3). We consider a two-

parameter function similar to Eq. (C.2) where we replace R_x with $f_{\rm peak}/M_{\rm chirp}$ (inspired by [49]) and perform the fit. Figure C.3 shows the empirical relation $f_0/M_{\rm chirp}(M_{\rm chirp}, f_{\rm peak}/M_{\rm chirp})$ along with the simulation data. The relation reads

$$\begin{aligned} f_0/M_{\rm chirp} \;=\; & +3.035\ M_{\rm chirp} + 5.373\ f_{\rm peak}/M_{\rm chirp} \\ & -0.202\ M_{\rm chirp}^2 - 1.101\ (f_{\rm peak}/M_{\rm chirp})^2 \\ & -1.654\ f_{\rm peak} \\ & -5.357. \end{aligned} \tag{C.4}$$

We find an average absolute deviation between the data the empirical relation of 0.0487 kHz and a maximum deviation of 0.182 kHz.

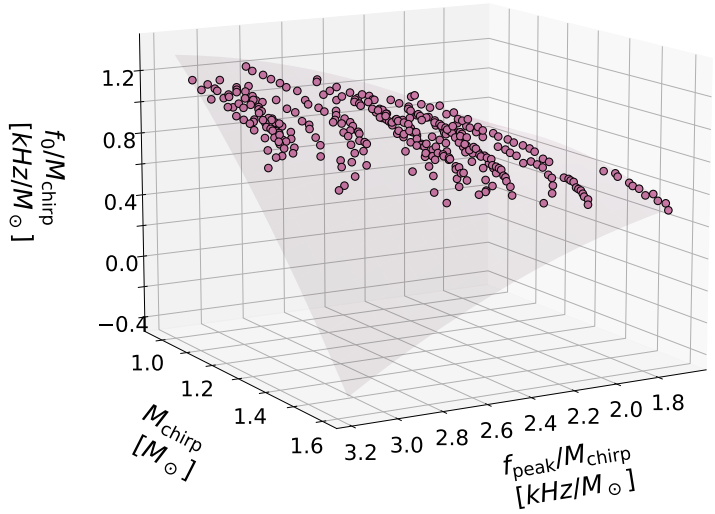

Figure C.3: $f_0/M_{\rm chirp}$ as a function of $M_{\rm chirp}$ and $f_{\rm peak}/M_{\rm chirp}$ for the subset of symmetric binary merger simulations.

We remark that using this relation, a combined measurement of $M_{\rm chirp}$ obtained from the inspiral and a measurement of $f_{\rm peak}$ obtained from the post-merger signal determines f_0. As discussed in Chapter 7, f_0 encodes information about the threshold mass, and so, it may be used to constrain the EoS. Furthermore, this relation provides a method that is independent of the GW data analysis tool used during the detection. This is because f_0 is determined from $M_{\rm chirp}$ and $f_{\rm peak}$ and not from the secondary components of the GW spectrum. We aim to further explore this particular relation in future work.

Acknowledgments

First, I would like to thank my advisor Andreas Bauswein for his guidance, continuous support, and the enthusiasm he showed for my results and the new ideas that I brought throughout this project. The collaboration with Andreas was surely a pleasant experience and I am grateful for it.

Also, I would like to thank Fritz Röpke who welcomed me to his group, PSO at HITS. I am thankful for the various opportunities that I had to discuss my progress with PSO. In addition, I thank the other members of the examination committee, Christian Fendt, Cornelis P. Dullemond, and Hans-Christian Schultz-Coulon. Special thanks to Christian for agreeing to be a referee for this thesis.

I also express my sincere thanks to Nikolaos Stergioulas, my collaborator and advisor during my MSc thesis project in Thessaloniki, where I was first introduced to the field of neutron star mergers. I am happy that we continue to work together, discuss, and exchange ideas for new projects.

I would like to thank my good friend and collaborator, Georgios Lioutas, for all the nice discussions we had and funny moments we shared throughout these years. He was always eager to help me and share his knowledge, especially on the theoretical but also on the technical aspects of the project, which is greatly appreciated.

I express my sincere gratitude to the rest of my collaborators: Javier Morán-Fraile, my friend and office mate at PSO with whom, we significantly increased the loudness of the office. Sebastian Blacker and Vimal Vijayan, my colleagues at GSI with whom we had many funny moments. In addition, I thank in alphabetical order: Blaschke D., Chatziioannou K., Coughlin M., Criswell A., Fischer T., Jones G., Mandic V., Miller J., Oertel M., Ohlmann S., Pakmor R., Schneider F., Springel V., Typel, S., Woldemariam N.

My work was supported by the Klaus Tschira Foundation and HITS which provided me substantial computational resources and a wonderful workspace. I also acknowledge financial support from the International Max Planck Research School for Astronomy and Cosmic Physics at the University of Heidelberg (IMPRS-HD), and support from the High Performance and Cloud Computing Group at the Zentrum für Datenverarbeitung of the University of Tübingen, the state of Baden-Württemberg through bwHPC and the German Research Foundation through grant no INST 37/935-1 FUGG.

Furthermore, I want to offer my special thanks to the people from HITS with whom I formed friendships and made my time in Heidelberg much more enjoyable, Giovanni, Hans, Sabrina, Christian, Alex, Cristian, Fede, Ana, Melvin, Nick, Leo, Jan, Kiril, and many others whom I may forget. I want to thank my friends from Thessaloniki: Vagelis, Vassilis, Nikos, Apostolos, with whom I shared numerous funny moments throughout these years. Nikos Chatzarakis, whose saying, "a good thesis is a finished thesis", echoed in my mind especially during the final days before the submission of the thesis.

Last but not least, I want to thank my parents, Ioanna and Dimitris, and siblings, Evangelia and Miltos, and my partner, Andriana, for their unconditional love and constant support. Special thanks to Andriana for having my back, listening to me, and encouraging me to continue throughout these years. She always tried to understand my problems, both scientific and everyday life-related, and even find solutions, which I greatly appreciate. I also want to thank her for proofreading the thesis. She has been such a big part of my life, my best friend, and I am very grateful for it.

List of publications

Publications:

[1] Soultanis, T., Bauswein, A. & Stergioulas, N. Analytic models of the spectral properties of gravitational waves from neutron star merger remnants. *Phys. Rev. D.* **105**, 043020 (2022,2)

[2] Bauswein, A., Blacker, S., Lioutas, G., Soultanis, T., Vijayan, V. & Stergioulas, N. Systematics of prompt black-hole formation in neutron star mergers. *Phys. Rev. D.* **103**, 123004 (2021,6)

[3] Blacker, S., Bastian, N., Bauswein, A., Blaschke, D., Fischer, T., Oertel, M., Soultanis, T. & Typel, S. Constraining the onset density of the hadron-quark phase transition with gravitational-wave observations. *Phys. Rev. D.* **102**, 123023 (2020,12)

Pre-prints:

[1] Lioutas, G., Bauswein, A., Soultanis, T., Pakmor, R., Springel, V. & Röpke, F. General relativistic moving-mesh hydrodynamics simulations with AREPO and applications to neutron star mergers. *ArXiv E-prints.* (2022,8)

Bibliography

[1] B. P. Abbott *et al.*, "Properties of the binary neutron star merger GW170817," *Phys. Rev. X*, vol. 9, no. 1, p. 011001, 2019.

[2] J. Aasi *et al.*, "Advanced LIGO," *Class. Quant. Grav.*, vol. 32, p. 074001, 2015.

[3] M. Punturo, M. Abernathy, F. Acernese, B. Allen, N. Andersson, K. Arun, F. Barone, B. Barr, M. Barsuglia, M. Beker, *et al.*, "The Einstein Telescope: a third-generation gravitational wave observatory," *Classical and Quantum Gravity*, vol. 27, p. 194002, Oct. 2010.

[4] T. Soultanis, A. Bauswein, and N. Stergioulas, "Analytic models of the spectral properties of gravitational waves from neutron star merger remnants," *Phys. Rev. D*, vol. 105, p. 043020, Feb 2022.

[5] A. Bauswein, S. Blacker, G. Lioutas, T. Soultanis, V. Vijayan, and N. Stergioulas, "Systematics of prompt black-hole formation in neutron star mergers," *Phys. Rev. D*, vol. 103, p. 123004, Jun 2021.

[6] B. P. Abbott, R. Abbott, T. D. Abbott, F. Acernese, K. Ackley, C. Adams, T. Adams, P. Addesso, R. X. Adhikari, V. B. Adya, *et al.*, "GW170817: Observation of Gravitational Waves from a Binary Neutron Star Inspiral," *Phys. Rev. Lett.*, vol. 119, p. 161101, Oct. 2017.

[7] E. Nakar, "Short-hard gamma-ray bursts," *Physics Reports*, vol. 442, no. 1, pp. 166–236, 2007. The Hans Bethe Centennial Volume 1906-2006.

[8] E. Berger, "Short-duration gamma-ray bursts," *Annual Review of Astronomy and Astrophysics*, vol. 52, no. 1, pp. 43–105, 2014.

[9] B. D. Metzger, G. Martínez-Pinedo, S. Darbha, E. Quataert, A. Arcones, D. Kasen, R. Thomas, P. Nugent, I. V. Panov, and N. T. Zinner, "Electromagnetic counterparts of compact object mergers powered by the radioactive decay of r-process nuclei," *Monthly Notices of the Royal Astronomical Society*, vol. 406, pp. 2650–2662, 08 2010.

[10] B. D. Metzger, "Kilonovae," *Living Reviews in Relativity*, vol. 23, p. 1, Dec. 2019.

[11] B. P. Abbott *et al.*, "Gravitational Waves and Gamma-rays from a Binary Neutron Star Merger: GW170817 and GRB 170817A," *Astrophys. J. Lett.*, vol. 848, no. 2, p. L13, 2017.

[12] A. Goldstein, P. Veres, E. Burns, M. S. Briggs, R. Hamburg, D. Kocevski, C. A. Wilson-Hodge, R. D. Preece, S. Poolakkil, O. J. Roberts, C. M. Hui, V. Connaughton, J. Racusin, A. von Kienlin, T. Dal Canton, N. Christensen, T. Littenberg, K. Siellez, L. Blackburn, J. Broida, E. Bissaldi, W. H. Cleveland, M. H. Gibby, M. M. Giles, R. M. Kippen, S. McBreen, J. McEnery, C. A. Meegan, W. S. Paciesas, and M. Stanbro, "An Ordinary Short Gamma-Ray Burst with Extraordinary Implications: Fermi-GBM Detection of GRB 170817A," *ApJL*, vol. 848, p. L14, Oct. 2017.

[13] V. Savchenko, C. Ferrigno, E. Kuulkers, A. Bazzano, E. Bozzo, S. Brandt, J. Chenevez, T. J.-L. Courvoisier, R. Diehl, A. Domingo, L. Hanlon, E. Jourdain, A. von Kienlin, P. Laurent, F. Lebrun, A. Lutovinov, A. Martin-Carrillo, S. Mereghetti, L. Natalucci, J. Rodi, J.-P. Roques, R. Sunyaev, and P. Ubertini, "Integral detection of the first prompt gamma-ray signal coincident with the gravitational-wave event GW170817," vol. 848, p. L15, oct 2017.

[14] E. Troja, L. Piro, H. van Eerten, R. T. Wollaeger, M. Im, O. D. Fox, N. R. Butler, S. B. Cenko, T. Sakamoto, C. L. Fryer, R. Ricci, A. Lien, R. E. Ryan, O. Korobkin, S. K. Lee, J. M. Burgess, W. H. Lee, A. M. Watson, C. Choi, S. Covino, P. D'Avanzo, C. J. Fontes, J. B. González, H. G. Khandrika, J. Kim, S. L. Kim, C. U. Lee, H. M. Lee, A. Kutyrev, G. Lim, R. Sánchez-Ramírez, S. Veilleux, M. H. Wieringa, and Y. Yoon, "The X-ray counterpart to the gravitational-wave event GW170817," *Nature*, vol. 551, pp. 71–74, Nov. 2017.

[15] R. Margutti, E. Berger, W. Fong, C. Guidorzi, K. D. Alexander, B. D. Metzger, P. K. Blanchard, P. S. Cowperthwaite, R. Chornock, T. Eftekhari, M. Nicholl, V. A. Villar, P. K. G. Williams, J. Annis, D. A. Brown, H. Chen, Z. Doctor, J. A. Frieman, D. E. Holz, M. Sako, and M. Soares-Santos, "The electromagnetic counterpart of the binary neutron star merger LIGO/virgo GW170817. v. rising x-ray emission from an off-axis jet," *The Astrophysical Journal*, vol. 848, p. L20, oct 2017.

[16] D. Haggard, M. Nynka, J. J. Ruan, V. Kalogera, S. B. Cenko, P. Evans, and J. A. Kennea, "A deep chandra x-ray study of neutron star coalescence GW170817," *The Astrophysical Journal*, vol. 848, p. L25, oct 2017.

[17] G. Hallinan, A. Corsi, K. P. Mooley, K. Hotokezaka, E. Nakar, M. M. Kasliwal, D. L. Kaplan, D. A. Frail, S. T. Myers, T. Murphy, K. De, D. Dobie, J. R. Allison, K. W. Bannister, V. Bhalerao, P. Chandra, T. E. Clarke, S. Giacintucci, A. Y. Q. Ho, A. Horesh, N. E. Kassim, S. R. Kulkarni, E. Lenc, F. J. Lockman, C. Lynch, D. Nichols, S. Nissanke, N. Palliyaguru, W. M. Peters, T. Piran, J. Rana, E. M. Sadler, and L. P. Singer, "A radio counterpart to a neutron star merger," *Science*, vol. 358, no. 6370, pp. 1579–1583, 2017.

[18] K. D. Alexander, E. Berger, W. Fong, P. K. G. Williams, C. Guidorzi, R. Margutti, B. D. Metzger, J. Annis, P. K. Blanchard, D. Brout,

D. A. Brown, H.-Y. Chen, R. Chornock, P. S. Cowperthwaite, M. Drout, T. Eftekhari, J. Frieman, D. E. Holz, M. Nicholl, A. Rest, M. Sako, M. Soares-Santos, and V. A. Villar, "The electromagnetic counterpart of the binary neutron star merger LIGO/virgo GW170817. VI. radio constraints on a relativistic jet and predictions for late-time emission from the kilonova ejecta," *The Astrophysical Journal*, vol. 848, p. L21, oct 2017.

[19] J. D. Lyman, G. P. Lamb, A. J. Levan, I. Mandel, N. R. Tanvir, S. Kobayashi, B. Gompertz, J. Hjorth, A. S. Fruchter, T. Kangas, D. Steeghs, I. A. Steele, Z. Cano, C. Copperwheat, P. A. Evans, J. P. U. Fynbo, C. Gall, M. Im, L. Izzo, P. Jakobsson, B. Milvang-Jensen, P. O'Brien, J. P. Osborne, E. Palazzi, D. A. Perley, E. Pian, S. Rosswog, A. Rowlinson, S. Schulze, E. R. Stanway, P. Sutton, C. C. Thöne, A. de Ugarte Postigo, D. J. Watson, K. Wiersema, and R. A. M. J. Wijers, "The optical afterglow of the short gamma-ray burst associated with GW170817," *Nature Astronomy*, vol. 2, pp. 751–754, July 2018.

[20] B. P. Abbott, R. Abbott, T. D. Abbott, F. Acernese, K. Ackley, C. Adams, T. Adams, P. Addesso, R. X. Adhikari, V. B. Adya, *et al.*, "Multi-messenger observations of a binary neutron star merger," *The Astrophysical Journal*, vol. 848, p. L12, oct 2017.

[21] L.-X. Li and B. Paczyński, "Transient Events from Neutron Star Mergers," *Astrophys. J. Lett.*, vol. 507, pp. L59–L62, Nov. 1998.

[22] D. Kasen, B. Metzger, J. Barnes, E. Quataert, and E. Ramirez-Ruiz, "Origin of the heavy elements in binary neutron-star mergers from a gravitational-wave event," *Nature*, vol. 551, pp. 80–84, Nov. 2017.

[23] B. P. Abbott *et al.*, "GW170817: Measurements of neutron star radii and equation of state," *Phys. Rev. Lett.*, vol. 121, no. 16, p. 161101, 2018.

[24] K. Chatziioannou, "Neutron-star tidal deformability and equation-of-state constraints," *General Relativity and Gravitation*, vol. 52, p. 109, Nov. 2020.

[25] K. Hotokezaka, K. Kyutoku, H. Okawa, M. Shibata, and K. Kiuchi, "Binary neutron star mergers: Dependence on the nuclear equation of state," *Phys. Rev. D*, vol. 83, p. 124008, Jun 2011.

[26] A. Bauswein, T. W. Baumgarte, and H.-T. Janka, "Prompt merger collapse and the maximum mass of neutron stars," *Phys. Rev. Lett.*, vol. 111, p. 131101, Sep 2013.

[27] N. Stergioulas, A. Bauswein, K. Zagkouris, and H.-T. Janka, "Gravitational waves and non-axisymmetric oscillation modes in mergers of compact object binaries," *Monthly Notices of the Royal Astronomical Society*, vol. 418, pp. 427–436, 11 2011.

[28] A. Bauswein and N. Stergioulas, "Unified picture of the post-merger dynamics and gravitational wave emission in neutron star mergers," *Phys. Rev. D*, vol. 91, p. 124056, Jun 2015.

[29] V. Paschalidis and N. Stergioulas, "Rotating stars in relativity," *Living Reviews in Relativity*, vol. 20, p. 7, Nov. 2017.

[30] T. Dietrich, T. Hinderer, and A. Samajdar, "Interpreting binary neutron star mergers: describing the binary neutron star dynamics, modelling gravitational waveforms, and analyzing detections," *General Relativity and Gravitation*, vol. 53, p. 27, Mar. 2021.

[31] S. Bernuzzi, "Neutron star merger remnants," *General Relativity and Gravitation*, vol. 52, p. 108, Nov. 2020.

[32] X. Zhuge, J. M. Centrella, and S. L. W. McMillan, "Gravitational radiation from the coalescence of binary neutron stars: Effects due to the equation of state, spin, and mass ratio," *Physical Review D*, vol. 54, pp. 7261–7277, Dec. 1996.

[33] M. Shibata, "Constraining nuclear equations of state using gravitational waves from hypermassive neutron stars," *Phys. Rev. Lett.*, vol. 94, p. 201101, May 2005.

[34] M. Shibata, K. Taniguchi, and K. b. o. Uryū, "Merger of binary neutron stars with realistic equations of state in full general relativity," *Phys. Rev. D*, vol. 71, p. 084021, Apr 2005.

[35] R. Oechslin and H.-T. Janka, "Gravitational waves from relativistic neutron-star mergers with microphysical equations of state," *Phys. Rev. Lett.*, vol. 99, p. 121102, Sep 2007.

[36] A. Bauswein and H.-T. Janka, "Measuring neutron-star properties via gravitational waves from neutron-star mergers," *Phys. Rev. Lett.*, vol. 108, p. 011101, Jan 2012.

[37] A. Bauswein, H.-T. Janka, K. Hebeler, and A. Schwenk, "Equation-of-state dependence of the gravitational-wave signal from the ring-down phase of neutron-star mergers," *Phys. Rev. D*, vol. 86, p. 063001, Sep 2012.

[38] K. Hotokezaka, K. Kiuchi, K. Kyutoku, T. Muranushi, Y.-i. Sekiguchi, M. Shibata, and K. Taniguchi, "Remnant massive neutron stars of binary neutron star mergers: Evolution process and gravitational waveform," *Phys. Rev. D*, vol. 88, p. 044026, Aug 2013.

[39] K. Takami, L. Rezzolla, and L. Baiotti, "Spectral properties of the post-merger gravitational-wave signal from binary neutron stars," *Phys. Rev. D*, vol. 91, p. 064001, Mar 2015.

[40] S. Bernuzzi, T. Dietrich, and A. Nagar, "Modeling the complete gravitational wave spectrum of neutron star mergers," *Phys. Rev. Lett.*, vol. 115, p. 091101, Aug 2015.

[41] J. A. Clark, A. Bauswein, N. Stergioulas, and D. Shoemaker, "Observing gravitational waves from the post-merger phase of binary neutron star coalescence," *Classical and Quantum Gravity*, vol. 33, p. 085003, Apr. 2016.

[42] A. Bauswein, N. Stergioulas, and H.-T. Janka, "Exploring properties of high-density matter through remnants of neutron-star mergers," *European Physical Journal A*, vol. 52, p. 56, Mar. 2016.

[43] A. Bauswein and N. Stergioulas, "Spectral classification of gravitational-wave emission and equation of state constraints in binary neutron star mergers," *Journal of Physics G Nuclear Physics*, vol. 46, p. 113002, Nov. 2019.

[44] L. Baiotti, "Gravitational waves from neutron star mergers and their relation to the nuclear equation of state," *Progress in Particle and Nuclear Physics*, vol. 109, p. 103714, Nov. 2019.

[45] J. L. Friedman and N. Stergioulas, "Astrophysical implications of neutron star inspiral and coalescence," *International Journal of Modern Physics D*, vol. 29, no. 11, p. 2041015, 2020.

[46] T. Dietrich, T. Hinderer, and A. Samajdar, "Interpreting binary neutron star mergers: describing the binary neutron star dynamics, modelling gravitational waveforms, and analyzing detections," *General Relativity and Gravitation*, vol. 53, p. 27, Mar. 2021.

[47] N. Sarin and P. D. Lasky, "The evolution of binary neutron star post-merger remnants: a review," *General Relativity and Gravitation*, vol. 53, p. 59, June 2021.

[48] A. Bauswein, H.-T. Janka, K. Hebeler, and A. Schwenk, "Equation-of-state dependence of the gravitational-wave signal from the ring-down phase of neutron-star mergers," *Phys. Rev. D*, vol. 86, p. 063001, Sep 2012.

[49] S. Vretinaris, N. Stergioulas, and A. Bauswein, "Empirical relations for gravitational-wave asteroseismology of binary neutron star mergers," *Phys. Rev. D*, vol. 101, p. 084039, Apr 2020.

[50] S. Köppel, L. Bovard, and L. Rezzolla, "A general-relativistic determination of the threshold mass to prompt collapse in binary neutron star mergers," *The Astrophysical Journal*, vol. 872, p. L16, feb 2019.

[51] A. Bauswein, O. Just, H.-T. Janka, and N. Stergioulas, "Neutron-star Radius Constraints from GW170817 and Future Detections," *Astrophys. J. Lett.*, vol. 850, p. L34, Dec. 2017.

[52] A. Perego, D. Logoteta, D. Radice, S. Bernuzzi, R. Kashyap, A. Das, S. Padamata, and A. Prakash, "Probing the incompressibility of nuclear matter at ultrahigh density through the prompt collapse of asymmetric neutron star binaries," *Phys. Rev. Lett.*, vol. 129, p. 032701, Jul 2022.

[53] S. D. Tootle, L. J. Papenfort, E. R. Most, and L. Rezzolla, "Quasi-universal behavior of the threshold mass in unequal-mass, spinning binary neutron star mergers," *The Astrophysical Journal Letters*, vol. 922, p. L19, nov 2021.

[54] M. Kölsch, T. Dietrich, M. Ujevic, and B. Brügmann, "Investigating the mass-ratio dependence of the prompt-collapse threshold with numerical-relativity simulations," *Phys. Rev. D*, vol. 106, p. 044026, Aug 2022.

[55] B. P. Abbott *et al.*, "Prospects for observing and localizing gravitational-wave transients with Advanced LIGO, Advanced Virgo and KAGRA," *Living Rev. Rel.*, vol. 23, no. 1, p. 3, 2020.

[56] M. Punturo, M. Abernathy, F. Acernese, B. Allen, N. Andersson, K. Arun, F. Barone, B. Barr, M. Barsuglia, Beker, *et al.*, "The Einstein Telescope: a third-generation gravitational wave observatory," *Classical and Quantum Gravity*, vol. 27, p. 194002, Oct. 2010.

[57] B. P. Abbott *et al.*, "Exploring the Sensitivity of Next Generation Gravitational Wave Detectors," *Class. Quant. Grav.*, vol. 34, no. 4, p. 044001, 2017.

[58] D. Martynov, H. Miao, H. Yang, F. H. Vivanco, E. Thrane, R. Smith, P. Lasky, W. E. East, R. Adhikari, A. Bauswein, A. Brooks, Y. Chen, T. Corbitt, A. Freise, H. Grote, Y. Levin, C. Zhao, and A. Vecchio, "Exploring the sensitivity of gravitational wave detectors to neutron star physics," *Physical Review D*, vol. 99, p. 102004, May 2019.

[59] K. Ackley *et al.*, "Neutron Star Extreme Matter Observatory: A kilohertz-band gravitational-wave detector in the global network," *Publ. Astron. Soc. Austral.*, vol. 37, p. e047, 2020.

[60] D. Ganapathy, L. McCuller, J. G. Rollins, E. D. Hall, L. Barsotti, and M. Evans, "Tuning Advanced LIGO to kilohertz signals from neutron-star collisions," *Phys. Rev. D*, vol. 103, p. 022002, Jan. 2021.

[61] M. A. Page, M. Goryachev, H. Miao, Y. Chen, Y. Ma, D. Mason, M. Rossi, C. D. Blair, L. Ju, D. G. Blair, A. Schliesser, M. E. Tobar, and C. Zhao, "Gravitational wave detectors with broadband high frequency sensitivity," *Communications Physics*, vol. 4, p. 27, Dec. 2021.

[62] N. Sarin and P. D. Lasky, "Multimessenger astronomy with a kHz-band gravitational-wave observatory," *arXiv e-prints*, p. arXiv:2110.10892, Oct. 2021.

[63] C. Messenger, K. Takami, S. Gossan, L. Rezzolla, and B. S. Sathyaprakash, "Source redshifts from gravitational-wave observations of binary neutron star mergers," *Phys. Rev. X*, vol. 4, p. 041004, Oct 2014.

[64] P. J. Easter, P. D. Lasky, A. R. Casey, L. Rezzolla, and K. Takami, "Computing fast and reliable gravitational waveforms of binary neutron star merger remnants," *Phys. Rev. D*, vol. 100, p. 043005, Aug 2019.

[65] K. W. Tsang, T. Dietrich, and C. Van Den Broeck, "Modeling the post-merger gravitational wave signal and extracting binary properties from future binary neutron star detections," *Phys. Rev. D*, vol. 100, p. 044047, Aug 2019.

[66] S. Bose, K. Chakravarti, L. Rezzolla, B. S. Sathyaprakash, and K. Takami, "Neutron-star radius from a population of binary neutron star mergers," *Phys. Rev. Lett.*, vol. 120, p. 031102, Jan 2018.

[67] H. Yang, V. Paschalidis, K. Yagi, L. Lehner, F. Pretorius, and N. Yunes, "Gravitational wave spectroscopy of binary neutron star merger remnants with mode stacking," *Phys. Rev. D*, vol. 97, p. 024049, Jan 2018.

[68] P. J. Easter, S. Ghonge, P. D. Lasky, A. R. Casey, J. A. Clark, F. Hernandez Vivanco, and K. Chatziioannou, "Detection and parameter estimation of binary neutron star merger remnants," *Phys. Rev. D*, vol. 102, p. 043011, Aug 2020.

[69] T. Whittaker, W. E. East, S. R. Green, L. Lehner, and H. Yang, "Using machine learning to parametrize postmerger signals from binary neutron stars," *arXiv e-prints*, p. arXiv:2201.06461, Jan. 2022.

[70] M. Breschi, S. Bernuzzi, F. Zappa, M. Agathos, A. Perego, D. Radice, and A. Nagar, "Kilohertz gravitational waves from binary neutron star remnants: Time-domain model and constraints on extreme matter," *Phys. Rev. D*, vol. 100, p. 104029, Nov 2019.

[71] T. Whittaker, W. E. East, S. R. Green, L. Lehner, and H. Yang, "Using machine learning to parametrize postmerger signals from binary neutron stars," *Phys. Rev. D*, vol. 105, p. 124021, Jun 2022.

[72] M. Breschi, S. Bernuzzi, K. Chakravarti, A. Camilletti, A. Prakash, and A. Perego, "Kilohertz Gravitational Waves From Binary Neutron Star Mergers: Numerical-relativity Informed Postmerger Model," *arXiv e-prints*, p. arXiv:2205.09112, May 2022.

[73] H.-T. Janka, "Explosion mechanisms of core-collapse supernovae," *Annual Review of Nuclear and Particle Science*, vol. 62, no. 1, pp. 407–451, 2012.

[74] J. Lattimer, "Neutron stars and the nuclear matter equation of state," *Annual Review of Nuclear and Particle Science*, vol. 71, no. 1, pp. 433–464, 2021.

[75] M. Shibata, *100 Years of General Relativity: Volume 1, Numerical Relativity*. World Scientific, 2015.

[76] J. M. Lattimer and M. Prakash, "The physics of neutron stars," *Science*, vol. 304, no. 5670, pp. 536–542, 2004.

[77] Y. Suwa, T. Yoshida, M. Shibata, H. Umeda, and K. Takahashi, "On the minimum mass of neutron stars," *Monthly Notices of the Royal Astronomical Society*, vol. 481, pp. 3305–3312, 09 2018.

[78] J. Antoniadis *et al.*, "A Massive Pulsar in a Compact Relativistic Binary," *Science*, vol. 340, p. 6131, 2013.

[79] C. E. Rhoades and R. Ruffini, "Maximum mass of a neutron star," *Phys. Rev. Lett.*, vol. 32, pp. 324–327, Feb 1974.

[80] C. J. Pethick, D. G. Ravenhall, and C. P. Lorenz, "The inner boundary of a neutron-star crust," *Nuclear Physics A*, vol. 584, pp. 675–703, Feb. 1995.

[81] A. Kurkela, P. Romatschke, and A. Vuorinen, "Cold quark matter," *Phys. Rev. D*, vol. 81, p. 105021, May 2010.

[82] O. Komoltsev and A. Kurkela, "How perturbative qcd constrains the equation of state at neutron-star densities," *Phys. Rev. Lett.*, vol. 128, p. 202701, May 2022.

[83] M. Oertel, M. Hempel, T. Klähn, and S. Typel, "Equations of state for supernovae and compact stars," *Rev. Mod. Phys.*, vol. 89, p. 015007, Mar 2017.

[84] G. Burgio, H.-J. Schulze, I. Vidaña, and J.-B. Wei, "Neutron stars and the nuclear equation of state," *Progress in Particle and Nuclear Physics*, vol. 120, p. 103879, 2021.

[85] K. Chatziioannou, J. A. Clark, A. Bauswein, M. Millhouse, T. B. Littenberg, and N. Cornish, "Inferring the post-merger gravitational wave emission from binary neutron star coalescences," *Phys. Rev. D*, vol. 96, p. 124035, Dec 2017.

[86] A. Torres-Rivas, K. Chatziioannou, A. Bauswein, and J. A. Clark, "Observing the post-merger signal of gw170817-like events with improved gravitational-wave detectors," *Phys. Rev. D*, vol. 99, p. 044014, Feb 2019.

[87] Kokkotas, K. D. and Ruoff, J., "Radial oscillations of relativistic stars*," *A&A*, vol. 366, no. 2, pp. 565–572, 2001.

[88] "LORENE: Langage Objet pour la RElativité NumériquE." webpage: http://www.lorene.obspm.fr/.

[89] E. Gourgoulhon, P. Grandclément, K. Taniguchi, J.-A. Marck, and S. Bonazzola, "Quasiequilibrium sequences of synchronized and irrotational binary neutron stars in general relativity: Method and tests," *Phys. Rev. D*, vol. 63, p. 064029, Feb 2001.

[90] Z. Etienne, S. R. Brandt, P. Diener, W. E. Gabella, M. Gracia-Linares, R. Haas, A. Kedia, M. Alcubierre, D. Alic, G. Allen, *et al.*, "The einstein toolkit," May 2021. To find out more, visit http://einsteintoolkit.org.

[91] R. Oechslin, S. Rosswog, and F.-K. Thielemann, "Conformally flat smoothed particle hydrodynamics application to neutron star mergers," *Phys. Rev. D*, vol. 65, p. 103005, May 2002.

[92] Oechslin, R., Janka, H.-T., and Marek, A., "Relativistic neutron star merger simulations with non-zero temperature equations of state* - i. variation of binary parameters and equation of state," *A&A*, vol. 467, no. 2, pp. 395–409, 2007.

[93] J. Isenberg and J. Nester, "Canonical Gravity," in *General Relativity and Gravitation. Vol. 1. One hundred years after the birth of Albert Einstein. Edited by A. Held. New York*, vol. 1, p. 23, Jan. 1980.

[94] J. R. Wilson, G. J. Mathews, and P. Marronetti, "Relativistic numerical model for close neutron-star binaries," *Phys. Rev. D*, vol. 54, pp. 1317–1331, Jul 1996.

[95] R. Arnowitt, S. Deser, and C. W. Misner, "Republication of: The dynamics of general relativity," *General Relativity and Gravitation*, vol. 40, pp. 1997–2027, Sept. 2008.

[96] F. Banyuls, J. A. Font, J. M. Ibanez, J. M. Marti, and J. A. Miralles, "Numerical {3 + 1} general relativistic hydrodynamics: A local characteristic approach," *The Astrophysical Journal*, vol. 476, pp. 221–231, feb 1997.

[97] J. A. Font, "Numerical Hydrodynamics and Magnetohydrodynamics in General Relativity," *Living Rev. Relativity*, vol. 11, no. 7, 2008.

[98] L. Baiotti, I. Hawke, P. J. Montero, F. Löffler, L. Rezzolla, N. Stergioulas, J. A. Font, and E. Seidel, "Three-dimensional relativistic simulations of rotating neutron star collapse to a Kerr black hole," *Phys. Rev. D*, vol. 71, p. 024035, 2005.

[99] P. Mösta, B. C. Mundim, J. A. Faber, R. Haas, S. C. Noble, T. Bode, F. Löffler, C. D. Ott, C. Reisswig, and E. Schnetter, "GRHydro: A new open source general-relativistic magnetohydrodynamics code for the Einstein Toolkit," *Classical and Quantum Gravity*, vol. 31, no. 1, p. 015005, 2014.

[100] T. W. Baumgarte and S. L. Shapiro, "Numerical integration of einstein's field equations," *Phys. Rev. D*, vol. 59, p. 024007, Dec 1998.

[101] M. Shibata and T. Nakamura, "Evolution of three-dimensional gravitational waves: Harmonic slicing case," *Phys. Rev. D*, vol. 52, pp. 5428–5444, Nov 1995.

[102] T. Nakamura, K. Oohara, and Y. Kojima, "General Relativistic Collapse to Black Holes and Gravitational Waves from Black Holes," *Progress of Theoretical Physics Supplement*, vol. 90, pp. 1–218, 01 1987.

[103] S. Bernuzzi and D. Hilditch, "Constraint violation in free evolution schemes: Comparing the bssnok formulation with a conformal decomposition of the z4 formulation," *Phys. Rev. D*, vol. 81, p. 084003, Apr 2010.

[104] D. Hilditch, S. Bernuzzi, M. Thierfelder, Z. Cao, W. Tichy, and B. Brügmann, "Compact binary evolutions with the z4c formulation," *Phys. Rev. D*, vol. 88, p. 084057, Oct 2013.

[105] T. Dietrich, T. Hinderer, and A. Samajdar, "Interpreting binary neutron star mergers: describing the binary neutron star dynamics, modelling gravitational waveforms, and analyzing detections," *General Relativity and Gravitation*, vol. 53, p. 27, Mar. 2021.

[106] D. Pollney, C. Reisswig, E. Schnetter, N. Dorband, and P. Diener, "High accuracy binary black hole simulations with an extended wave zone," *Phys. Rev. D*, vol. 83, p. 044045, Feb 2011.

[107] C. Reisswig, C. D. Ott, E. Abdikamalov, R. Haas, P. Mösta, and E. Schnetter, "Formation and coalescence of cosmological supermassive-black-hole binaries in supermassive-star collapse," *Phys. Rev. Lett.*, vol. 111, p. 151101, Oct 2013.

[108] X.-D. Liu, S. Osher, and T. Chan, "Weighted essentially non-oscillatory schemes," *Journal of Computational Physics*, vol. 115, no. 1, pp. 200 – 212, 1994.

[109] G.-S. Jiang and C.-W. Shu, "Efficient implementation of weighted eno schemes," *Journal of Computational Physics*, vol. 126, no. 1, pp. 202 – 228, 1996.

[110] A. Harten, P. D. Lax, and B. van Leer, "On upstream differencing and Godunov-type schemes for hyperbolic conservation laws," *SIAM review*, vol. 25, no. 1, p. 35, 1983.

[111] S. C. Noble, C. F. Gammie, J. C. McKinney, and L. D. Zanna, "Primitive variable solvers for conservative general relativistic magnetohydrodynamics," *The Astrophysical Journal*, vol. 641, pp. 626–637, apr 2006.

[112] "McLachlan, a public BSSN code."

[113] "Kranc: Kranc assembles numerical code."

[114] C. Reisswig, C. D. Ott, U. Sperhake, and E. Schnetter, "Gravitational wave extraction in simulations of rotating stellar core collapse," *Phys. Rev. D*, vol. 83, p. 064008, Mar 2011.

[115] J. D. Brown, P. Diener, O. Sarbach, E. Schnetter, and M. Tiglio, "Turducken-ing black holes: an analytical and computational study," *Phys. Rev. D*, vol. 79, p. 044023, 2009.

[116] T. W. Baumgarte and S. L. Shapiro, *Numerical Relativity: Solving Einstein's Equations on the Computer*. Cambridge University Press, 2010.

[117] J. M. Hyman, "The method of lines solution of partial differential equations," Tech. Rep. COO-3077-139, ERDA Mathematics and Computing Laboratory, Courant Institute of Mathematical Sciences, New York University, October 1976.

[118] K. Kyutoku, M. Shibata, and K. Taniguchi, "Reducing orbital eccentricity in initial data of binary neutron stars," *Phys. Rev. D*, vol. 90, p. 064006, Sep 2014.

[119] P. C. Peters, "Gravitational radiation and the motion of two point masses," *Phys. Rev.*, vol. 136, pp. B1224–B1232, Nov 1964.

[120] M. Shibata, T. W. Baumgarte, and S. L. Shapiro, "Stability of coalescing binary stars against gravitational collapse: Hydrodynamical simulations," *Phys. Rev. D*, vol. 58, p. 023002, Jun 1998.

[121] W. L. Briggs, V. E. Henson, and S. F. McCormick, *A Multigrid Tutorial (2nd Ed.)*. USA: Society for Industrial and Applied Mathematics, 2000.

[122] R. Schaback and H. Wendland, "Kernel techniques: From machine learning to meshless methods," *Acta Numerica*, vol. 15, p. 543–639, 2006.

[123] S. Rosswog, "SPH Methods in the Modelling of Compact Objects," *Living Reviews in Computational Astrophysics*, vol. 1, p. 1, Oct. 2015.

[124] A. Bauswein, H.-T. Janka, and R. Oechslin, "Testing approximations of thermal effects in neutron star merger simulations," *Phys. Rev. D*, vol. 82, p. 084043, Oct 2010.

[125] A. Bauswein, S. Blacker, V. Vijayan, N. Stergioulas, K. Chatziioannou, J. A. Clark, N.-U. F. Bastian, D. B. Blaschke, M. Cierniak, and T. Fischer, "Equation of state constraints from the threshold binary mass for prompt collapse of neutron star mergers," *Phys. Rev. Lett.*, vol. 125, p. 141103, Sep 2020.

[126] J. J. Monaghan and R. A. Gingold, "Shock Simulation by the Particle Method SPH," *Journal of Computational Physics*, vol. 52, pp. 374–389, Nov. 1983.

[127] H. Müther, M. Prakash, and T. Ainsworth, "The nuclear symmetry energy in relativistic brueckner-hartree-fock calculations," *Physics Letters B*, vol. 199, no. 4, pp. 469 – 474, 1987.

[128] B. P. Abbott, R. Abbott, T. D. Abbott, F. Acernese, K. Ackley, C. Adams, T. Adams, P. Addesso, R. X. Adhikari, V. B. Adya, *et al.*, "Gw170817: Observation of gravitational waves from a binary neutron star inspiral," *Phys. Rev. Lett.*, vol. 119, p. 161101, Oct 2017.

[129] J. S. Read, B. D. Lackey, B. J. Owen, and J. L. Friedman, "Constraints on a phenomenologically parametrized neutron-star equation of state," *Phys. Rev. D*, vol. 79, p. 124032, Jun 2009.

[130] C. Reisswig and D. Pollney, "Notes on the integration of numerical relativity waveforms," *Classical and Quantum Gravity*, vol. 28, p. 195015, sep 2011.

[131] A. Bauswein, R. A. Pulpillo, H.-T. Janka, and S. Goriely, "NUCLEOSYNTHESIS CONSTRAINTS ON THE NEUTRON STAR-BLACK HOLE MERGER RATE," *The Astrophysical Journal*, vol. 795, p. L9, oct 2014.

[132] M. Hempel and J. Schaffner-Bielich, "A statistical model for a complete supernova equation of state," *Nuclear Physics A*, vol. 837, no. 3, pp. 210–254, 2010.

[133] A. W. Steiner, M. Hempel, and T. Fischer, "Core-collapse Supernova Equations of State Based on Neutron Star Observations," *Astrophysical Journal*, vol. 774, p. 17, Sept. 2013.

[134] M. Hempel, T. Fischer, J. Schaffner-Bielich, and M. Liebendörfer, "NEW EQUATIONS OF STATE IN SIMULATIONS OF CORE-COLLAPSE SUPERNOVAE," *The Astrophysical Journal*, vol. 748, p. 70, mar 2012.

[135] H. Toki, D. Hirata, Y. Sugahara, K. Sumiyoshi, and I. Tanihata, "Relativistic many body approach for unstable nuclei and supernova," *Nuclear Physics A*, vol. 588, no. 1, pp. c357–c363, 1995. Proceedings of the Fifth International Symposium on Physics of Unstable Nuclei.

[136] Y. Sugahara and H. Toki, "Relativistic mean-field theory for unstable nuclei with non-linear σ and ω terms," *Nuclear Physics A*, vol. 579, no. 3, pp. 557–572, 1994.

[137] J. M. Lattimer and F. Douglas Swesty, "A generalized equation of state for hot, dense matter," *Nuclear Physics A*, vol. 535, no. 2, pp. 331–376, 1991.

[138] G. A. Lalazissis, J. König, and P. Ring, "New parametrization for the lagrangian density of relativistic mean field theory," *Phys. Rev. C*, vol. 55, pp. 540–543, Jan 1997.

[139] G. Shen, C. J. Horowitz, and S. Teige, "New equation of state for astrophysical simulations," *Phys. Rev. C*, vol. 83, p. 035802, Mar 2011.

[140] S. Banik, M. Hempel, and D. Bandyopadhyay, "NEW HYPERON EQUATIONS OF STATE FOR SUPERNOVAE AND NEUTRON STARS IN DENSITY-DEPENDENT HADRON FIELD THEORY," *The Astrophysical Journal Supplement Series*, vol. 214, p. 22, sep 2014.

[141] B. D. Lackey, M. Nayyar, and B. J. Owen, "Observational constraints on hyperons in neutron stars," *Phys. Rev. D*, vol. 73, p. 024021, Jan 2006.

[142] M. Alford, M. Braby, M. Paris, and S. Reddy, "Hybrid stars that masquerade as neutron stars," *The Astrophysical Journal*, vol. 629, pp. 969–978, aug 2005.

[143] F. Douchin and P. Haensel, "A unified equation of state of dense matter and neutron star structure," *Astron. Astrophys.*, vol. 380, pp. 151–167, Dec. 2001.

[144] A. Akmal, V. Pandharipande, and D. Ravenhall, "The Equation of state of nucleon matter and neutron star structure," *Phys. Rev. C*, vol. 58, pp. 1804–1828, 1998.

[145] R. B. Wiringa, V. Fiks, and A. Fabrocini, "Equation of state for dense nucleon matter," *Phys. Rev. C*, vol. 38, pp. 1010–1037, Aug 1988.

[146] S. Goriely, N. Chamel, and J. M. Pearson, "Further explorations of skyrme-hartree-fock-bogoliubov mass formulas. xii. stiffness and stability of neutron-star matter," *Phys. Rev. C*, vol. 82, p. 035804, Sep 2010.

[147] G. R. Lee, R. Gommers, F. Waselewski, K. Wohlfahrt, and A. O'Leary, "Pywavelets: A python package for wavelet analysis," *Journal of Open Source Software*, vol. 4, no. 36, p. 1237, 2019.

[148] F. Maione, R. De Pietri, A. Feo, and F. Löffler, "Spectral analysis of gravitational waves from binary neutron star merger remnants," *Phys. Rev. D*, vol. 96, p. 063011, Sep 2017.

[149] M. A. Branch, T. F. Coleman, and Y. Li, "A subspace, interior, and conjugate gradient method for large-scale bound-constrained minimization problems," *SIAM Journal on Scientific Computing*, vol. 21, no. 1, pp. 1–23, 1999.

[150] R. H. Byrd, R. B. Schnabel, and G. A. Shultz, "Approximate solution of the trust region problem by minimization over two-dimensional subspaces," *Mathematical Programming*, vol. 40, pp. 247–263, Jan 1988.

[151] P. Virtanen, R. Gommers, T. E. Oliphant, M. Haberland, T. Reddy, D. Cournapeau, E. Burovski, P. Peterson, W. Weckesser, J. Bright, *et al.*, "SciPy 1.0: Fundamental Algorithms for Scientific Computing in Python," *Nature Methods*, vol. 17, pp. 261–272, 2020.

[152] T. A. Apostolatos, "Search templates for gravitational waves from precessing, inspiraling binaries," *Phys. Rev. D*, vol. 52, pp. 605–620, Jul 1995.

[153] A. Passamonti and N. Andersson, "Merger-inspired rotation laws and the low-T/W instability in neutron stars," *Mon. Not. Roy. Astron. Soc.*, vol. 498, pp. 5904–5915, 09 2020.

[154] X. Xie, I. Hawke, A. Passamonti, and N. Andersson, "Instabilities in neutron-star postmerger remnants," *Physical Review D*, vol. 102, p. 044040, Aug. 2020.

[155] R. De Pietri, A. Feo, J. A. Font, F. Löffler, M. Pasquali, and N. Stergioulas, "Numerical-relativity simulations of long-lived remnants of binary neutron star mergers," *Phys. Rev. D*, vol. 101, p. 064052, Mar 2020.

[156] A. Bauswein, N. Stergioulas, and H.-T. Janka, "Revealing the high-density equation of state through binary neutron star mergers," *Phys. Rev. D*, vol. 90, p. 023002, Jul 2014.

[157] G. Ashton, M. Hübner, P. D. Lasky, C. Talbot, K. Ackley, S. Biscoveanu, Q. Chu, A. Divakarla, P. J. Easter, B. Goncharov, F. H. Vivanco, J. Harms, M. E. Lower, G. D. Meadors, D. Melchor, E. Payne, M. D. Pitkin, J. Powell, N. Sarin, R. J. E. Smith, and E. Thrane, "Bilby: A user-friendly bayesian inference library for gravitational-wave astronomy," *The Astrophysical Journal Supplement Series*, vol. 241, p. 27, apr 2019.